Summer 1995

Studies of Mixing Processes in Gases and Effects on Combustion and Stability

Frank Paul Kozusko Jr.
Old Dominion University

STUDIES OF MIXING PROCESSES IN GASES AND EFFECTS ON COMBUSTION AND STABILITY

by

Frank Paul Kozusko, Jr.

B.S.(Physics) 1969, Utica College of Syracuse University
M.A.(Physics) 1971, University of California at Davis
M.S.(Computational and Applied Mathematics) 1991, Old Dominion University

A Dissertation Submitted to the Faculty of
Old Dominion University in Partial Fulfillment of the
Requirements for the Degree of

DOCTOR OF PHILOSOPHY
Computational and Applied Mathematics

OLD DOMINION UNIVERSITY
July, 1995

Approved by:

D.Glenn Lasseigne, (Director)

ABSTRACT

STUDIES OF MIXING PROCESSES IN GASES AND EFFECTS ON COMBUSTION AND STABILITY

Frank P. Kozusko, Jr.

Old Dominion University, 1995

Director: Dr. D. Glenn Lasseigne

Three physical models of laminar mixing of initially separated gases are studied. Two models study the effects of the mixing dynamics on the chemical reactions between the gases. The third model studies the structure and stability of a laminar mixing layer in a binary gas. The three models are:

1. Two ideal and incompressible gases representing fuel and oxidizer are initially at rest and separated across an infinite linear interface in a two dimensional system. Combustion, expected as the gases mix, will lead to a rapid rise in temperature in a localized area, i.e. ignition. The mixing of the gases is enhanced by two counter-rotating vortices with centers located on the initial interface. The ignition process is studied by an asymptotic analysis.

Ignition times for the double vortex lay between the no vortex and the single vortex times. As the distance between the two counter-rotating vortices gets smaller, ignition times approach the no vortex case, for increasing distance the ignition times approach the single vortex case.

2. Laminar mixing of compressible gases representing two reduced chemical systems is studied. The gases are initially separated into two semi-infinite planes and have different freestream flow velocities. Combustion is followed through ignition to the post-ignition steady flame.

   The ignition distance is an inverse logarithmic function of the initially required loading of a non-fuel, non-oxidizer radical. The post-ignition flame temperature is not effected by the initial radical concentration.

3. Laminar compressible non-reacting mixing of two real gases of different freestream temperatures and flow velocities is studied. Realistic values of transport properties are obtained from various tables or calculated from theory. The transport properties are dynamically calculated as functions of the changing temperature and gas concentrations across the mixing layer. A steady state mixed solution is found. Items of interest are the stability characteristics, the profiles of temperature and gas concentrations and the variations of the Prandtl and Lewis numbers.

   The Lewis number and Prandtl numbers may vary significantly through the mixing layer. Neutral phase speeds and growth rates for spatial stability are also shown to be effected by the molecular weights and physical properties.

Acknowledgment

I wish to acknowledge all those who have encouraged and assisted me in this eight year quest.

My thanks to the chairman, Dr. Tweed, and my three graduate advisors: Dr. Wohl, Dr. Dorrepaal and Dr. Swetits. Dr. Wohl first encouraged me to go forward with my dream during my initial inquiries into the possibility of graduate study. Dr. Dorrepaal scheduled courses that could fit into my work schedule during my part-time studies. Dr. Swetits helped me transition from a part-time to full-time student. Dr. Tweed always scheduled my teaching assignments to best fit my course work and research schedule. All my professors at ODU were helpful in working around my Naval duty schedule and helping me relearn some of the fundamentals buried by a long academic hiatus. I wish to thank Drs. Hu, Grosch and Lasseigne for mentoring me in computer system techniques and fluid dynamics.

My three years of research have been conducted at the Institute for Computer Applications in Science and Engineering (ICASE). The staff and scientists were always helpful and I learned much from them. The superior computing facilities and the proximity to my house, more than doubled my output. I am thankful to Dr Hussaini, Director of ICASE, for his faith in me and for my appointed as an ICASE graduate fellow.

A special acknowledgment goes to Dr. Tom Jackson. He taught the very first course in my recommenced graduate career in Fall, 1987. He later agreed to be my thesis advisor and continued to provide me constant mentorship these last three years,

even when he was no longer on the Faculty at ODU. Thanks, Tom, for teaching this old (sea) dog new tricks.

Finally, a very special acknowledgment and thanks to my understanding wife, Christine, who has tolerated eight years of my working days and studying nights (or sometimes studying days and working nights). I promise I'll fix all the leaking faucets in the house, . . . soon.

Contents

APPENDICES

List of Tables

List of Figures

Chapter 1

INTRODUCTION

In this thesis, three different physical models of laminar mixing of initially separated gases are studied. The first two models study the effects of the mixing dynamics on the chemical reactions between the gases. Reduced kinetics is used, where a reduced number of chemical reactions, reactants and products are used to model a more complex system. The third model studies the structure and stability of a laminar mixing layer in a binary gas. Presented below is a more detailed overview of the three models. Also presented is a brief introduction of the governing equations used in laminar mixing layers, which will be further developed as applicable in the subsequent chapters. All of the systems studied here are assumed to depend on two spatial variables, and are either steady or unsteady according to the appropriate physical model. The three models are:

1. Two ideal and incompressible gases representing fuel and oxidizer are initially separated across an infinite linear interface in a two dimensional system. The gases are initially at rest with respect to each other. The system temperature

is near that where combustion, expected as the gases mix, will lead to a rapid rise in temperature in a localized area, an ignition point. The mixing of the gases, which would normally proceed by diffusion, is enhanced by two counter-rotating vortices whose centers are located on the initial interface. The ignition process is studied by asymptotic analysis and compared to previous work of similiar systems without vortex mixing and one with mixing provided by a single vortex.

2. Laminar mixing, ignition and stability of compressible gases representing a reduced chemical system is studied. Gases initially separated into two semi-infinite plans are mixed by diffusion and differing freestream flow velocities. Combustion is followed through and post ignition. Parameters of interest are the ignition distance from the initial stream mixing point, the post ignition temperature and stability as determined by the Lees/ Lin condition. Two different reduced chemical systems are analyzed.

3. Laminar compressible non-reacting mixing of two real gases of different freestream temperatures and flow velocities is studied. Realistic values of transport properties are obtained from various tables or calculated from theory. The transport properties are dynamically calculated as functions of the changing temperature and gas concentrations across the mixing layer. A steady state mixed solution is found. Items of interest are the stability characteristics and the profiles of temperature and gas concentrations as well as the Prandtl and Lewis numbers.

1.1 Chemical Reduction Systems

The simplest combustion process might look like

$$FUEL + OXYGEN \rightarrow PRODUCT + HEAT \tag{1.1.1}$$

and involves only two reactants and produces one product and thermal energy as indicated. Combustion processes are, of course, more complicated and involve many reactions, reactants and products. To make the combustion models more manageable, reduced numbers of component gases are used. This is accomplished by fiat (Birkan and Law [1]) or a reduction theory. Some reduction theories indeed produce the simple model above while others limit the number of components to only a few (Peters [2]).

1.2 Physical and Transport Properties

The physical properties of the gases affecting the mixing include molecular weight, specific heat and heat release of the reaction. Thermodynamic properties which must be considered in the mixing are the coefficients of thermal conductivity (λ), viscosity (μ) and species diffusion (D). Models are simplified by assuming equal weights, as in Chapters Two and Three. Other simplifications are the assumptions of constant and nominal values for the above properties. In Chapter Two the most simplifying assumptions are used while the investigation of Chapter Four attempts to calculate the most realistic values possible.

1.3 Ignition Dynamics in the Field of a Vortex Pair

In Chapter Two, the ignition dynamics of the initially separated fuel and oxidant are investigated using a simple model. In this model, fuel and oxidizer in an infinite plane are initially separated by the x-axis and are at rest. At time $t = 0$, two counter-rotating vortices with centers at $(-d, 0)$ (clockwise rotating) and $(d, 0)$ (counter-clockwise rotating) are initiated. The individual vortices are equally described, except for the rotation direction, by a radial velocity of zero and angular velocity of

$$V_{\pm d} = \frac{\pm R}{r_{\pm}}.$$

R is the vortex Reynolds number and r is the distance to the applicable vortex center. The system is simplified by assuming constant density, equal molecular weights and constant transport properties. At time $t > 0$, the fuel and the oxidizer mix by diffusion and the convective force of the combined vortices. Combustion is modeled as a one-step irreversible Arrhenius reaction. Rapid ignition is expected, so the system is studied on an asymptotic time scale. The ignition time and the ignition location are determined for various sets of initial parameters. Results are compared to previous work of Marble [3] who studied a similar system where mixing was by diffusion only and that conducted by Macaraeg, Jackson, and Hussaini [4] where mixing was by diffusion and a single vortex.

1.4 Reduced Mechanism Combustion

In Chapter Three, two reduced kinetic models are studied in a steady state, spatially varying laminar mixing layer. The first kinetic model was proposed by Birkan and Law [1]. In this system, equal molecular weights and constant transport properties were assumed. The second kinetic model was proposed by Peters [2], which models methane-air combustion. In this system equal molecular weights and constant transport properties were also used. However, the reaction rates and the heat release values were realistically calculated from available data tables. The physical system is that of two gases initially separated by a splitter. Each gas has a flow velocity parallel to the plate. At $x = 0$, the plate ends and the gases begin to mix by convection and diffusion. The combustion process is tracked in the x-direction through ignition to post-ignition steady flame structure. Of interest is the comparison of the ignition and post-ignition characteristics of the two reduction systems and the effect on the post-ignition structure of the initial conditions. As will be discussed further, Birkan and Law studied only the post-ignition flame structure and not the approach to ignition.

1.5 Structure and Stability of a Compressible Mixing Layer in a Binary Gas

In Chapters Four and Five, the physical system is the same as the previous one. However, only mixing and not combustion is assumed, and actual gas combinations

are used. The gases included in this study are hydrogen (H_2), helium (He), neon (Ne), nitrogen (N_2), oxygen (O_2) and argon (Ar). The true molecular weights are used and the transport properties are calculated using the best data available. Calculations and results are compared to previous work by Jackson and Grosch [5] [7] and Grosch [6].

1.6 Governing Equations

In this and subsequent sections, the governing equations for the three models of mixing described above are presented. The two-dimensional boundary layer equations for a reacting compressible flow mixture are given by Anderson [8]:

continuity,

$$\frac{\partial \rho^*}{\partial t^*} + \frac{\partial(\rho^* u^*)}{\partial x^*} + \frac{\partial(\rho^* v^*)}{\partial y^*} = 0; \tag{1.6.2}$$

conservation of momentum in the x-direction,

$$\rho^* \frac{\partial u^*}{\partial t^*} + \rho^* u^* \frac{\partial u^*}{\partial x^*} + \rho^* v^* \frac{\partial u^*}{\partial y^*} - \frac{\partial}{\partial y^*}\left(\mu^* \frac{\partial u^*}{\partial y^*}\right) = -\frac{\partial P^*}{\partial x^*}; \tag{1.6.3}$$

conservation of momentum in the y-direction,

$$\frac{\partial P^*}{\partial y^*} = 0; \tag{1.6.4}$$

energy,

$$\rho^* C_p^* \frac{\partial T^*}{\partial t^*} + \rho^* u^* C_p^* \frac{\partial T^*}{\partial x^*} + \rho^* v^* C_p^* \frac{\partial T^*}{\partial y^*} =$$
$$\frac{\partial}{\partial y^*}\left(\lambda^* \frac{\partial T^*}{\partial y^*}\right) + \mu^* \left(\frac{\partial u^*}{\partial y^*}\right)^2 + u^* \frac{\partial P^*}{\partial x^*} + \sum_{i=1}^{n} C_{p_i}^* \rho^* D_i^* \frac{\partial F_i}{\partial y^*} \frac{\partial T^*}{\partial y^*} - \sum_{i=1}^{n} h_i^* \Omega_i^*; \tag{1.6.5}$$

and conservation of species,

$$\rho^* \frac{\partial F_i^*}{\partial t^*} + \rho^* u^* \frac{\partial F_i^*}{\partial x^*} + \rho^* v^* \frac{\partial F_i^*}{\partial y^*} = \frac{\partial}{\partial y^*} \left(\rho^* D_i^* \frac{\partial F_i^*}{\partial y^*} \right) + \sum_{j=1}^{n} \nu^{ij} \Omega_j^*. \tag{1.6.6}$$

The asterisk indicates the dimensional form of the quantities: ρ^* the system mass density, C_p^* the specific heat capacity of the system, T^* the temperature, t^* the time, u^* the velocity in the x^* direction (parallel to the boundary), v^* the velocity in the y^* direction (normal to the boundary), μ^* the coefficient of viscosity of the system, P^* the pressure, $C_{p_i}^*$ the heat capacity of the i^{th} gas, D_i^* the diffusion coefficient of the i^{th} gas with respect to the total system, λ^* the thermal diffusion coefficient of the system, F_i^* the mass density of the i^{th} gas, Ω_j^* the rate of the j^{th} reaction (if any), ν^{ij} the stoichiometric number representing the production or absorption of the i^{th} gas in the j^{th} reaction, and h_i^* is the enthalpy change of the i^{th} reaction.

1.6.1 Non-dimensional Equations

The standard method used to provide universal reference for differing system values is to non-dimensionalize all values. The choices of the study are

$$u^* = u u_\infty^*, \qquad \lambda^* = \lambda \lambda_\infty^*, \qquad C_p^* = C_{p\infty}^* C_p$$

$$x^* = x L^*, \qquad y^* = \frac{y L^*}{\sqrt{Re}}, \qquad \text{and} \qquad t^* = \frac{t L^*}{u_\infty^*}.$$

All other values are non-dimensionalized similarly by their respective dimensional value at infinity. The non-dimensional equations are then

continuity,

$$\frac{\partial \rho}{\partial t} + \frac{\partial (\rho u)}{\partial x} + \frac{\partial (\rho v)}{\partial y} = 0; \tag{1.6.7}$$

conservation of momentum in the x-direction,

$$\rho\frac{\partial u}{\partial t}+\rho u\frac{\partial u}{\partial x}+\rho v\frac{\partial u}{\partial y}-\frac{\partial}{\partial y}\left(\mu\frac{\partial u}{\partial y}\right)=-\frac{\partial P}{\partial x}; \tag{1.6.8}$$

conservation of momentum in the y-direction,

$$\frac{\partial P}{\partial y}=0; \tag{1.6.9}$$

conservation of energy,

$$\begin{aligned}\rho C_p\frac{\partial T}{\partial t}+\rho u C_p\frac{\partial T}{\partial x}+\rho v C_p\frac{\partial T}{\partial y}=&\\ \frac{1}{Pr_\infty}\frac{\partial}{\partial y}\left(\lambda\frac{\partial T}{\partial y}\right)+M_\infty^2(\gamma_\infty-1)\mu\left(\frac{\partial u}{\partial y}\right)^2+u\left(\frac{\partial P}{\partial x}\right)+&\\ \frac{1}{Sc_\infty}\sum_{i=1}^{n}C_{p_i}\rho D_i\left(\frac{\partial F_i}{\partial y}\right)\left(\frac{\partial T}{\partial y}\right)-\sum_{i=1}^{n}h_i\Omega_i;&\end{aligned} \tag{1.6.10}$$

and

conservation of species,

$$\rho\frac{\partial F_i}{\partial t}+\rho u\frac{\partial F_i}{\partial x}+\rho v\frac{\partial F_i}{\partial y}=\frac{\partial}{\partial y}\left(\rho D_i\frac{\partial F_i}{\partial y}\right)+\sum_{j=1}^{n}\nu^{ij}\Omega_j. \tag{1.6.11}$$

The following non-dimensional quantities are defined:

$$Re=\frac{L^*\rho_\infty^* u_\infty^*}{\mu_\infty^*},\qquad Pr_\infty=\frac{\mu_\infty^* C_{p\infty}^*}{\lambda_\infty^*},\qquad Le_\infty=\frac{\lambda_\infty^*}{\rho_\infty^* D_\infty^* C_{p\infty}^*},$$

$$Sc_\infty=\frac{\mu_\infty^*}{\rho_\infty^* D_\infty^*},\qquad \gamma_\infty=\frac{C_{p_\infty}}{C_{v_\infty}},\qquad \text{and}\qquad \mathrm{M}_\infty=\frac{\mathrm{u}_\infty^*}{\mathrm{a}_\infty^*}.$$

Here M_∞ is the Mach number at infinity and C_v is the specific heat at constant volume.

1.6.2 Equation of State: Ideal Gas Law

The ideal gas law for a gas mixture in its non-dimensional form is

$$P=\rho T\frac{\sum_{i=1}^{n}(\frac{F_i}{W_i})}{\sum_{i=1}^{n}(\frac{F_{i,\infty}}{W_i})}, \tag{1.6.12}$$

where W_i is the molecular weight of the i^{th} gas.

1.6.3 Reaction Rates

The reaction rates used in this study are of the Arrhenius form. If two species with densities F_1 and F_2 are expected to react on contact, the model rate used is:

$$\Omega = F_1 F_2 Da \exp(\frac{-Ze}{T}). \tag{1.6.13}$$

Here, Da is the Damkohler number for the reaction, Ze is the Zeldovich number which is the nondimensional activation energy

$$Ze = \frac{E^*}{R^o T_\infty^*}, \tag{1.6.14}$$

where E^* is the dimensional activation energy for the particular reaction and R^o is the gas constant.

1.7 Coordinate Transformations

A standard technique in steady boundary layer theory is to perform two coordinate-system transformations to simplify the governing equations for the case of a spatially dependent density. The first transformation eliminates the density ρ from the continuity equation. The second reduces the dependence of the flow variables on the x-coordinate and replaces the continuity equation with a stream function. When the assumption of constant density is used, the first transformation is not needed.

1.7.1 Howarth-Dorodnitsyn Transformation

As mentioned above, the Howarth-Dorodnitsyn transformation [8] is used to eliminate the density from the continuity equation and is given by

$$(x,y) \rightarrow (X,Y),$$

$$Y = \int_0^y \rho d\bar{y}, \qquad X = x,$$

$$\text{and} \qquad V = \rho v + u \int_0^y \rho_x d\bar{y}. \tag{1.7.15}$$

where the notation $(\ )_x = \frac{\partial(\ )}{\partial x}$ has been adopted. The governing equations become

$$P_x = 0,$$

$$u_X + V_Y = 0,$$

$$\rho(uu_X + Vu_Y) = (\mu\rho u_Y)_Y,$$

$$\rho C_p(uT_X + VT_Y) =$$

$$(\frac{1}{Pr_\infty})(\lambda\rho T_Y)_Y + M_\infty^2(\gamma_\infty - 1)\mu(u_Y)^2 + (\frac{1}{Sc_\infty})\rho\sum_{i=1}^{n} C_{p_i} D_i T_Y F_{i,Y} - \sum_{i=1}^{n} h_i\Omega_i \tag{1.7.16}$$

and

$$\rho(uF_{i,Y} + VF_{i,Y}) = \frac{1}{Sc_\infty}(\rho D_i F_{i,Y})_Y + \sum_{j=1}^{n} \nu^{ij}\Omega_j. \tag{1.7.17}$$

1.7.2 Similiarity Transformation

For certain boundary conditions and using certain similarity transformations, the flow is found to be independent of one of the new independent variables. A standard

transformation is (Jackson and Grosch [7]):

$$(X, Y) \rightarrow (x, \eta),$$

$$\eta = \frac{Y}{2\sqrt{x}}, \qquad x = X$$

and

$$u = f'(\eta), \tag{1.7.18}$$

where primes denote differentiation with respect to the similarity variable η. The above transformation yields $V = (\eta f' - f)/\sqrt{x}$ which satisfies the continuity equation identically. The remaining equations are:

$$(\rho\mu f'')' + 2ff'' = 0, \tag{1.7.19}$$

$$(\rho\lambda T')' + 2Pr_\infty C_P f T' + (\gamma_\infty - 1)M_\infty^2 Pr_\infty \rho\mu f''^2$$

$$+Pr_\infty Sc_\infty^{-1}\rho^2 D_{12}T' \sum_{i=1}^{n} C_{P,i}F_i' = 4xPr_\infty(C_p\rho f' T_x - \sum_{i=1}^{n} h_i^*\Omega_i^*) \tag{1.7.20}$$

$$(\rho^2 D_{12}F_1')' + 2Sc_\infty f F_1' = 4x(f'F_i + \sum_{j=1}^{n} \nu^{ij}\Omega_j), \tag{1.7.21}$$

$$\sum_{i=1}^{n} F_i = 1 \tag{1.7.22}$$

and

$$C_P = \sum_{i=1}^{n} C_{P,i}F_i. \tag{1.7.23}$$

.

1.8 Stability

Once the the solution to the governing equations is determined, a further analysis is to examine the stability of that solution (called the mean flow). The analysis envisions

each of the dependent variables; temperature, pressure and velocities being perturbed by an undetermined function in the form of (example for velocity):

$$U = u_{mean} + \Phi \exp\left[i(\alpha x - \omega t)\right], \tag{1.8.24}$$

where ω is the frequency of the perturbation, $c = \frac{\omega}{\alpha}$ is the wave speed and α the wave number, assumed to be complex. For spatial stability which is analyzed here, if the imaginary part of α is non-zero the disturbance will grow at $x \rightarrow \pm\infty$. These represent unstable perturbation modes. In analysis first proposed by Lees and Lin [9], stable perturbation modes are postulated to exist when a regularity factor is zero. In both the reduced chemical combustion section and the binary gas mixture studies, stability conditions will be considered.

1.9 Summary

Three laminar mixing problems are considered in this thesis:

- In the double vortex problem, the simple combustion model (1.1.1) is used. The system density is assumed constant; therefore, the transformed Navier-Stokes equations are not required. The transport properties are chosen to be constant with nominal and simplifying values. The flow streams have equal velocity and a moving coordinate system is chosen so that the velocities in the free stream are zero. This system is assumed to exist in its separated state until a pair of counter-rotating vortices are started. The vortex centers coincide with the initial gas interface. The vortices will enhance the mixing of the gases and effect

the combustion rate. This study investigates the ignition processes and time to ignition for various combination of system parameters.

- In the reduced chemical combustion study, the flow magnitudes are different on separate sides of the splitter plate. Again nominal and simplifying values are assigned the transport properties. Two chemical reduction systems are studied, one only slightly more complex than the model (1.1.1) and one complex. The system is assumed to be independent of time but the density is spatially dependent; therefore, the transformed Navier-Stokes equations are used. The combustion process is studied as a function of the distance downstream of the end of the splitter plate. Ignition and post ignition structure and stability are analyzed.

- In the study of the effects of differing molecular weights on the mixing layer, only the process of the gases mixing is studied. It is assumed that there is no combustion. The system is variable density, with different flow velocities. Only one real gas is initially in each flow field. Thirty combinations of six different gases are considered. The transport properties are calculated using available theory and data. This complete system is compared to model systems which use simpler approximations for the transport properties. The steady state of the mixing layer is calculated, and the stability of this steady state is studied.

Chapter 2

IGNITION DYNAMICS IN THE FIELD OF A VORTEX PAIR

2.1 Introduction

An important problem in the general area of non-premixed combustion is the theoretical study of chemical reactions in turbulent reacting flows. However, such flows are difficult to analyze because the governing equations are highly nonlinear, transient and involve a large number of parameters as well as a wide range of length and time scales. The large scales are essentially inviscid and are related to the geometric configuration of the flow. On the other hand, combustion takes place on the smaller scales associated with the diffusion of fuel and oxidizer into each other. It is on these smaller scales that theoretical work can be established in hope of gaining insight into the more complex larger problems. Marble [3], developed a simple model problem that locally describes an established thin flame wrapped up by a small scale

eddy. However, certain important aspects, such as ignition and flame structure, were not included within the framework of the Marble problem. A systematic analysis of the ignition process in vortex dominated flows using asymptotic methods and direct numerical simulation has been conducted by Macaraeg, Jackson, and Hussaini [4]. Additionally, Thevenin and Candel [10] conducted a similar analysis but allowed for much larger difference in temperature between the initially unmixed gases. The above igniton studies have been restricted to a single point vortex. Since counter-rotating vortex pairs are likely to occur in turbulent flow (and easily demonstrated by dragging a coffee stirrer through coffee), the effects of the vortex pair on the ignition processes should also be examined. Considered here is an ignition dynamics model with constant density, one-step Arrhenius reaction between initially unmixed species of fuel and oxidizer occupying adjacent half-planes. The fuel and oxidizer are allowed to mix and react in the presence of a pair of counter-rotating point vortices with centers located on the initial interface. Using large activation energy asymptotics, particular attention is paid to the ignition regime as a function of the vortex Reynolds number and the spacing between the vortices and the initial density ratios of the fuel and oxidizer. Where applicable, results are compared to the previous work with a single point vortex [4] and also with the similiar ignition study where no vortex is present (Linan and Crespo [11]).

2.2 Problem Formulation

Two gases F_1 and F_2 are initially at rest. At $t = 0$, two counter-rotating vortices are initiated. The vortices each produce a radial and angular velocity component with respect to their own centers $(\pm d, 0)$. Both radial velocities are zero. The individual angular velocities are:

$$V_{\pm d} = \frac{\pm RPr}{r_{\pm}}. \tag{2.2.1}$$

The density of the system is assumed constant, and the diffusion coefficients are taken as $D_i = 1$. The reaction mechanism used for this study is:

$$F_1 + F_2 \rightarrow PRODUCT + HEAT. \tag{2.2.2}$$

The simplified versions of equations (1.6.7) through (1.6.11) are written in cylindrical coordinates. The continuity equation reduces to an identity with the introduction of the stream function which is due to the combined flow of the two vortices. The velocities in terms of the streamfunction are

$$U = \frac{1}{r}\frac{\partial \Psi}{\partial \theta} \quad \text{and} \quad V = -\frac{\partial \Psi}{\partial r}. \tag{2.2.3}$$

with (U, V) being the radial and angular velocity components, respectively. The particular streamfunction for the vortices given by (2.2.1) and expressed in Cartesian coordinates (x, y) is

$$\Psi = -\frac{RPr}{2} \ln\left[\frac{(x-d)^2 + y^2}{(x+d)^2 + y^2}\right]. \tag{2.2.4}$$

The other equations simplify to:

$$T_t + UT_r + \frac{V}{r}T_\theta = \nabla^2 T + \beta\Omega \tag{2.2.5}$$

and

$$F_{j,t} + UF_{j,r} + \frac{V}{r}F_{j,\theta} = \frac{1}{Le_j}\nabla^2 F_j - \Omega, \qquad j = 1,2, \tag{2.2.6}$$

where

$$\Omega = DaF_1F_2e^{-Ze/T} \tag{2.2.7}$$

and ∇^2 is the two-dimensional Laplacian operator in cylindrical coordinates; T is the temperature; and F_1 and F_2 are the mass fractions of the fuel and oxidizer, respectively. The chemical reaction is modeled as a one-step irreversible Arrhenius reaction. The nondimensional parameters appearing above are

$R = \Gamma/2\pi\nu$	vortex Reynolds number,
$Pr = \mu C_p/\lambda$	Prandtl number,
$Ze = E/(R^oT_\infty)$	Zeldovich number,
Da	Damkohler number,
$Le_j = Sc_j/Pr$	Lewis number for species j,
$Sc_j = \nu/D_j$	Schmidt number for species j

and

β	Heat release per unit mass of F_1

with Γ being the circulation of the vortex, $\nu = \mu/\rho$ is the kinematic viscosity, μ is the viscosity, ρ is the density that is assumed constant, λ is the thermal conductivity, C_p is the specific heat at constant pressure, E is the dimensional activation energy, R^o is the universal gas constant and D_j is the species diffusion coefficient. The Damkohler number is defined as the ratio of the characteristic diffusion time scale

to the characteristic chemical time scale. The temperature and mass fractions were nondimensionalized by the values T^*_∞ and $F^*_{1,\infty}$, respectively. The velocities were nondimensionalized by U_o, some characteristic speed. Lengths and times are referred to the relevant diffusion characteristic scales $l_d = \lambda^*/\rho^* C^*_p U^*_o$ and l_d/U_o of the flow, respectively. These equations are to be solved subject to appropriate initial and boundary conditions given in the appropriate sections below. All of the calculations to be presented use unit Prandtl number.

2.3 Convection Analysis

Analysis of the convection-only flow that would be induced by the combined interaction of the two vortices can give insight to the full convective-diffusive system. Circulation times associated with the convection can be used to evaluate the system ignition times. Convective streamlines and circulation periods are developed below.

The total velocity in the x and y directions as a result of the interaction of the two vortices can be shown to be:

$$v_x = \frac{-4dRxy}{[(x-d)^2+y^2][(x+d)^2+y^2]} \tag{2.3.8}$$

and

$$v_y = \frac{2dR(x^2-y^2-d^2)}{[(x-d)^2+y^2][(x+d)^2+y^2]}. \tag{2.3.9}$$

Dividing equation (2.3.8) by equation (2.3.9) yields the differential equation

$$\frac{v_x}{v_y} = \frac{\frac{dx}{dt}}{\frac{dy}{dt}} = \frac{dx}{dy} = \frac{-2xy}{x^2-y^2-c^2} \tag{2.3.10}$$

which has a solution:

$$(x - x_d)^2 + y^2 = x_d^2 - d^2. \tag{2.3.11}$$

Thus, the convection flow has circular streamlines. The streamline through the arbitrary point (x, y) lies on a circle with center $(x_d, 0)$ and radius

$$r^2 = x_d^2 - d^2. \tag{2.3.12}$$

Clearly there are an infinite number of convection circles. The convective flow induced by the double vortex can now be understood by calculating the angular and radial velocity at a point (x, y) with respect to the point $(x_d, 0)$.

The radial velocity is :

$$U_{x_d} = 2ydR\frac{x^2 - y^2 - d^2 - 2x(x - x_d)}{((x-d)^2 + y^2)((x+d)^2 + y^2)((x - x_d)^2 + y^2)^{\frac{1}{2}}}. \tag{2.3.13}$$

Using equation (2.3.12), it is seen that the numerator in equation (2.3.13) is equal to zero, consistent with circular flow. The angular velocity is given by

$$V_{x_d} = 2Rd\frac{y^2(x + x_d) + (x^2 - d^2)(x - x_d)}{((x-d)^2 + y^2)((x+d)^2 + y^2)((x - x_d)^2 + y^2)^{\frac{1}{2}}}. \tag{2.3.14}$$

Using equation (2.3.12) this reduces to

$$V_{x_d} = \frac{dR}{xr}. \tag{2.3.15}$$

Since $V_{x_d} = r\dot{\theta}$,

$$\dot{\theta} = \frac{dR}{xr^2} = \frac{dR}{(rcos(\theta) + x_d)r^2} \tag{2.3.16}$$

and the rotation time is given by

$$t = \int_{\theta_0}^{\theta_1} \dot{\theta} dt. \tag{2.3.17}$$

This gives a period of rotation of

$$T = \frac{2\pi x_d r^2}{dR}. \tag{2.3.18}$$

If the point $(x_0, 0)$ is defined as the x-intercept of the flow circle with $x_0 = x_d - r$, then substitution into (2.3.12) and (2.3.18) yields

$$r = \frac{d^2 - x_0^2}{2x_0}, \quad x_d = \frac{x_0^2 + d^2}{2x_0} \quad \text{and} \quad T = \frac{\pi(d^2 - x_0^2)^2(x_0^2 + d^2)}{4dRx_0^3}. \tag{2.3.19}$$

The convection flow can now be viewed as a series of nonintersecting eccentric circles with periods and radii dependent only on the vortex spacing d and the location of the x-intercept nearest to $x = 0$. Figure 2.1 shows the period as a function of the near zero x-intercept for R values 20, 15, 10 and 5 from left to right. Figure 2.2 shows various streamlines for $d = 3$ clearly demonstrating the eccentric nature. These streamlines are independent of R which only effects the speed of the convection flow around the streamlines. In what follows, the full convective-diffusion results will be compared with the purely convective flow discussed above.

2.4 Ignition Asymptotic Analysis

At time $t = 0$, the reaction rate is exactly zero since the product F_1F_2 has a value of zero everywhere. For $t > 0$, the fuel and oxidizer mix by diffusion and by the convection induced by the vortex pair. Thus, the product F_1F_2 and the reaction rate are no longer zero. For small time, it is reasonable to assume that the effect of the reaction on the overall flow field is small. So, the solution for small time is near the inert or chemically frozen solution which is denoted by the superscript I. In what

follows, the only case considered is the case with the fuel and the oxidizer having near equal initial temperatures. This assumption leads to the inert temperature having the form $T^I = 1 + O(Ze^{-1})$, where the $O(Ze^{-1})$ term is included to allow for small initial temperature differences between the fuel and the oxidizer. As time increases, the combustibles continue to mix and the reaction rate increases until, at some finite time, a thermal explosion occurs characterized by significant departure from the inert solution. To analyze this ignition process, the effect of the growing reaction rate is determined by expanding the dependent variables about the inert solution as

$$T = 1 + Ze^{-1}T_1 + O(Ze^{-2}) \tag{2.4.20}$$

and

$$F_j = F_j{}^I + O(Ze^{-1}). \tag{2.4.21}$$

Taking the asymptotic limit $Ze \to \infty$, the leading-order equations are given by

$$T_{1,t} + UT_{1,r} + \frac{V}{r}T_{1,\theta} = \nabla^2 T_1 + F_1^I F_2^I e^{T_1} \tag{2.4.22}$$

and

$$F_{j,t}^I + UF_{j,r}^I + \frac{V}{r}F_{j,\theta}^I = \frac{1}{Le_j}\nabla^2 F_j^I \qquad j = 1,2 \tag{2.4.23}$$

where the Damkohler number Da has been chosen to be

$$Da = \frac{e^{Ze}}{\beta Ze}. \tag{2.4.24}$$

This particular choice of the Damkohler number ensures that a distinguished limit exists, that is, the reaction rate term is of the same order in a Zeldovich number expansion as the time derivative terms. The appropriate boundary and initial conditions

are given by

$$FUEL \quad SIDE: \qquad T_1 = 0, \quad F_1^I = 1, \quad F_2^I = 0 \qquad (2.4.25)$$

and

$$OXIDIZER \quad SIDE: \qquad T_1 = \beta_T, \quad F_1^I = 0, \quad F_2^I = \phi^{-1} \qquad (2.4.26)$$

where ϕ is the equivalence ratio defined as the ratio of the mass fraction of the fuel (species 1) to the mass fraction of the oxidizer (species 2) divided by the ratio of their molecular weights times their stoichiometric coefficients. The parameter β_T allows for small initial temperature differences. If $\phi = 1$, the mixture is said to be stoichiometric, if $\phi > 1$ it is fuel rich, and if $\phi < 1$, it is fuel lean. Also, if β_T is less than zero, the oxidizer is relatively cold compared to the fuel, and if β_T is greater than zero, it is relatively hot.

2.5 Numerical Techniques

The equations (2.4.22) and (2.4.23) are solved numerically for a range of R. Implementation of the boundary conditions is facilitated if the system is recast in Cartesian coordinates (x, y). The solution technique is a 2nd-order finite-difference scheme on a nonuniform mesh with a four-stage Runge-Kutta time-stepping scheme that is formally 2nd-order but has an extended stability region making it accurate and robust for solving moderately stiff problems [4]. Two coordinate stretching forms are used to resolve the structure near and between the vortex centers. The stretching in the y-direction is similiar to that employed by [4]. The stretching in the x-direction requires

a form that has a fine grid size between and near the vortex centers, a coarse grid as $x \rightarrow x_{max}$, and preserves the symmetry of the problem. The dx sizing is provided by choosing a minimum dx to be placed at the vortex center and then changing the dx as a function of x according to:

$$dx(x_i+dx) = dx(x_i)\frac{1+z^2+b(z^2-1)(z^2-2)\exp(\frac{x^2}{x_{max}^2})}{1+c(z^2-1)^2(z^2-2)^2}, \quad x_{i+1} = x_i+dx \quad (2.5.27)$$

where $z = x/d$ is the variable x normalized by the vortex center and c is selected to limit the ratio of $dx(x = 0)$ and $dx(x = d)$. The solution to the system (equations 2.4.22 and 2.4.23) is advanced in time from the initial conditions using the Runga-Kutta scheme. Grid resolution studies that at least doubled the computational mesh were carried out to ensure that all of the structures were well resolved.

2.6 Results

As t increases, the solution for the temperature perturbation T_1 becomes unbounded at some finite time (t_{ig}) and location (x_{ig}, y_{ig}). This defines the ignition time. Ignition times are presented below as a function of the various parameters: (i) vortex spacing, (ii) equivalence ratio, (iii) temperature ratio and (iv) Lewis number. Whenever appropriate, results are compared to the classical result of Linan and Crespo [11] in which the reactants mix by diffusion only in the absence of any vortex and with that of a corresponding potential point vortex centered at the origin of the coordinate system having velocities

$$U = 0 \quad \text{and} \quad V = \frac{R}{r} \quad (2.6.28)$$

as discussed in [4].

2.6.1 Comparison of Ignition Times of a Single vs a Double Vortex

Figure 2.3 shows the nondimensional ignition time for the double vortex as a function of the vortex Reynolds number R for $\phi = Le_j = Pr = 1$, $\beta_T = 0$ and for vortex centers at $d = 3$ ($\triangle$) and $d = 4$ ($\square$). The nondimensional ignition times corresponding to the vortex pair lay between that of no vortex (Linan and Crespo case) denoted by the solid line and that of the potential point vortex ($\diamond$) described in [4]. That the ignition in the presence of a double vortex will proceed more slowly than in the presence of a single vortex when the vortex Reynolds number is the same in both cases is a somewhat unexpected result.

As was shown, the convective flow for the two cases is very different. The single vortex has streamline circles which are concentric and the angular velocity around a circle is constant. The interaction of the two vortices causes streamline circles which are eccentric with an angular velocity that varies around the circle. It is easily envisioned that the flow is faster between the vortices where the flow from the individual vortices is additive and likewise slower on the the outside ($x < -d$ and $x > d$) where the flows are opposing each other. Where as the single vortex tends to produce a maximum of the product F_1F_2 in the center of the vortex [4], the double vortex produces a maximum of the product F_1F_2 at an eccentric location.

For these cases where $\beta_T = 0$, the heat convection is not significant during the

early stage of the mixing. Also with $\beta_T = 0$, the diffusion of heat will proceed differently than the diffusion of F_1 and F_2 which are completely separated at the start of the analysis. The importance of temperature to the difference in single versus double ignition times will be presented shortly. Additionally, figures will show that the elevated temperature surfaces will wrap around the double vortices centers; whereas, for the single vortex the maximum of the product F_1F_2 and the high temperature point always occur at the center of the vortex. As will be shown, for low Reynolds numbers these two quantities are in an eccentric location and for higher values of R, the temperature maximum is in the center while the F_1F_2 high point is still eccentric. The fact that ignition takes place where the F_1F_2 product is low should be attributed to the exponential temperature dependence of the Arrhenius reaction rate. An interim case will exist with two hot spots; one at the high F_1F_2 point and one at the center of the vortex.

2.6.2 Effects of Vortex Spacing

Figure 2.3 shows that the difference in ignition times between the single and double vortex is less for $d = 4$ than for $d = 3$. To further investigate the influence of the vortex spacing on ignition, Figure 2.4 shows a plot of the nondimensional ignition time as a function of vortex spacing for $R = 20$. The limit $d = 0$ is the Linan and Crespo result since the counter-rotating vortices cancel as the spacing goes to zero. As the spacing increases, the nondimensional ignition time for the double vortex ($\square$) approaches that of the potential point vortex since the velocity fields associated with each vortex of the vortex pair have a reduced effect on each other.

2.6.3 Effects of Vortex Reynolds Number

In Figure 2.3, it appears that as the Reynolds number increases from zero there are three distinct regions which is clearly different than in the single vortex case. When the Reynolds number is small, the interaction between the pair of vortices is slight and the vortex strength is small. This region could be referred to as vortex assisted diffusion. As the Reynolds number increases there is a stronger interaction between the pair. The interaction is sufficient to prevent ignition at the vortex center before an asymmetric ignition takes place. For even larger Reynolds numbers, the interaction between the vortices is still strong, but each vortex is strong enough to cause ignition at the center before an asymmetric ignition is possible. The shift of the ignition point as Reynolds number increases is apparent from Figure 2.5 which shows the isotherms of the temperature perturbation at the time of ignition for R values 5, 10, 15 and 20. For $R = 5$ and $R = 10$, the ignition point is not at the center of the vortex, and the ignition point shows a slight counterclockwise movement for the larger Reynolds number. With $R = 15$, the ignition is still away from the vortex center, but a second hot spot is beginning to be established at the center of the vortex. The two temperature peaks are shown in Figure 2.6 which is the temperature surface for $R = 15$ and $d = 3$. In the last frame in Figure 2.5, the ignition is occurs at the center of the vortex for $R = 20$ which is the final region in Figure 2.4. This is dramatically illustrated in Figure 2.7 where the temperature hot spot is clearly established at the center of the vortex. Also of note is the elevated temperature along the diffusion front that spirals about the vortex center. Figure 2.8 shows the contours

of the mass fraction F_1^I at ignition for the double vortex with $d = 3$, $\beta_T = 0$, and $\phi = Le_j = Pr = 1$. (The contours are enhanced to show the location of the $F_1^I \approx 0.5$ levels). For $R = 5$, the interface does not move far from the center of the vortex before ignition; for higher values of R, there is more of a wrap around effect.

2.6.4 Effect of Equivalence Ratio

Figure 2.9 is a plot of the nondimensional ignition times for the potential point vortex ($\Box$), for the double vortex ($\Diamond$) with centers $(\pm 4, 0)$, and for no vortex ($\triangle$), as a function of the equivalence ratio ϕ with $R = 20$, $Le_j = Pr = 1$ and $\beta_T = 0$. In all three cases, the nondimensional ignition time is delayed significantly for fuel rich mixtures ($\phi > 1$), while the nondimensional ignition time is enhanced for fuel lean mixtures ($\phi < 1$). The double vortex ignition times lie between the single vortex and no vortex ignition times as previously explained.

2.6.5 Effect of Temperature Ratio

Figure 2.10 shows the nondimensional ignition time for the potential point vortex, for the double vortex with centers $(\pm 4, 0)$, and for no vortex, as a function of the temperature ratio β_T with $R = 20$ and $\phi = Le_j = Pr = 1$. Recall that the nondimensional ignition times for the no vortex case are those obtained by Linan and Crespo [11]. In all three cases, the nondimensional ignition time is delayed significantly when the temperature of the oxidizer is less than that of the fuel ($\beta_T < 0$), while the nondimensional ignition time is enhanced when the temperature of the oxidizer is greater

than that of the fuel ($\beta_T > 0$). As β_T increases from zero, the nondimensional ignition times for all three cases become essentially indistinguishable. For a large β_T the immediate result of the convective mixing is homogenizing the temperature in the center of the vortex. This reduces the central temperature and asymetric ignitions take place as discussed in [4]

2.6.6 Effect of Lewis Number

To investigate the effect of the Lewis number on ignition, the nondimensional ignition time as a function of the Lewis number $Le_j = Le$ for $\beta_T = -2$ ($\diamond$), $\beta_T = 0$ ($\square$), and $\beta_T = 2$ ($\triangle$) with $R = 0$ and $\phi = Pr = 1$ is shown in Figure 2.11. These results correspond to the case where no vortex is present and mixing is achieved by diffusion alone. Linan and Crespo [11] did not consider this non-unity Lewis number case in their analysis. The largest effect occurs for $\beta_T = -2$ since the nondimensional ignition time is delayed thereby allowing diffusion to play a more dominant role. The combined effect of equivalence ratio and Lewis number is determined by examining Figure 2.9 together with Figure 2.11. Since fuel rich mixtures delay ignition, diffusion becomes more important and thus the effects of non-unity Lewis numbers become noticable. For fuel lean mixtures, the nondimensional ignition time is shortened, the reactants have not had much time to diffuse, and thus non-unity Lewis numbers do not significantly alter the nondimensional ignition time. These trends persist even when a potential point vortex or a double vortex is introduced at time $t = 0$ since the effect of convection is to only somewhat reduce the overall nondimensional ignition time.

2.6.7 Effects of Convection

The ignition time along with the convective flow analysis allows insight into the mixing of the species. From Figure 2.3, the ignition time for $d = 3$ and $Re = 20$ is approximately 5.6. At $Re = 20$, a convective circle with center $(x_d, 0) = (4.65, 0)$, radius $r = 3.55$, and intersecting the x-axis at $x = 1.1$ has a period equal to the ignition time (see Figure 2.1). A fluid element starting at any point inside this circle has been recirculated at least once before ignition, conversely a fluid element starting outside this circle does not experience one cycle of circulation before ignition. Figure 2.12 shows the effects of convection on equally spaced fluid elements starting at $y = 0$ and $0 < x < 3$ at $t = 0$ and the streamline circle defining the recirculation region, superimposed on the contours of F_2 at time of ignition. The vortex center is marked by a cross. It appears that the diffusion interface defined by $F_1^I = 0.5$ follows the convection of the fluid elements closely if the original elements lay outside of the recirculation circle and on a convection circle with radius much greater than the recirculation circle. However, inside the recirculation circle there would be many layers of fuel and oxidizer in the absence of diffusion, each layer being thinner as the vortex center is approached. Diffusion will eliminate the interface between the layers near the vortex center, leaving behind an almost constant mixture of fuel and oxidizer. If the product $F_1 F_2$ is large enough at the vortex center, then ignition will take place there, as it does for $R = 20$. For the region $x >> d$, the convective flow is much slower and only slightly effects the diffusion interface.

2.7 Conclusion

Presented here is a study of the influence of the hydrodynamical and physiochemical parameters on the ignition time and flame structure assuming a one-step, irreversible Arrhenius reaction between initially unmixed species occupying adjacent half-planes which are then allowed to mix and react by convection and diffusion in the presence of a vortex pair. In particular, the nondimensional ignition time is enhanced when (i) the vortex Reynolds number is increased from zero, (ii) the mixture is fuel lean, or (iii) the oxidizer is initially hotter than the fuel. The ignition time approaches that of a potential point-vortex as the vortex spacing increases. The effect of non-unity Lewis numbers on ignition is greatest when the ignition times are delayed, since diffusion then plays a more dominant role. In all cases, the ignition time obtained for the double vortex is between the case when no vortex is present and the case when a potential point vortex is located at the origin.

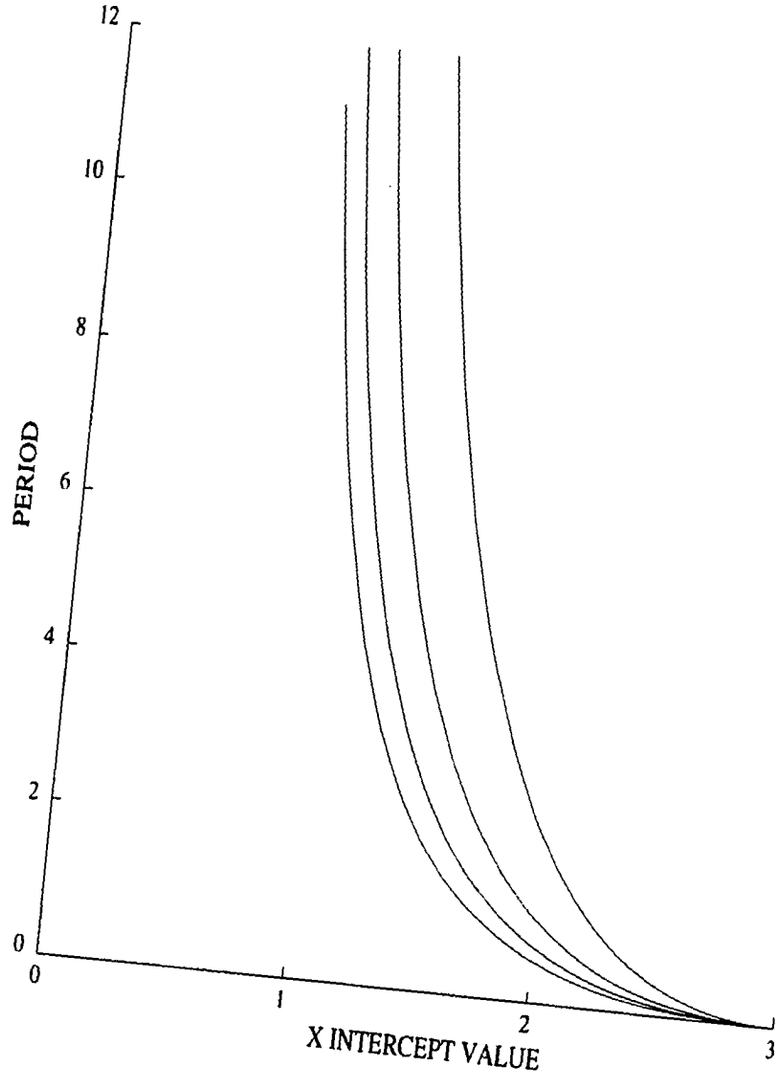

Figure 2.1: Streamline circle periods for $R = 20,\ 15,\ 10$ and 5 (left to right) vs x intercept.

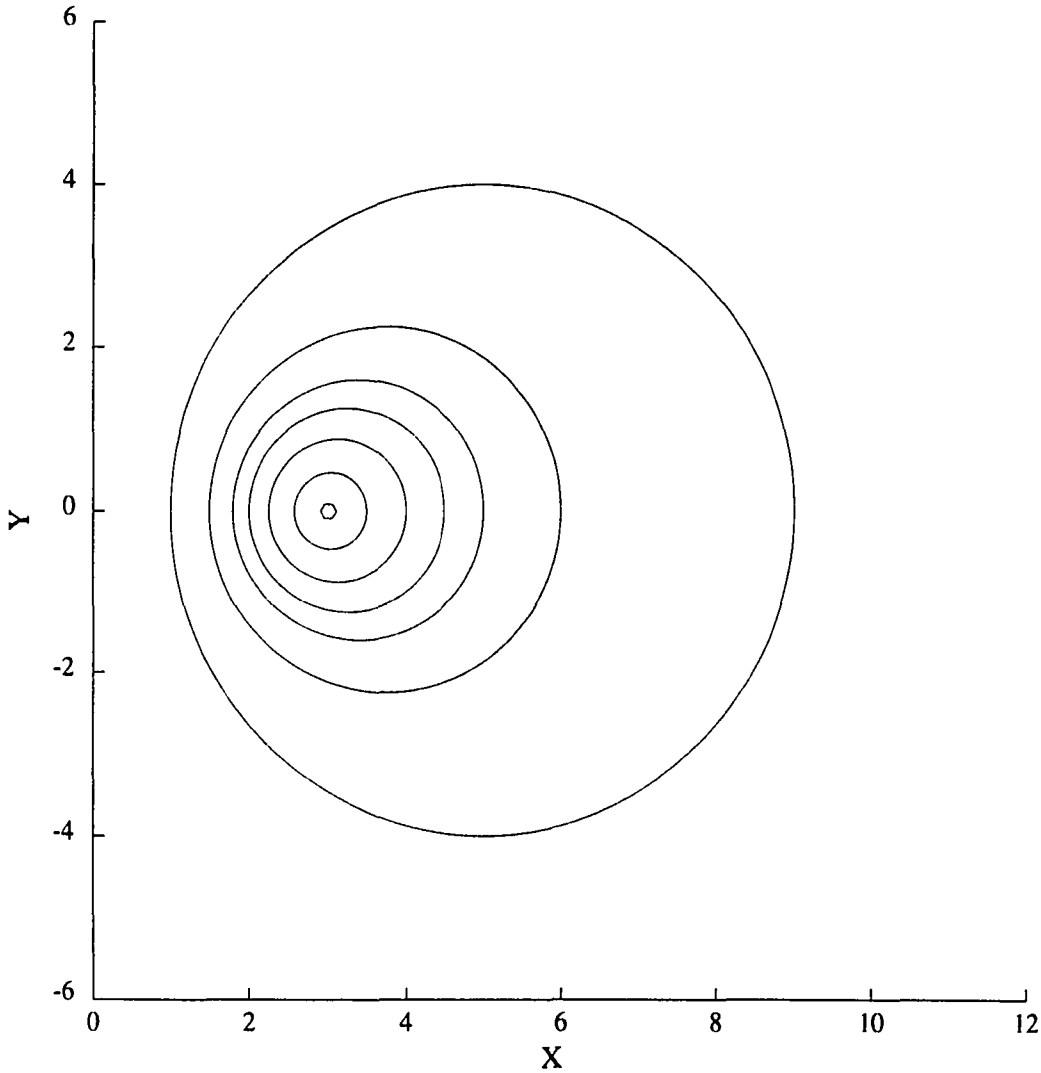

Figure 2.2: Eccentric streamline circles for d=3.

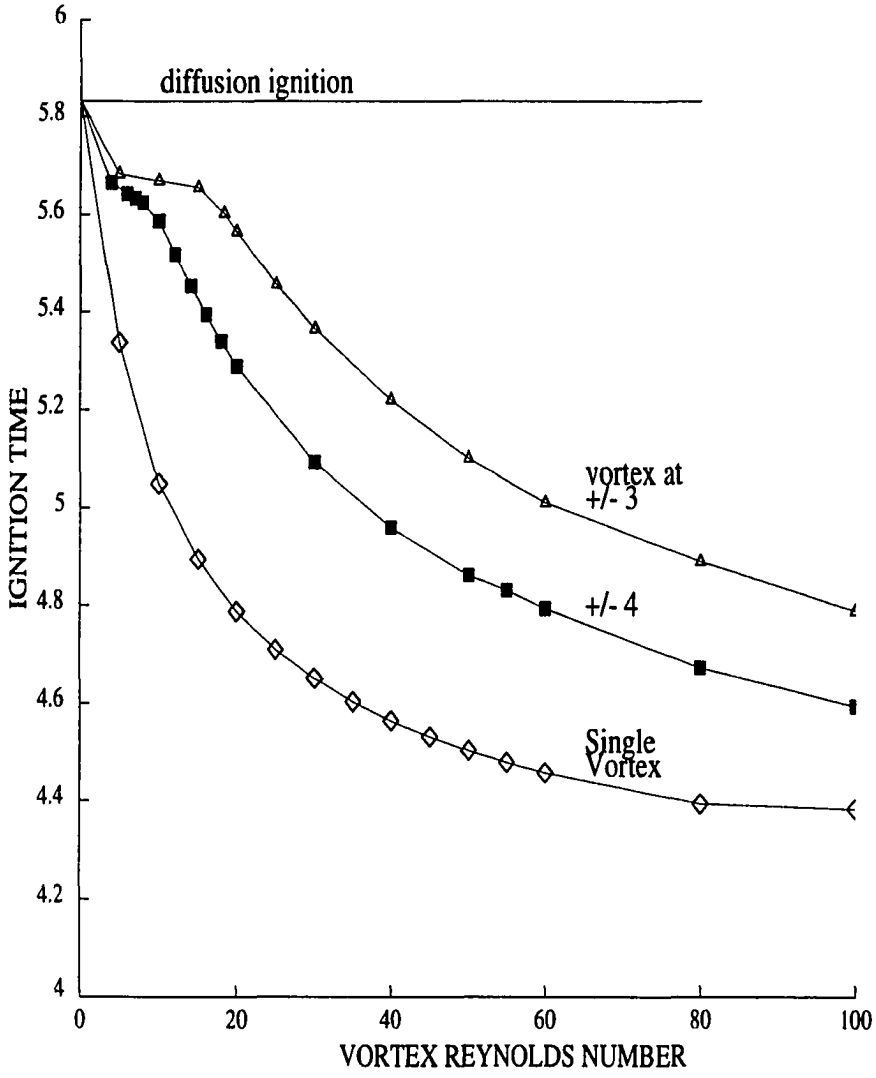

Figure 2.3: Nondimensional ignition times as a function of the vortex Reynolds number R for $\beta_T = 0$, $\phi = Le_j = Pr = 1$ and for vortex spacings $d = 3$ ($\triangle$) and $d = 4$ ($\square$).

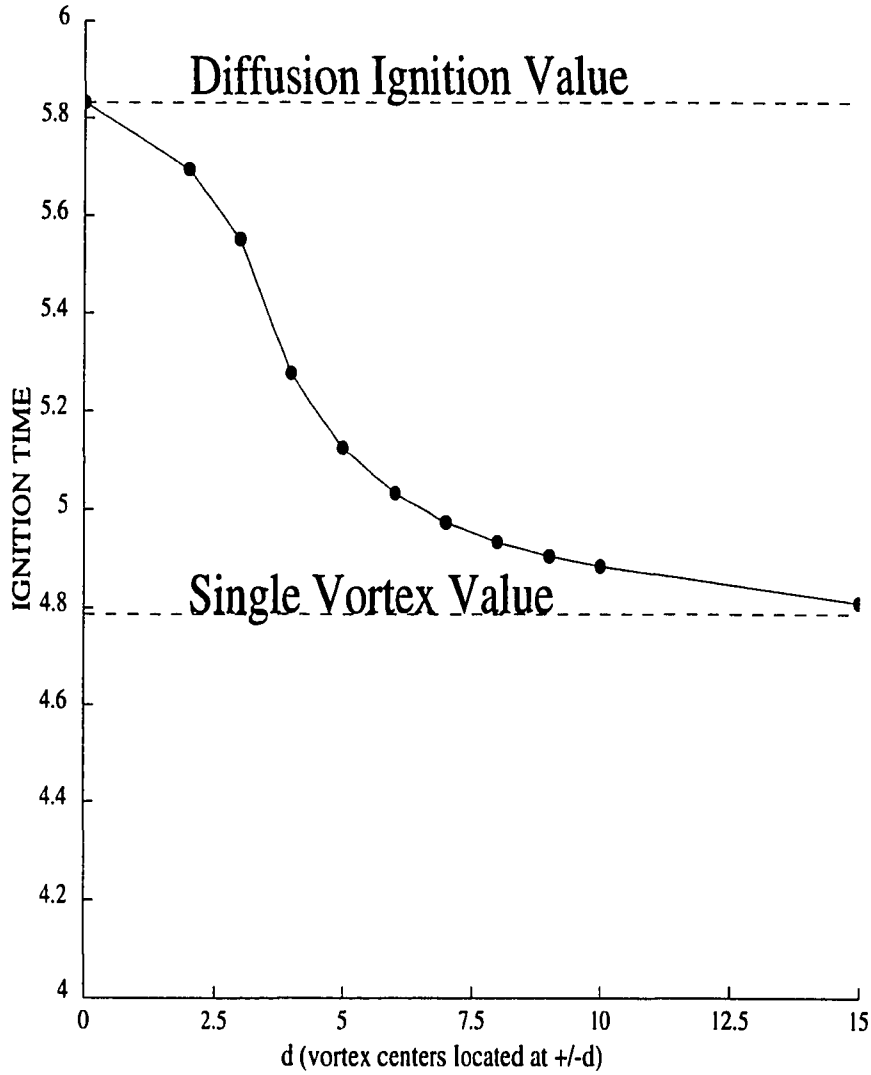

Figure 2.4: Nondimensional ignition times as a function of vortex spacing d for $R = 20$, $\beta_T = 0$, and $\phi = Le_j = Pr = 1$.

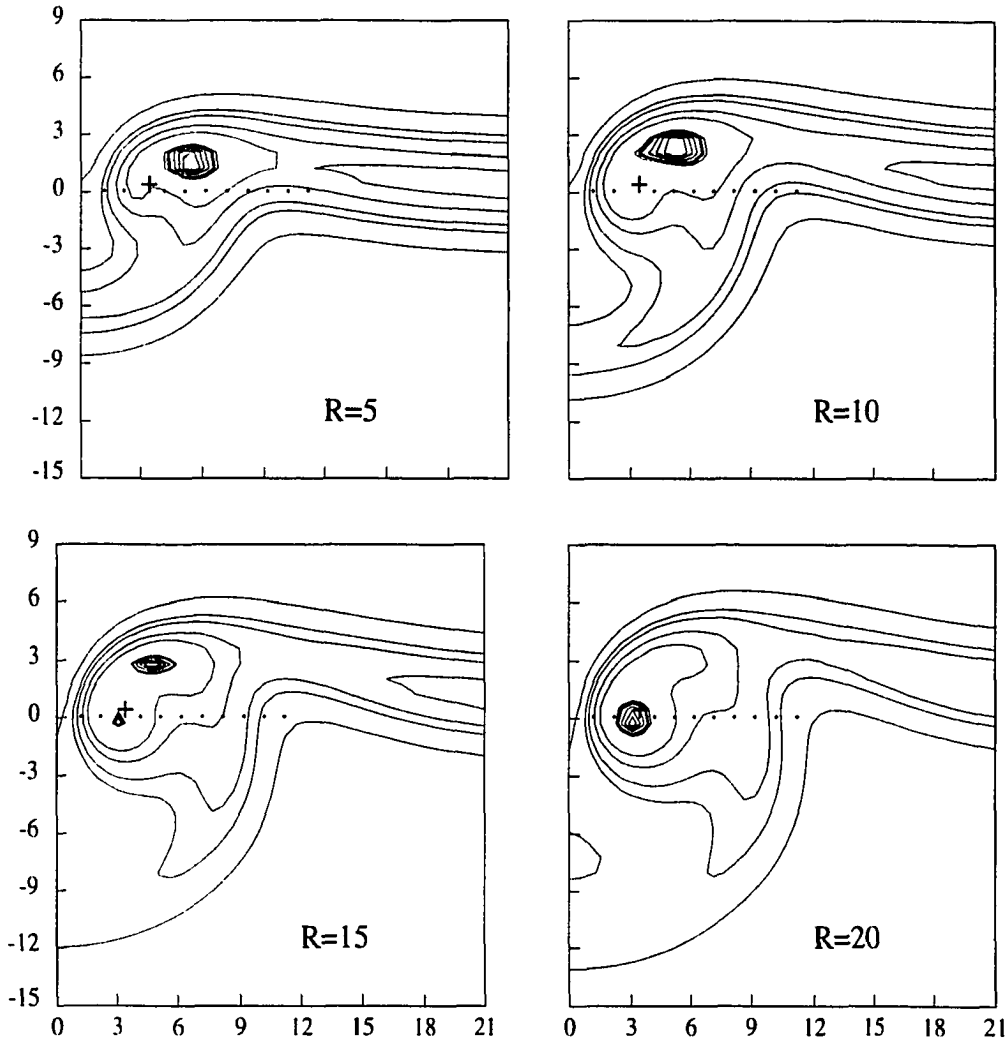

Figure 2.5: Isotherms of the temperature perturbation at ignition for the double vortex with center at $d = 3$ and for vortex Reynolds numbers of R=5, R=10, R=15 and R=20, with $\beta_T = 0$,and $\phi = Le_j = Pr = 1$.

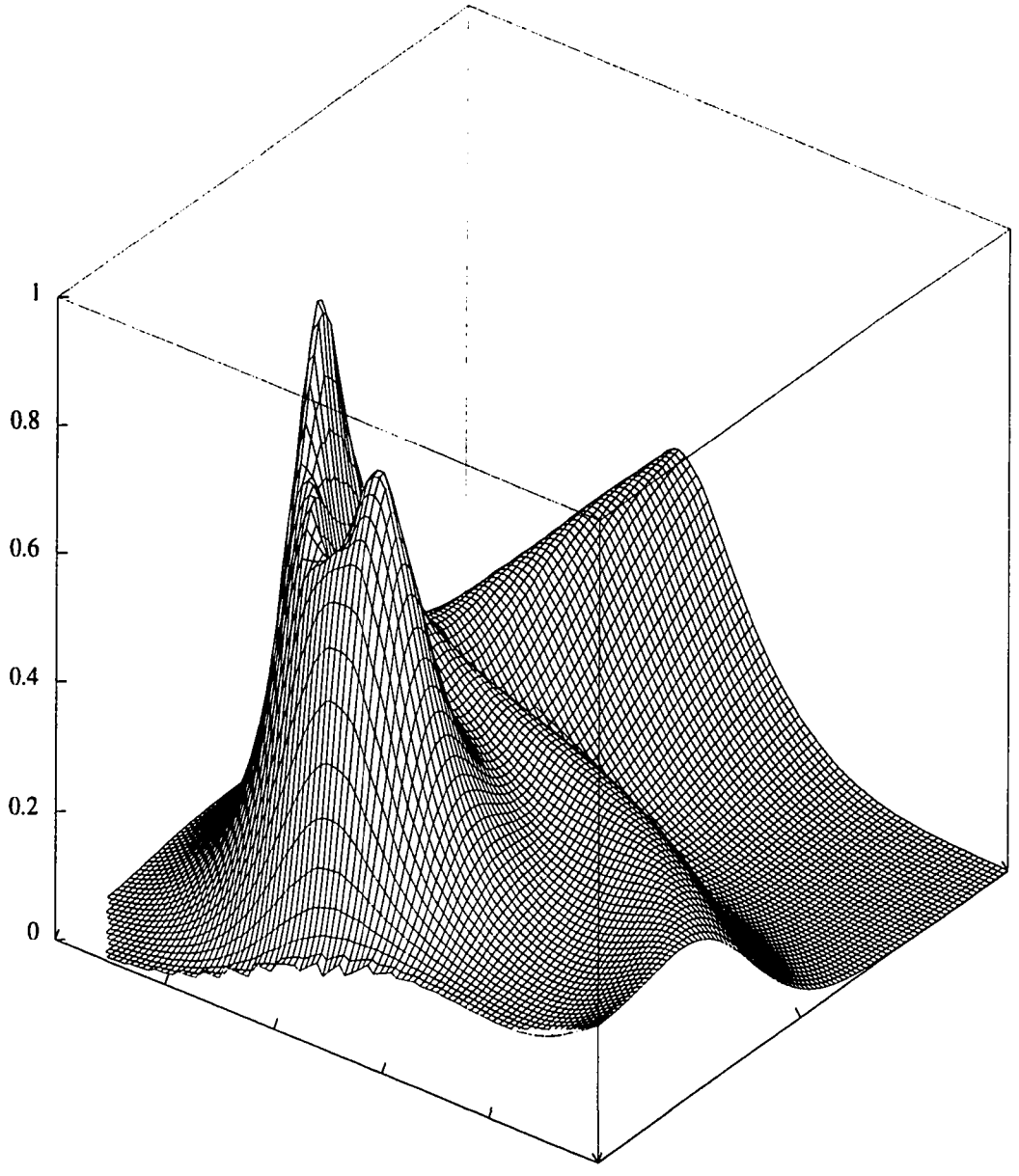

Figure 2.6: Temperature surface at ignition for d=3, R=15, $\beta_T = 0$, and $\phi = Le_j = Pr = 1$.

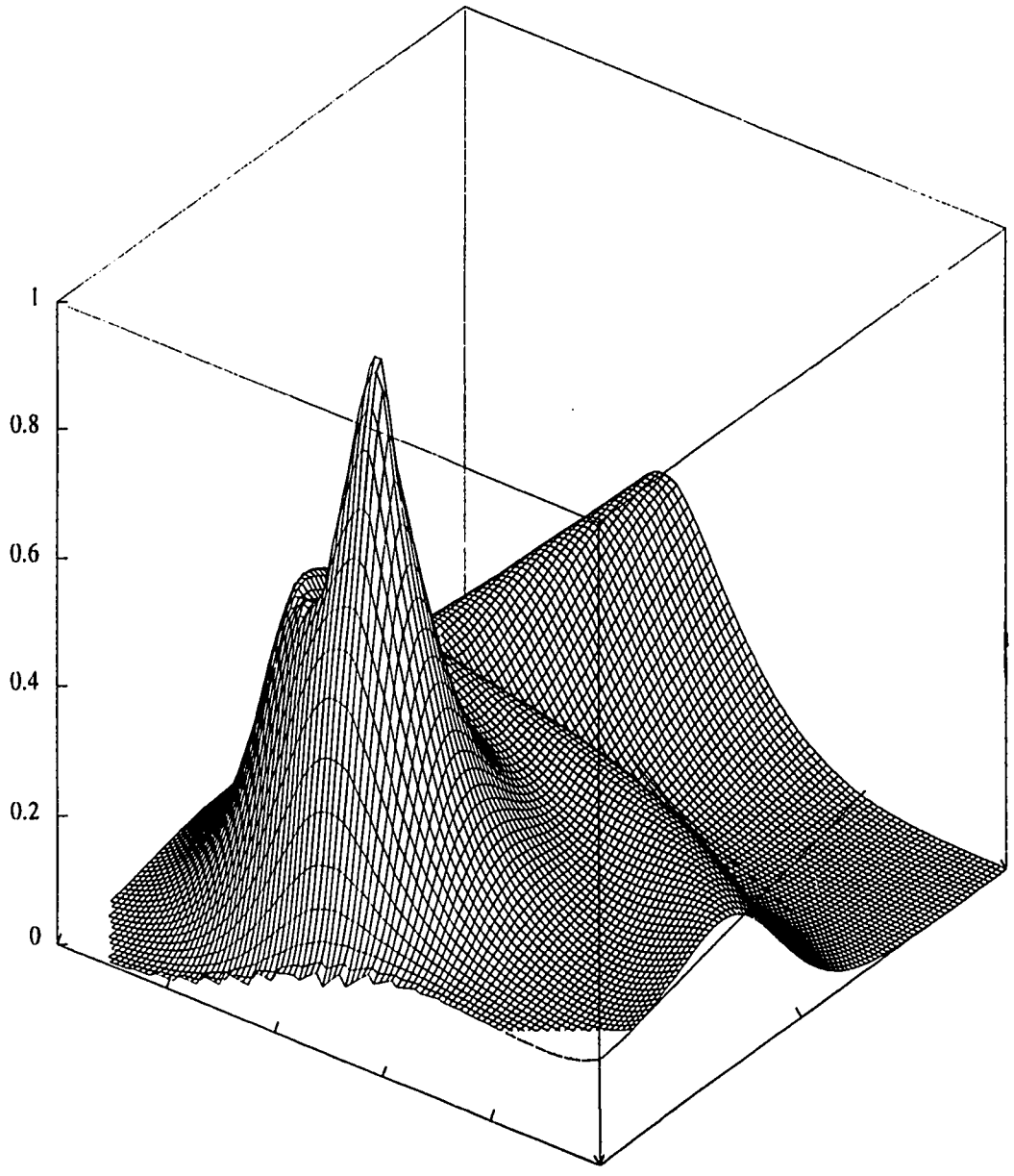

Figure 2.7: Temperature surface at ignition for d=3, R=20, $\beta_T = 0$, and $\phi = Le_j = Pr = 1$.

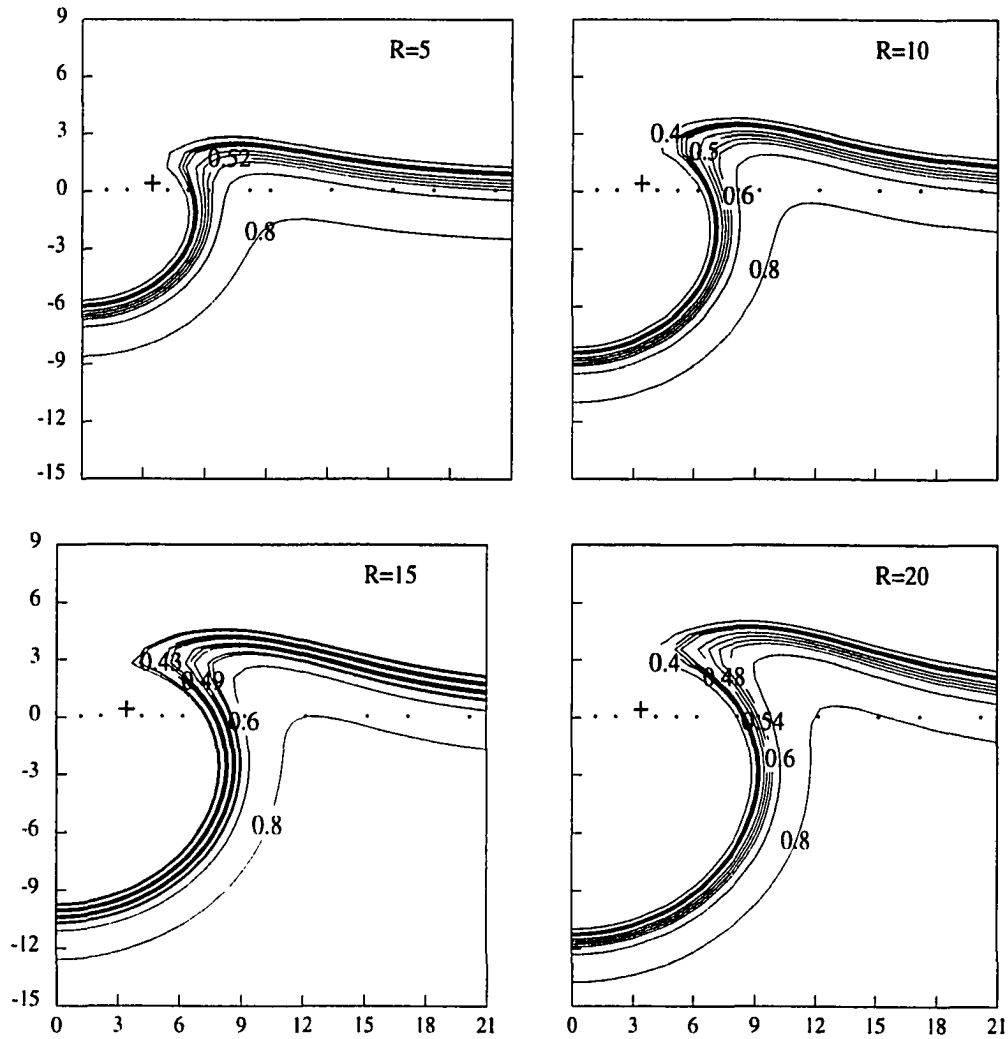

Figure 2.8: Contours of the fuel mass fraction F_1^I at ignition for the double vortex with center at $d = 3$, $\beta_T = 0$, and $\phi = L\epsilon_j = Pr = 1$.

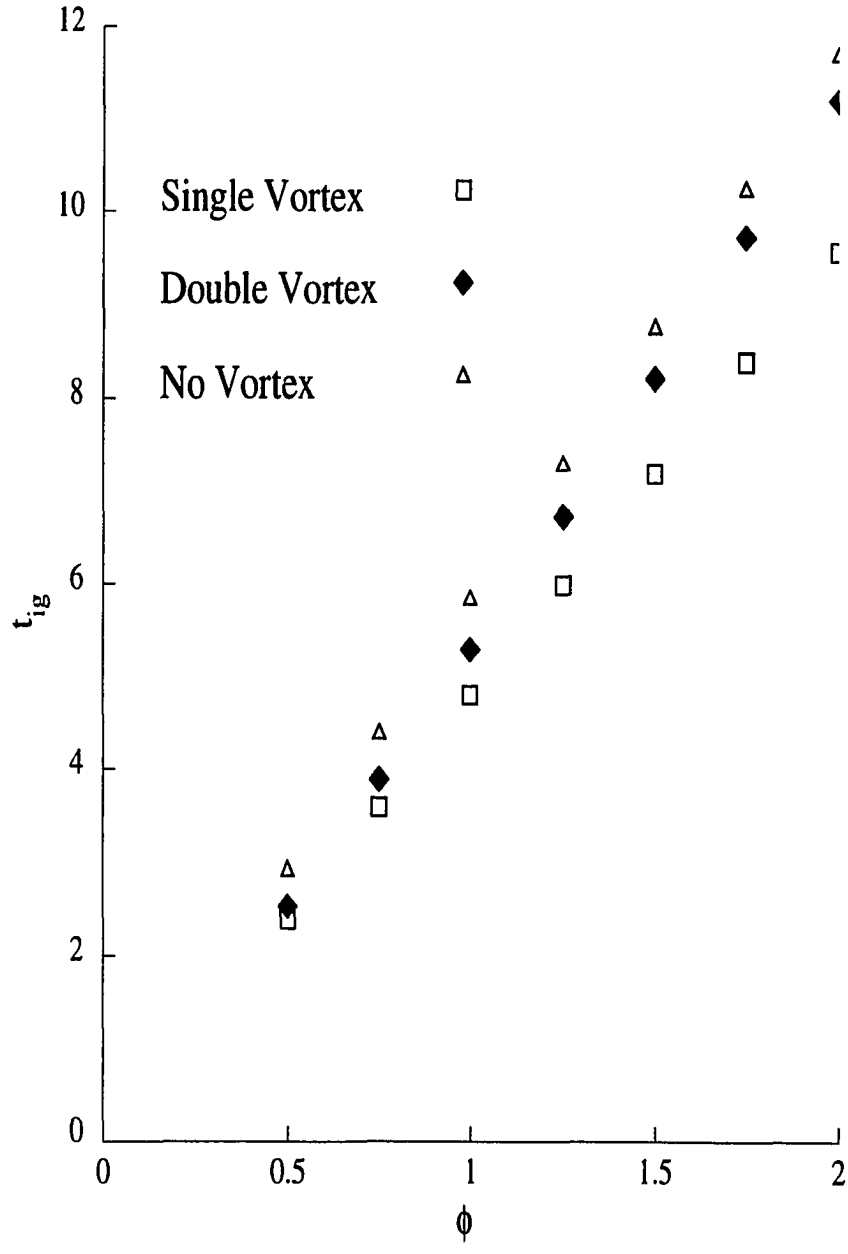

Figure 2.9: Nondimensional ignition times as a function of the equivalence ratio ϕ with $R = 20$, $\beta_T = 0$ and $Le_j = Pr = 1$.

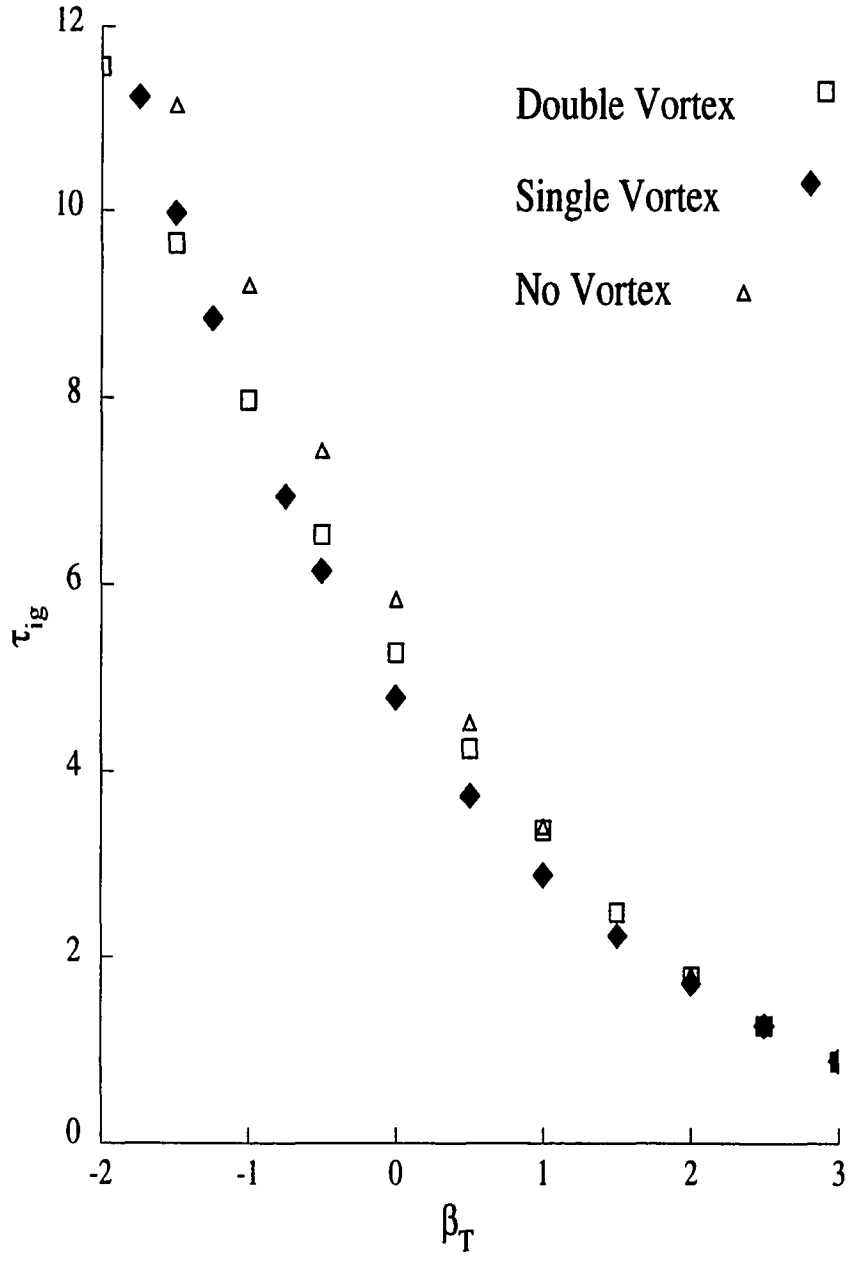

Figure 2.10: Nondimensional ignition times for a single vortex, for a double vortex with R=20 and for no vortex (R=0) as a function of the temperature ratio β_T with $R = 20$ and $\phi = Le_j = Pr = 1$.

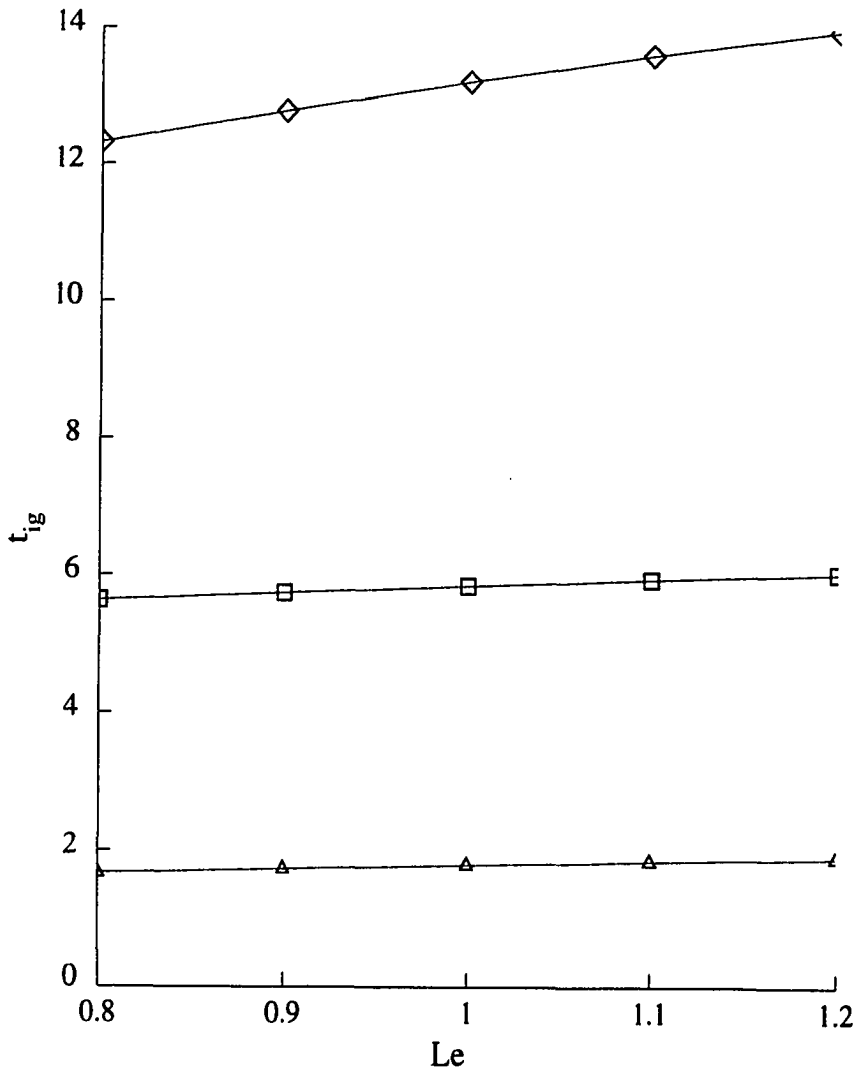

Figure 2.11: Nondimensional ignition times as a function of the Lewis number $Le_j = Le$ for $\beta_T = -2$ ($\diamond$), $\beta_T = 0$ ($\square$) and $\beta_T = 2$ ($\triangle$) with $R = 0$ and $\phi = Pr = 1$.

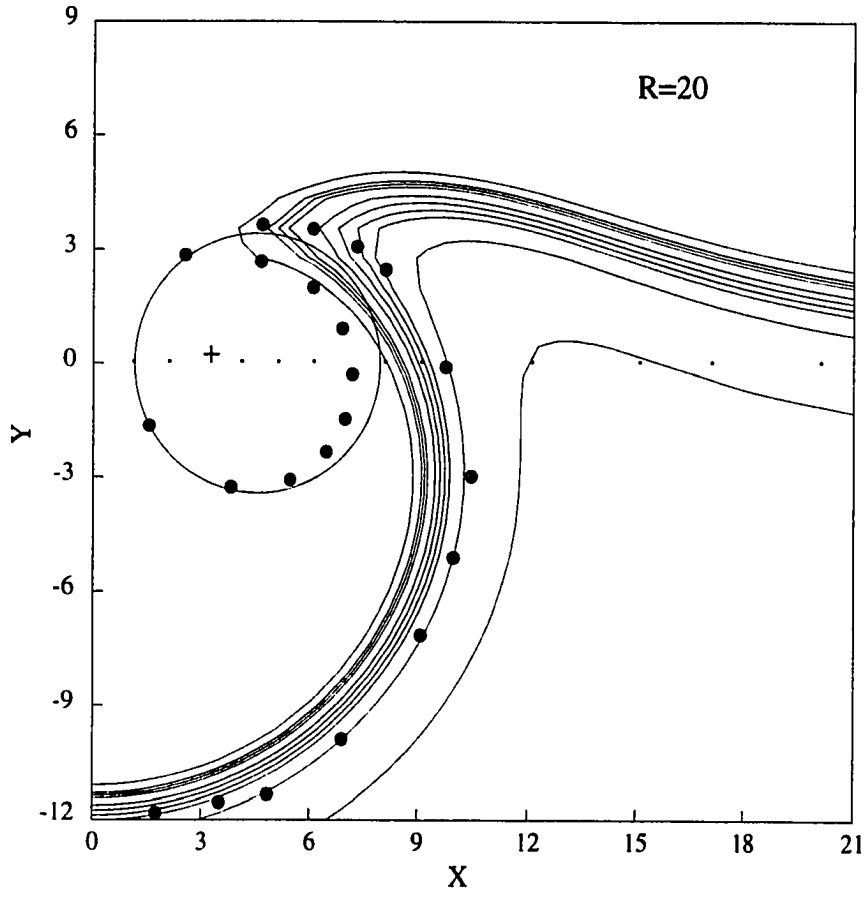

Figure 2.12: Ignition convection wavefront (•), F_1^I contours and recirculation circle.

Chapter 3

IGNITION AND STRUCTURE USING REDUCED MECHANISM COMBUSTION

3.1 Introduction

The previous analysis of the ignition in the field of a double vortex used a reduced combustion system representing a single step irreversible process of the form:

$$FUEL + OXYGEN \rightarrow PRODUCT + HEAT. \tag{3.1.1}$$

This is the simplest representation of reduced chemical combustion involving more than one species. In this chapter, the ignition and the post-ignition structure of mixing layers involving more complex models of reduced chemical systems is considered. The

first system was proposed by Birkan and Law [1] as:

$$OXYGEN + Radical_1 \rightarrow 2Radical_2 + HEAT, \tag{3.1.2}$$

$$FUEL + Radical_2 \rightarrow 2Radical_1 + HEAT \tag{3.1.3}$$

and

$$Radical_1 + Radical_2 + M \rightarrow 2Product + M + HEAT. \tag{3.1.4}$$

The second system, based on methane-air combustion (Peters [2]), is:

$$3H_2 + O_2 \rightleftharpoons 2H + 2H_2O \tag{3.1.5}$$

and

$$2H + M \rightleftharpoons H_2 + M. \tag{3.1.6}$$

The radicals represent additional elements or compounds necessary for the reaction scheme and M represents the composite of all inert compounds in the mixing gases. Equation (3.1.5) and equation (3.1.6) are both exothermic to the right and endothermic to the left. These two reduction schemes are analyzed in the mixing layer model of Jackson and Grosch [7]. The system is assumed to be at steady state. All component gases are assumed to have the same molecular weight and heat capacity.

3.2 Mixing Layer Equations

The physical geometry used by [7] envisions several gases initially flowing parallel and separated by a splitter plate. At $x = 0$ the plate ends and the gases begin to mix by convection and diffusion. The steady state nondimensional equations governing

the mixing layer in this analysis are a subset of (1.6.7) through (1.6.11) along with (1.6.12) and are given by:

$$\frac{\partial(\rho u)}{\partial x} + \frac{\partial(\rho v)}{\partial y} = 0, \tag{3.2.7}$$

$$\rho(u\frac{\partial u}{\partial x} + v\frac{\partial u}{\partial y}) = \frac{\partial}{\partial y}\left(\mu\frac{\partial u}{\partial y}\right), \tag{3.2.8}$$

$$\rho(u\frac{\partial T}{\partial x} + v\frac{\partial T}{\partial y}) = Pr_{\infty}^{-1}\frac{\partial}{\partial y}\left(\lambda\frac{\partial T}{\partial y}\right) + (\gamma_{\infty}-1)M_{\infty}^{2}\mu\left(\frac{\partial u}{\partial y}\right)^{2} + \Sigma_i\beta_i\Omega_i \tag{3.2.9}$$

$$\rho(u\frac{\partial F_j}{\partial x} + v\frac{\partial F_j}{\partial y}) = Sc_{\infty}^{-1}\frac{\partial}{\partial y}\left(\mu\frac{\partial F_j}{\partial y}\right) + \Sigma_i\nu^{ij}\Omega_i \tag{3.2.10}$$

and

$$\rho T = 1, \tag{3.2.11}$$

where

$$\Omega_i = \Sigma_j Da_{ij}F_iF_j\exp\left(-\frac{Ze_j}{T}\right) \tag{3.2.12}$$

and ν^{ij} is the stoichiometric number for the j^{th} species in the i^{th} reaction. Following the Howarth-Dorodnitsyn and similarity transformations, setting $Pr_{\infty} = Sc_{j_{\infty}} = 1$, and using the Chapman form for the viscosity, $\mu = T$, the governing equations become (see (1.7.19) through (1.7.22)):

$$f''' + 2ff'' = 0, \tag{3.2.13}$$

$$L(T) = (\gamma_{\infty}-1)M_{\infty}^{2}(f'')^{2} + \frac{4x}{\rho}\Sigma_i\beta_i\Omega_i, \tag{3.2.14}$$

and

$$L(F_j) = \frac{4x}{\rho}\Sigma_i \nu^{ij}\Omega_i \tag{3.2.15}$$

where

$$L(\ ) = 4xf'\frac{\partial(\ )}{\partial x} - (\ )'' - 2f(\ )', \tag{3.2.16}$$

with

$$(\ )' = \frac{\partial(\ )}{\partial \eta}.$$

3.3 Birkan and Law Reduction System

With the nondimensionalization performed using the dimensional values at infinity and adopting the notation

$$F_1 = FUEL, \quad F_2 = OXYGEN,$$

$$F_{R_2} = Radical_2 \quad \text{and} \quad F_{R_1} = Radical_1, \tag{3.3.17}$$

the initial and boundary conditions for the upper half-plane at the end of the splitter plate $x = 0$ and at $y \to \infty$ are

$$T = 1, \quad F_1 = 1, \quad F_2 = F_{R_2} = 0, \quad F_{R_1} = \beta_1 \quad \text{and} \quad u = 1. \tag{3.3.18}$$

Similarly, the initial and boundary conditions for the lower half-plane at the end of the splitter plate $x = 0$ and at $y \to -\infty$ are

$$T = \beta_T, \quad F_1 = 0, \quad F_2 = \phi, \ F_{R_2} = \beta_2, \quad F_{R_1} = 0 \quad \text{and} \quad u = \beta_u. \tag{3.3.19}$$

The reaction mechanism is given by

$$I: \quad F_2 + R_1 \to 2R_2 + Heat, \tag{3.3.20}$$

$$II: \quad F_1 + R_2 \rightarrow 2R_1 + Heat \tag{3.3.21}$$

and

$$III: \quad R_1 + R_2 + M \rightarrow 2P + M + Heat. \tag{3.3.22}$$

Following [1], the heat release parameters and the activation energies are set to

$$\beta_I = \beta_{II} = \beta_{III} = 1, \quad Ze_I = Ze_{II} = Ze \quad \text{and} \quad Ze_{III} = 0. \tag{3.3.23}$$

Under these assumptions, the reaction rates are

$$\Omega_I = Da_{F_2R_1} F_2 R_1 \exp(-Ze/T), \tag{3.3.24}$$

$$\Omega_{II} = Da_{F_1R_2} F_1 R_2 \exp(-Ze/T) \tag{3.3.25}$$

and

$$\Omega_{III} = Da_{R_1R_2} R_1 R_2. \tag{3.3.26}$$

The transformed equations take the form

$$f''' + 2ff'' = 0, \tag{3.3.27}$$

$$L(T) = (\gamma_\infty - 1)M_\infty^2 (f'')^2 + \frac{4x}{\rho}\Sigma_I \Omega_I, \tag{3.3.28}$$

$$L(F_1) = \frac{4x}{\rho}(-\Omega_I), \tag{3.3.29}$$

$$L(F_2) = \frac{4x}{\rho}(-\Omega_{II}), \tag{3.3.30}$$

$$L(R_1) = \frac{4x}{\rho}(2\Omega_{II} - \Omega_I - \Omega_{III}) \tag{3.3.31}$$

and

$$L(R_2) = \frac{4x}{\rho}(2\Omega_I - \Omega_{II} - \Omega_{III}). \tag{3.3.32}$$

To reduce the number of parameters, the Damkohler numbers are set as $Da_{F_1R_2} = Da_{F_2R_1} = Da_I$ and $Da_{R_1R_2}$ is chosen as

$$Da_{R_1R_2} = Da_{III} \exp(Ze). \tag{3.3.33}$$

3.3.1 Selection of Parameters

The following variables need to be selected for analysis of the above system:

$$\Phi, \quad \beta_1, \quad \beta_2, \quad Ze,$$
$$\beta_u, \quad \beta_T, \quad Da_I \quad \text{and} \quad Da_{III}. \tag{3.3.34}$$

Birkan and Law [1] solved their system at post-ignition equilibium and did not require setting initial conditions of R_1 and R_2. Here, the ignition is to be studied, and these initial conditions are important. In this system, no initial reaction is possible unless at least one of β_1 or β_2 is non-zero. The parameter choice is simplified by setting $\beta_2 = 0$ and varying β_1. In all the analysis that follows, Ze was chosen as 30 representing a moderate activation energy. Also set are the values $\beta_T = 1.0$ and $\beta_u = 0.5$

3.4 Methane-Air Reduction

The following system models combustion in a methane-air system as described by Peters [2]. The numerous reactions in the system are modeled by those representing the most heat production, the highest species concentration, and the slowest reaction rates. Eight reactions are chosen to be representative of the methane-air system:

$$\omega_1 : \quad H + O_2 \rightleftharpoons OH + O, \tag{3.4.35}$$

$$\omega_2 : \quad O + H_2 \rightleftharpoons OH + H, \tag{3.4.36}$$

$$\omega_3 : \quad H_2 + OH \rightleftharpoons H_2O + H, \tag{3.4.37}$$

$$\omega_4 : \quad OH + OH \rightleftharpoons O + H_2O, \tag{3.4.38}$$

$$\omega_5 : \quad H + O_2 + M \rightarrow HO_2 + M, \tag{3.4.39}$$

$$\omega_6 : \quad H + HO_2 \rightarrow 2OH, \tag{3.4.40}$$

$$\omega_7 : \quad H + HO_2 \rightarrow H_2 + O_2, \tag{3.4.41}$$

and

$$\omega_8 : \quad OH + HO_2 \rightarrow H_2O + O_2. \tag{3.4.42}$$

The species conservation equations are

$$L(H) = -\omega_1 + \omega_2 + \omega_3 - \omega_5 - \omega_6 - \omega_7, \tag{3.4.43}$$

$$L(OH) = \omega_1 + \omega_2 - \omega_3 - 2\omega_4 + 2\omega_6 - \omega_8 = 0, \tag{3.4.44}$$

$$L(O) = \omega_1 - \omega_2 + \omega_4 = 0, \tag{3.4.45}$$

$$L(H_2) = -\omega_2 - \omega_3 + \omega_4, \tag{3.4.46}$$

$$L(O_2) = -\omega_1 - \omega_5 + \omega_7 + \omega_8, \tag{3.4.47}$$

$$L(H_2O) = \omega_3 + \omega_4 + \omega_8 \tag{3.4.48}$$

and

$$L(HO_2) = \omega_5 - \omega_6 - \omega_7 - \omega_8 = 0. \tag{3.4.49}$$

An equilibrium assumption has been made for the reactants OH, O and HO_2 based on their faster reaction rates. The reaction rates are provided in [2] as the product

of the interacting species densities and the reaction k-factor given by

$$k_i = A_i T^{\beta_i} \exp(-E_i/RT). \tag{3.4.50}$$

As an example, the first reaction rate in the forward direction is given by

$$\omega_{1_f} = [H][O_2]k_{1_f}. \tag{3.4.51}$$

The equilibrium assumptions previously mentioned yield the equilibrium values

$$[HO_2]_{eq} = \frac{k_5[H][O_2][M]}{(k_6 + k_7)[H] + k_8[OH]}, \tag{3.4.52}$$

$$[OH]_{eq} = \frac{k_{3b}[H_2O][H]}{k_{3f}[H_2]} \tag{3.4.53}$$

and

$$[O]_{eq} = \frac{k_{4f}[OH][OH]}{k_{3f}[H_2]}. \tag{3.4.54}$$

The species conservation equations are reduced to

$$L(H) = 2(\omega_1 + \omega_6) - 2\omega_5 - \omega_7, \tag{3.4.55}$$

$$L(H_2) = -3(\omega_1 + \omega_6) + \omega_5, \tag{3.4.56}$$

$$L(O_2) = -(\omega_1 + \omega_6) \tag{3.4.57}$$

and

$$L(H_2O) = 2(\omega_3 + \omega_6). \tag{3.4.58}$$

The chemical system equivalent to the above is

$$I: \quad 3H_2 + O_2 \rightleftharpoons 2H + 2H_2O \tag{3.4.59}$$

and

$$II: \quad 2H + M \rightleftharpoons H_2 + M. \tag{3.4.60}$$

The global reaction rates are given by

$$\omega_I = \omega_1 + \omega_6 \tag{3.4.61}$$

and

$$\omega_{II} = \omega_5. \tag{3.4.62}$$

The remaining governing equations for this system are

$$f''' + 2ff'' = 0 \tag{3.4.63}$$

and

$$L(T) = (\gamma_\infty - 1)M_\infty^2(f'')^2 + \frac{4x}{\rho}(\beta_I\omega_I + \beta_{II}\omega_{II}). \tag{3.4.64}$$

The values of β_I and β_{II} are calculated from reference tables of enthalpy (McBride [12]) based on formation of the compounds from the assigned reference elements.

3.4.1 Selection of Parameters

In the Birkan and Law system no initial reaction is possible if both R_1 and R_2 are not present for $x < 0$. A similiar conclusion is found here by analyzing equations (3.4.35) through (3.4.42). If only H_2 and O_2 are present for the initial condition $x < 0$, then the reactions will not start. Here, the initial condition will provide for some loading of H on the same side of the splitter plate as is H_2. The minimum value of H to be expected is calculated by assuming equilibrium disassociation of H_2 according to

$$H_2 + M \rightleftharpoons 2H + M. \tag{3.4.65}$$

This gives an initial H concentration of $O(10^{-11})$. Calculations were made using this minimum value and several other values of initial H loading .

3.5 Numerical Techniques

Equation (3.4.63) for the streamfunction f is independent of the remaining equations and is solved using the boundary value problem solver COLSYS. The remaining equations are formed into an implicit nonlinear system of equations using the Crank-Nicholson finite-differencing scheme. The system is in the form

$$A\vec{h}(x) = \vec{b}(x) \tag{3.5.66}$$

and is marched in the x-direction from $x = 0$ past the ignition point to a post-ignition steady state. The matrix A is inverted using the Thomas algorithm. The x dependence of the inhomogenous term $\vec{b}(x)$ is handled by an iteration process for each $\triangle x$ step of the form:

$$A\vec{h}([x + \triangle x]_1) = \vec{b}(x) \tag{3.5.67}$$

and

$$A\vec{h}([x + \triangle x]_{i+1}) = \vec{b}([x + \triangle x]_i). \tag{3.5.68}$$

This iteration technique is more complicated for the methane-air system which requires calculation of equilbrium values for O, OH and HO_2 at each iteration and each new value of x.

3.6 Results

3.6.1 Ignition Distances

The Birkan-Law reduction system and the reduced methane-air system are analyzed to determine the point of ignition x_{ig} as a function of β_1 or $H_{initial}$. These parameters are varied over several orders of magnitude. The ignition point is defined as the point when the maximum temperature reaches 90% of its post-ignition flame temperature. For the Birkan-Law system with Da_1=Da_2=50, Da_3=1000, $\beta_T = 1.0$ and $\phi = 0.5$ an almost linear relationship of the ignition distance as a function of the $\log(\beta_1)$ is found (see Figure 3.1). For the methane-air system with $\beta_T = 1.0$ and $\phi = 0.5$, Figure 3.2 shows a similar near linear relationship of the ignition distance as a function of the $\log(H_{initial})$. A comparison of the ignition distances of Figure 3.1 to those of Figure 3.2 reveals a difference by a factor of 10 to 20. This can be attributed to the different reaction mechanisms, the heat release factors and the form of the Arrhenius reaction as determined by the respective Damkohler numbers and activation energies.

3.6.2 Component Densities at Ignition

Since the initial loading of the radicals effects the ignition distance, the values of the radical mass fraction at the ignition point should be of interest. Figure 3.3 shows the concentration of radicals R_1 and R_2 at the time of ignition for $\beta_1 = 10^{-5}$, $\beta_1 = 10^{-4}$ and $\beta_1 = 10^{-3}$. The difference in magnitude between R_1 and R_2 at the interface is due to the fuel-oxidizer difference represented by $\phi = 0.5$. Figure 3.4 shows the nondimensional concentration of H_2O and H for methane-air system with initial H

loading varying from 10^{-11} to 10^{-4}. Although the initial loading varies over several orders of magnitude, the mass fraction profiles at ignition are nearly identical, thus it appears from Figures 3.3 and 3.4 that ignition is delayed (*i.e.* x_{ig} varies) until the radical concentration at the interface reaches some required level.

3.6.3 Flame Temperature

The temperature of the post-ignition flame is independent of the initial radical loading. Figure 3.5 shows the maximum temperature as a function of x for the methane-air reduction system for two different $H_{initial}$: 10^{-11} and 10^{-4}. This Figure shows that ignition is delayed for $H_{initial} = 10^{-11}$, but the post-ignition flame temperature is the same in both cases.

3.6.4 Flame Structure

Figures 3.6 and 3.7 show the mass fraction of the component gases, the temperature and the regularity factor (see Chapter 5) of the post-ignition, steady flame as a function of η for $H_{initial} = 10^{-11}$ and $\phi = 0.5$ and 1.0 respectively. With the larger concentration of H_2, the flame temperature is higher as are the concentrations of all of the intermediate reactants and products. Figure 3.8 shows the maximum value of temperature, H_2O and H for the methane-air system as a function of x with $H_{initial} = 10^{-11}$ and $\phi = 0.5$. The build up of H_2O and H to ignition is evident as is the post-ignition approach to an equilibrium value.

3.7 Conclusion

Ignition and post-ignition of a non-premixed flame in a laminar mixing layer has been studied. Two reduced chemical reaction systems were used. Both reduction systems gave similiar results as to the effects of the input parameters on the ignition distances and the ignition structure. In each case some initial loading of at least one of the radical components was required. The ignition distances varied inversely to the logarithm of the initial loading. The concentration of the radicals and the post-ignition flame temperature are relatively unaffected by the initial radical loading.

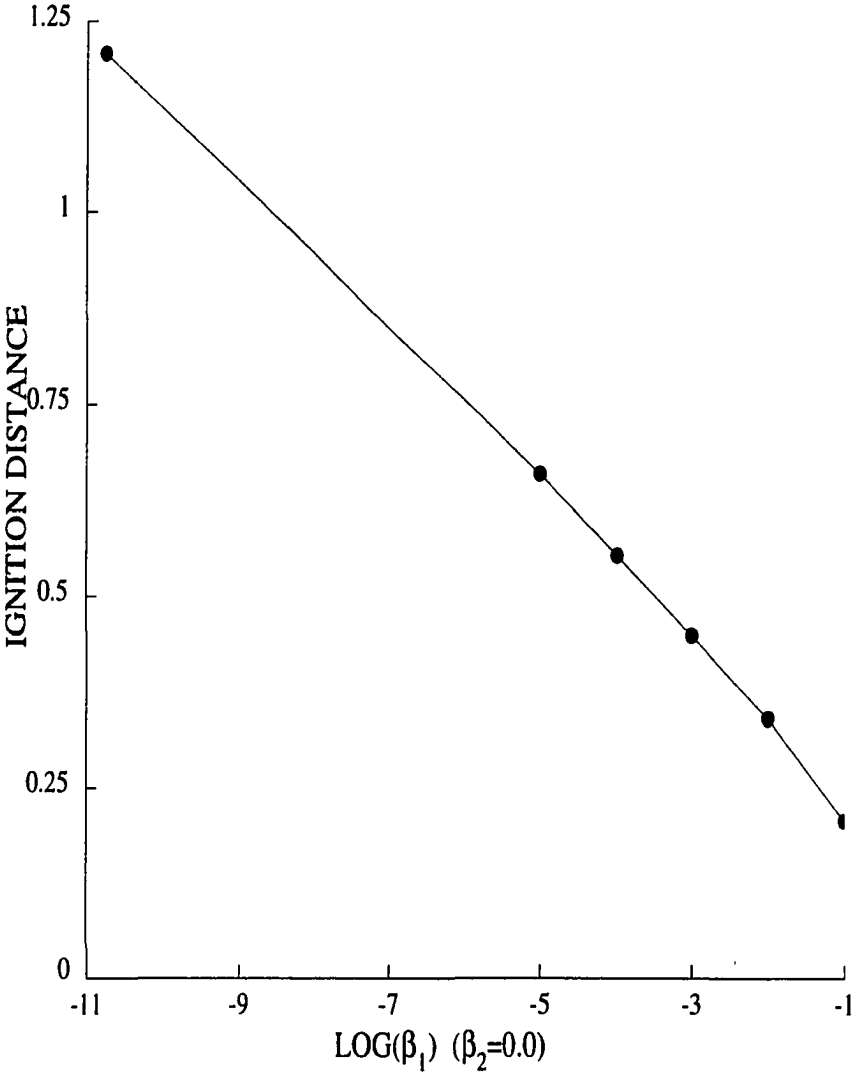

Figure 3.1: Nondimensional ignition distance as a function of β_1 loading using the Birkan-Law reduction with $Da_1=Da_2=50$, $Da_3=1000$, and $\phi = 0.5$.

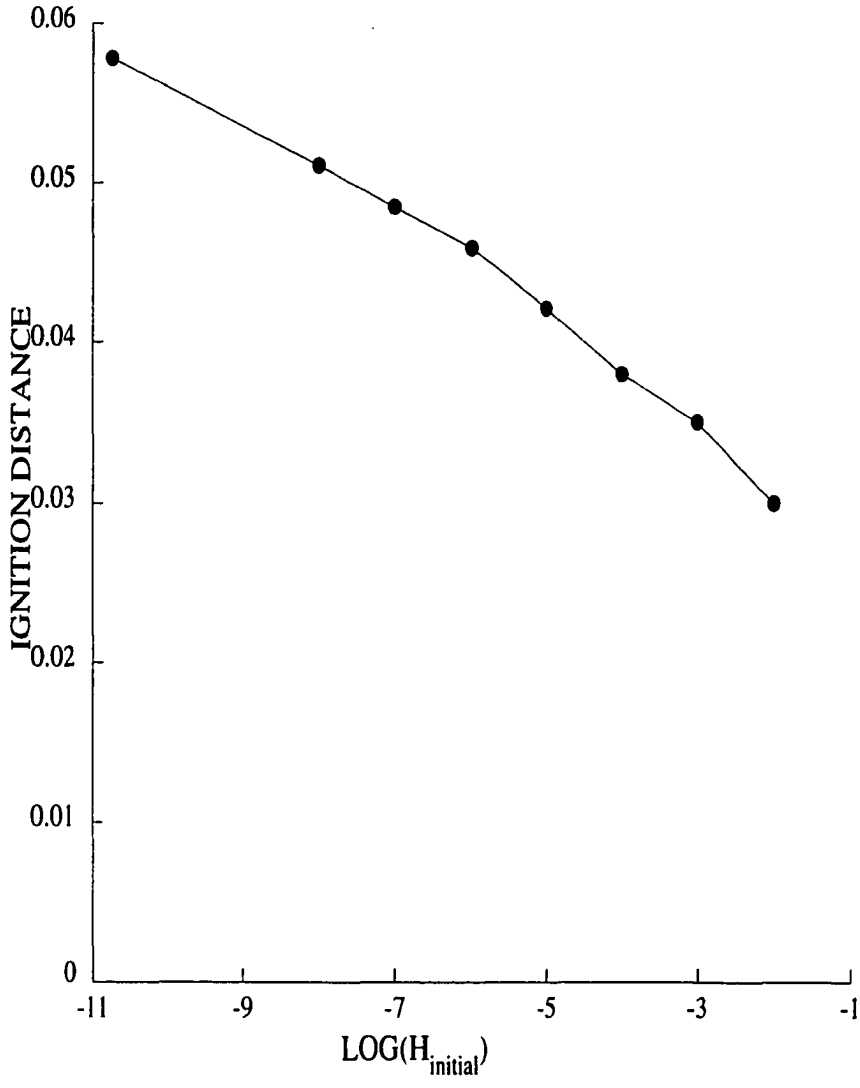

Figure 3.2: Nondimensional ignition distance as a function of $H_{initial}$ loading using the methane-air reduction with $\phi = 0.5$.

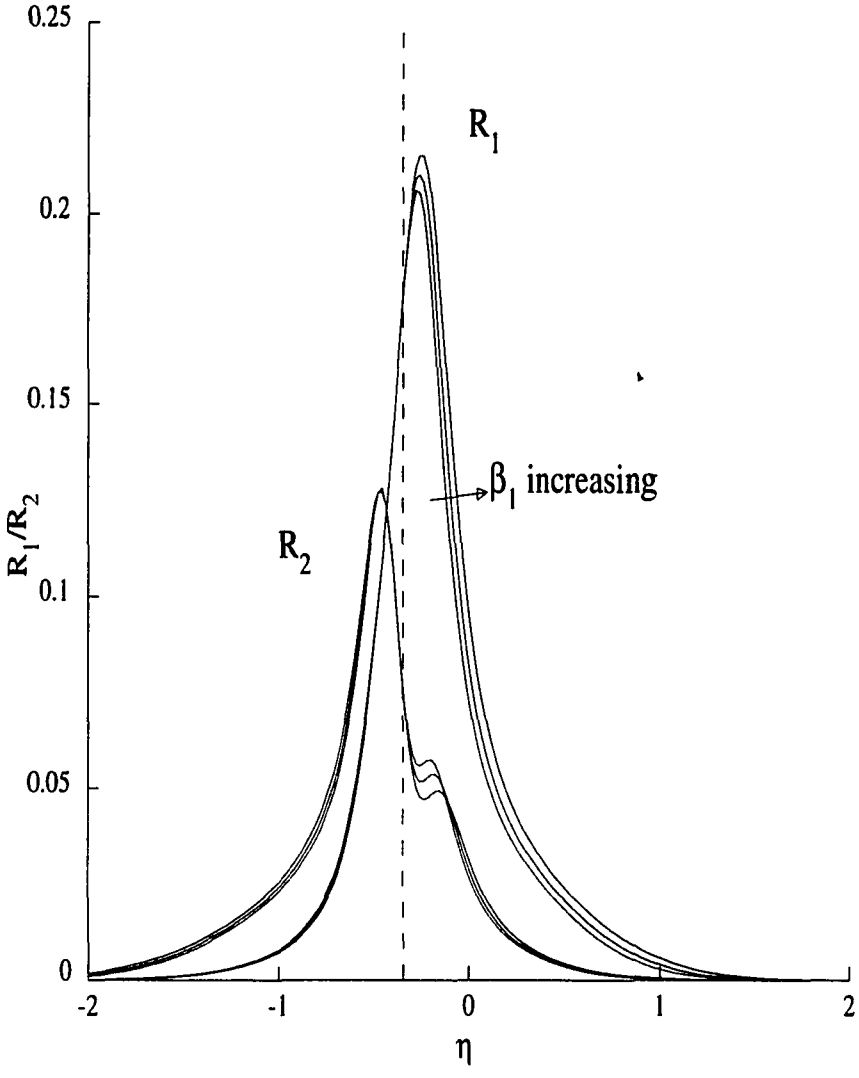

Figure 3.3: Nondimensional radical concentrations for different $H_{initial}$ loading using the Birkan-Law reduction.

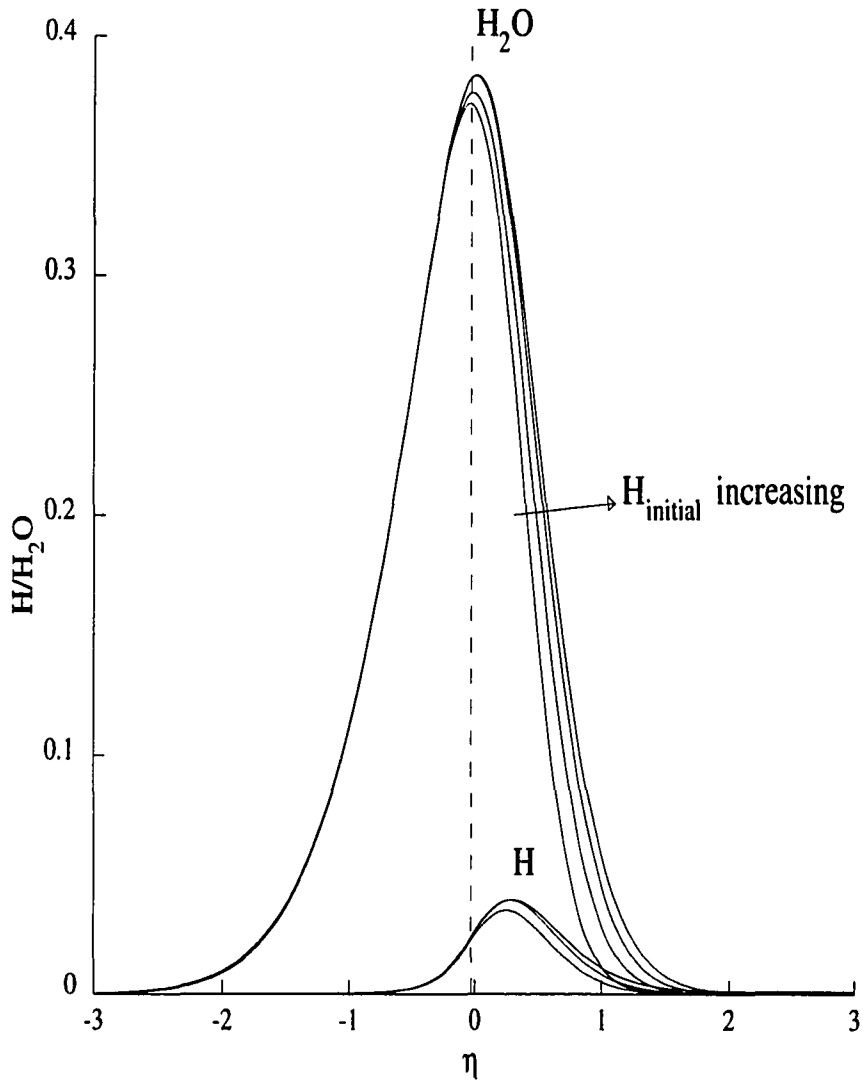

Figure 3.4: Nondimensional H and H_2O concentrations for different $H_{initial}$ loading using the methane-air reduction.

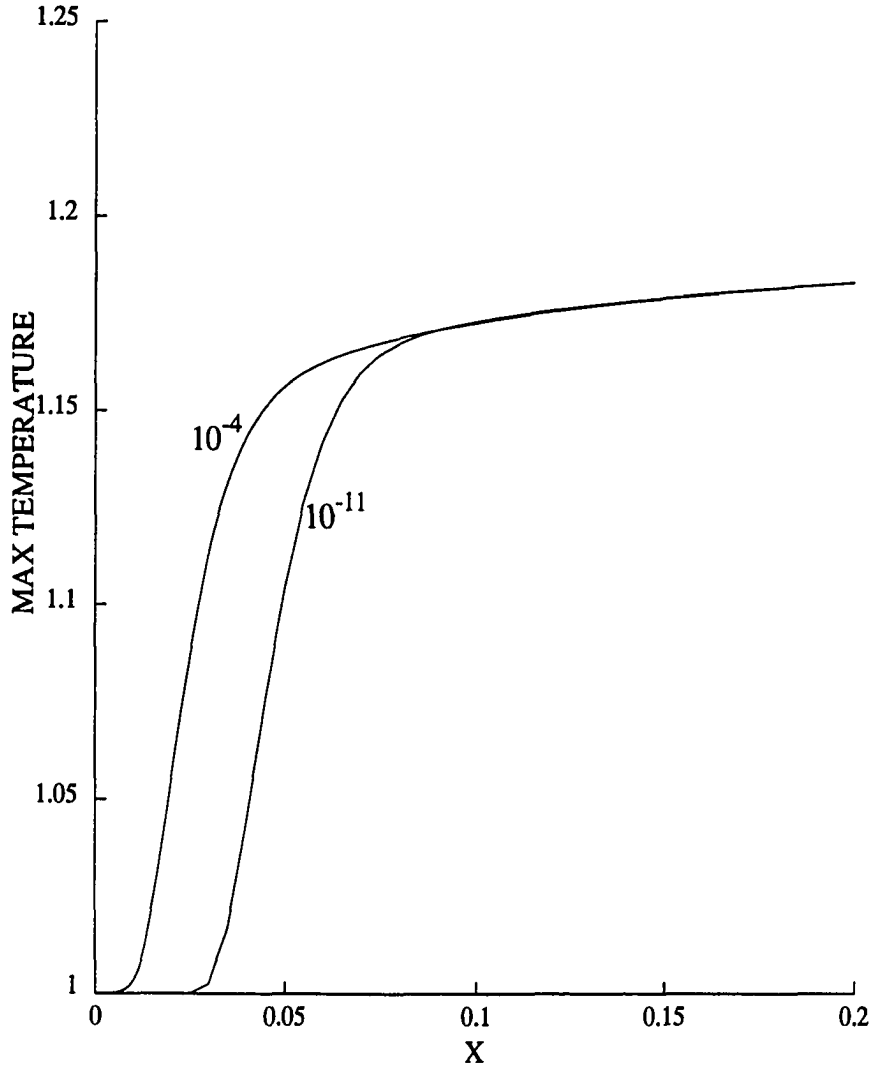

Figure 3.5: Maximum temperature vs x for methane-air reduction with $\phi = 0.5$ and $H_{initial} = 10^{-11}$ and $H_{initial} = 10^{-4}$.

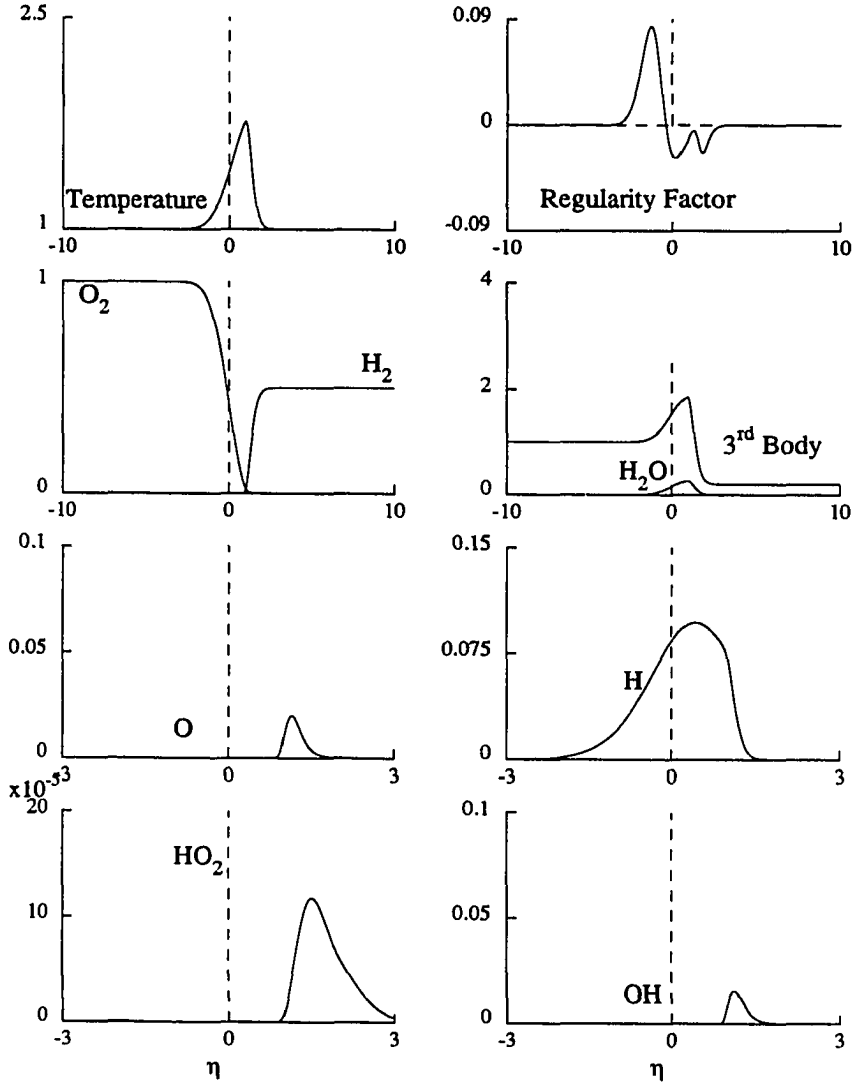

Figure 3.6: Post-ignition flame structure for methane-air reduction with $\phi = 0.5$ and $H_{initial} = 10^{-11}$.

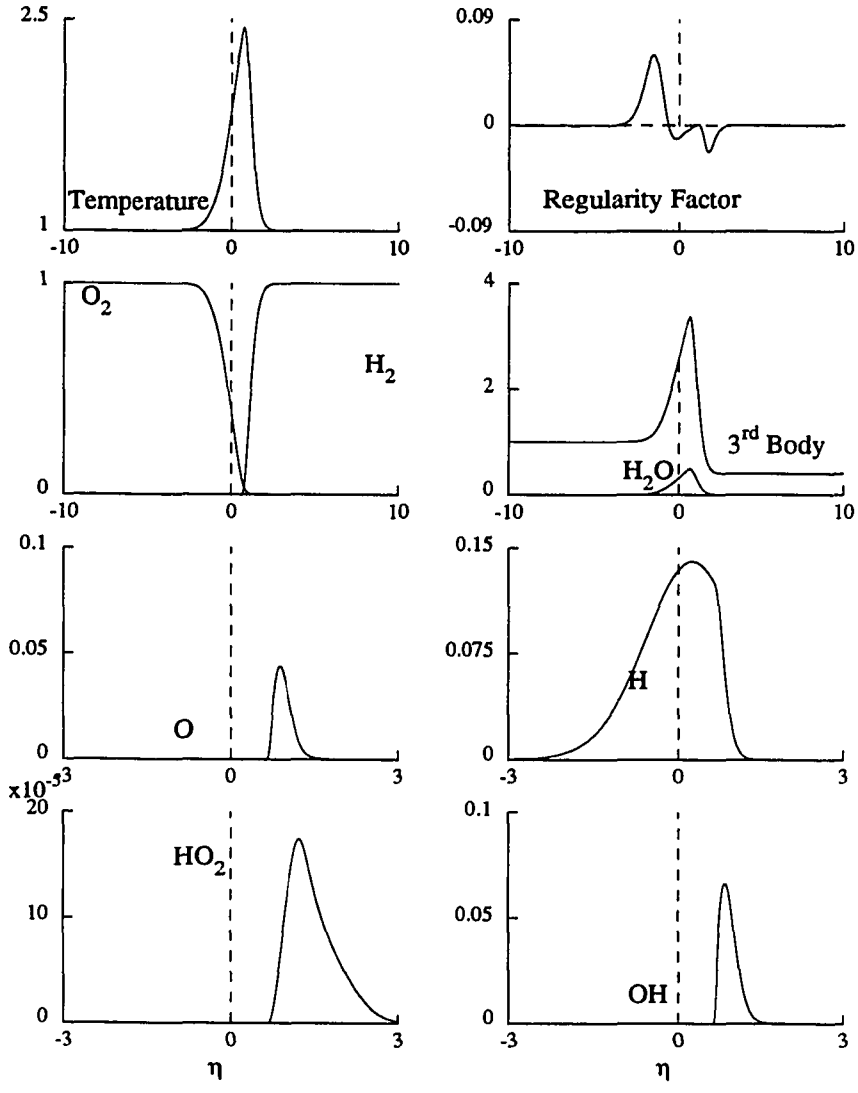

Figure 3.7: Post-ignition flame structure for methane-air reduction with $\phi = 1.0$ and $H_{initial} = 10^{-11}$.

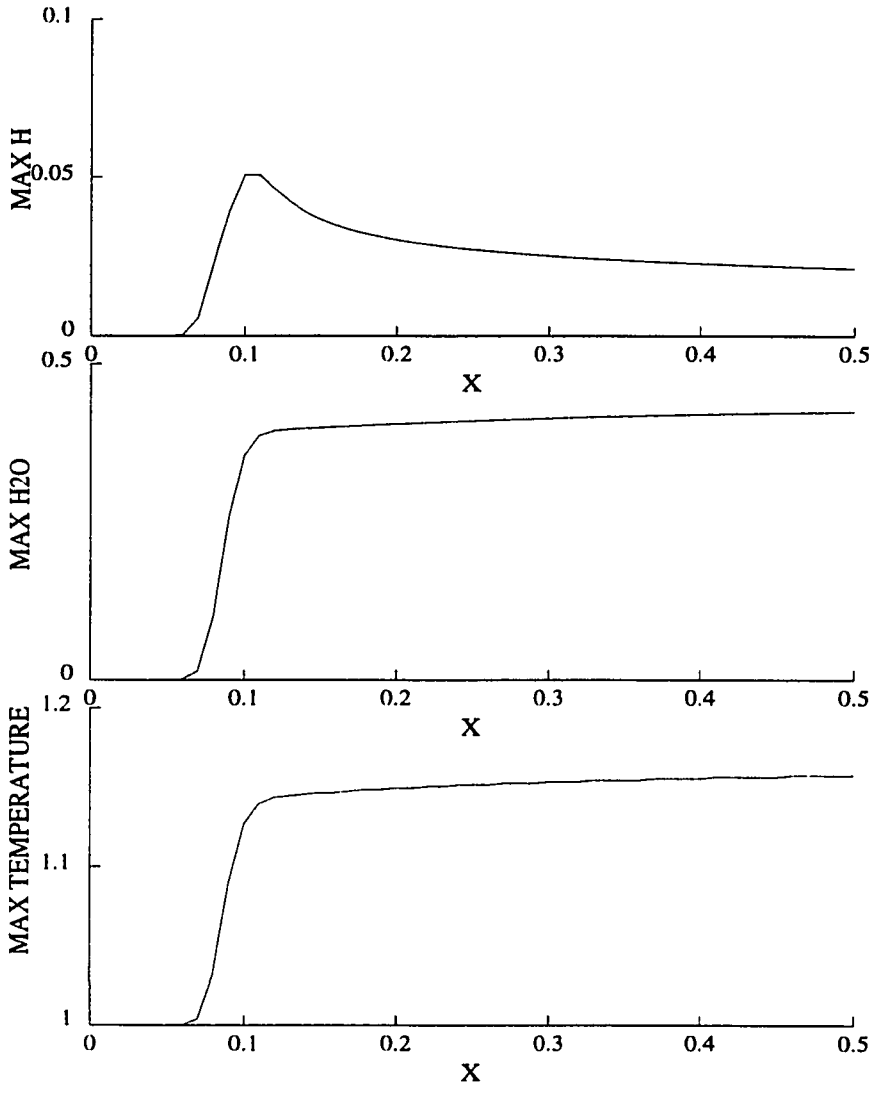

Figure 3.8: Maximum temperature, H_2O and H concentrations vs x for methane-air reduction with $\phi = 0.5$ and $H_{initial} = 10^{-11}$.

Chapter 4

THE STRUCTURE OF A COMPRESSIBLE MIXING LAYER IN A BINARY GAS

4.1 Introduction

As previously mentioned and practiced in Chapters Two and Three, it is common in mixing layer studies to assign constant and nominal values to the parameters μ, λ, C_p, D_i, Pr and Sc or to calculate values according to simplified models. Additionally, it is common to assign equal molecular weights to the gases considered, thus simplifying the problem further. Here, the mixing of two gases across a laminar mixing layer will be studied using values for the transport properties calculated from detailed models or tabulated data and using the real molecular weights. Thus, this is an accurate representation of a mixing layer using a combination of real gases. The geometry

is identical to the reduced chemistry combustion problem of the previous chapter. However, the gases will be assumed non-reacting. The mixing will be limited to two gases, but could of course be extended to include more. The gases included in this study are hydrogen (H_2), helium (He), neon (Ne), nitrogen (N_2), oxygen (O_2) and argon (Ar). This choice of gases was not arbitrary. Papamoschou and Roshko [13] and Hall, Dimotakis and Rosemann [14] used binary combinations of He, N_2 and Ar in their experiments. In addition, hydrogen is the proposed fuel for scramjet engines.

4.2 Governing Equations

The nondimensional equations are given by

$$(\rho\mu f'')' + 2ff'' = 0, \tag{4.2.1}$$

$$(\rho\lambda T')' + 2Pr_\infty C_P f T' + (\gamma_\infty - 1)M_\infty^2 Pr_\infty \rho\mu f''^2 + Pr_\infty Sc_\infty^{-1}\rho^2 D_{12}T'\sum_1^2 C_{P,i}F_i' = 0, \tag{4.2.2}$$

$$(\rho^2 D_{12}F_1')' + 2Sc_\infty f F_1' = 0, \tag{4.2.3}$$

$$1 = F_1 + F_2, \tag{4.2.4}$$

$$1 = \rho T(WF_1 + F_2), \tag{4.2.5}$$

and

$$C_P = \sum_1^2 C_{P,i}F_i. \tag{4.2.6}$$

The equations were nondimensionalized by the freestream quantities ρ_∞, T_∞, u_∞, $P_\infty = \rho_\infty R^o T_\infty/W_2$, μ_∞, λ_∞, $D_{12,\infty}$, $C_{P,\infty}$ for the density, temperature, velocities, pressure, viscosity, thermal conductivity, binary diffusion coefficient and specific heat,

respectively. Primes denote differentiation with respect to the similarity variable η. The constants appearing above are the Schmidt number $Sc_\infty = \mu_\infty/\rho_\infty D_{12,\infty}$, the Prandtl number $Pr_\infty = \mu_\infty C_{P,\infty}/\lambda_\infty$, the Mach number $M_\infty = u_\infty/a_\infty$, the molecular weight W_i of species F_i with $W = W_2/W_1$ being their ratio, and the ratio of specific heats γ_∞. The speed of sound is $a_\infty^2 = (\gamma_\infty - 1)C_{P,\infty}T_\infty$. A fixed value of $T_\infty = 300^\circ K$ is used for this study.

The appropriate boundary conditions are

$$T = f' = F_2 = 1 \quad \text{and} \quad F_1 = 0 \qquad as \;\; \eta \to \infty, \tag{4.2.7}$$

and

$$T = \beta_T, \quad f' = \beta_U, \quad F_1 = 1 \quad \text{and} \quad F_2 = 0 \qquad as \;\; \eta \to -\infty, \tag{4.2.8}$$

with $\beta_U = \frac{U^*_{-\infty}}{U^*_\infty} \in [0,1)$ and $\beta_T \frac{T^*_{-\infty}}{T^*_\infty} > 0$ being the velocity and the temperature ratios, respectively. For the momentum equation, the third boundary condition $f(0) = 0$ is imposed to fix the streamline along the streamwise axis. If β_T is less than one, the gas in the slow freestream is relatively cold compared with that in the fast freestream, and if β_T is greater than one it is relatively hot. There are two cases depending on the magnitude of W:

- $\underline{W > 1}$: heavier gas resides in the fast freestream at $\eta = \infty$ and the lighter gas in the slow freestream at $\eta = -\infty$; or
- $\underline{W < 1}$: lighter gas resides in the fast freestream at $\eta = \infty$ and the heavier gas in the slow freestream at $\eta = -\infty$.

For the inert gases Ar and He (typical gases used in experiments), we see that W can vary between 0.1 for the Ar-He case, and 9.9 for the He-Ar case. The convention is

used that the first gas listed corresponds to F_1 which resides in the slow freestream at $\eta = -\infty$, while the second gas listed corresponds to F_2 which resides in the fast freestream at $\eta = \infty$; e.g., the case *Ar-He* implies that the gas in the slow freestream is argon, while the gas in the fast freestream is helium. The ratio of molecular weights, W, for the different gases considered in this study is given in Table 1.

4.3 Calculation of Transport and Thermal Properties

The following transport and thermal properties are variables of the dynamic system and are thus dependent on the values of T and F: thermal conductivity(λ), coefficient of viscosity(μ), binary diffusion coefficient(D_{12}) and thermal heat capacity(C_p). The values of each must be calculated at each new value of η as equations (4.2.1) to (4.2.6) are solved from $-\infty$ to ∞. The methods used to determine each follows.

4.3.1 Heat Capacity

The heat capacities of the individual gases as a function of temperature is obtained in tabulated form from reference tables (McBride [12]) and stored. Linear interpolation is used to obtain the specific heat at any temperature. All specific heat values are nondimensionalized by the specific heat of the individual gas at $\eta = \infty$ and $T^* = T^*_\infty = 300°\text{K}$. The nondimensional mixture C_p is calculated by :

$$C_p = F_1 C_{p_1} + F_2 C_{p_2}. \tag{4.3.9}$$

4.3.2 Coefficient of Viscosity

Viscosities are calculated using cross section and collision integral theory (Anderson [8] and Maitland [15]). The theory provides for calculation of the individual gas viscosity coefficients and the calculation of a mixture viscosity as a function of temperature and the concentrations, F_1 and F_2. This again calls for tabular storage and interpolation. The collision and integral theory provides forms for calculating viscosities for monatomic and polyatomic gases. The polyatomic form is not used because of its complexity. However, numerous spot checks were run comparing the individual and mixture viscosities calculated using the monatomic form against coefficients of viscosity found in Touloudian et al [16]. Satisfactory agreement was obtained in all cases for monatomic and polyatomic gases, so the monatomic form of the viscosity is used. The viscosity values are nondimensionalized by the value of the viscosity of the individual gas at at $\eta = \infty$ and $T^* = T^*_\infty = 300°\text{K}$.

4.3.3 Thermal Conductivity

An attempt was made to use the monatomic forms of the cross section and collision integral theory to calculate thermal conductivities for both monatomic and polyatomic gases. Thermal conductivities for polyatomic gases (N_2, H_2 and N_2) calculated this way compared poorly against reference tables (Touloudian et al [17]. This lead to using tabular data [17] to calculate the thermal conductivity for the individual gases. The mixture conductivity is calculated using the method of Mason and Saxena recommended by [17]. Since this theory provides one form for monatomic gases and one

for polyatomic gases, the polyatomic form is used if at least one of the two gases is polyatomic. The thermal conductivity values are nondimensionalized by the value of the thermal conductivity of the individual gas at $\eta = \infty$ and $T^* = T^*_\infty = 300°\text{K}$.

4.3.4 Binary Diffusion Coefficient

The scattering cross section and collision integral theory is used to calculate D_{12}. The monatomic form was used for all cases. The use of the monatomic form to calculate D_{12} for mixtures involving polyatomic gases is justified since satisfactory checks were made against the experimental data of Bzowski [18] and Hirschfelder [19]. Additionally, Hirschfelder [19] states that the agreement between experimental data and the monatomic theory predictions is generally quite satisfactory for both monatomic and polyatomic gases.

4.4 Numerical Techniques

The system of equations is solved by a "shooting" method. The system requires four shooting parameters related to the asymptotic values in the freestream.

4.4.1 Asymptotic Analysis of Equations

In the limit as $\eta \to -\infty$ the transport properties can be consider constant and equations (1.7.19) take the form:

$$\mu\rho f''' + 2ff'' = 0, \tag{4.4.10}$$

$$\rho^2 D_{12_\infty} F_i'' + 2Sc_\infty f F_i' = 0 \tag{4.4.11}$$

and

$$\lambda\rho T'' + Pr_\infty M_\infty^2(\gamma-1)\rho\mu(f'')^2 + \frac{Pr_\infty}{Sc_\infty}\rho^2 D_{12_\infty}(C_{p_1}F_1' + C_{p_2}F_2')T' + 2C_p Pr_\infty f T' = 0. \tag{4.4.12}$$

The system is simplified by setting $F = F_1 = 1 - F_2$. From Kennedy and Gatski [20], the following approximations are made:

$$f \approx d_1 + \beta_U \eta + \int_{-\infty}^{-\eta} Q_U(\eta^*)d\eta^*, \tag{4.4.13}$$

$$f_\eta \approx \beta_U + Q_U(\eta), \qquad f_{\eta\eta} \approx Q_U'(\eta), \tag{4.4.14}$$

$$F \approx 1 + Q_F(\eta), \qquad F' \approx Q_F'(\eta), \tag{4.4.15}$$

$$T \approx \beta_T + Q_T(\eta) \quad \text{and} \qquad T' \approx Q_T'(\eta). \tag{4.4.16}$$

Upon substitution, the leading order equations take the form ($f' = U$):

$$Q_{(\,)}'' + 2\alpha_{(\,)}^2\left(\frac{d_1}{\beta_U} + \eta\right)Q_{(\,)}' = 0, \tag{4.4.17}$$

where ( ) stands for U, T or F. The α's are defined as

$$\alpha_U = \left(\frac{\beta_U}{\beta_\mu\beta_\rho}\right)^{\frac{1}{2}}, \qquad \alpha_F = \left(\frac{Sc_\infty\beta_U}{\beta_\rho^2\beta_D}\right)^{\frac{1}{2}} \quad \text{and} \quad \alpha_T = \left(\frac{\beta_{C_P}Pr_\infty\beta_U}{\beta_\lambda\beta_\rho}\right)^{\frac{1}{2}}, \tag{4.4.18}$$

where

$$\beta_{C_P} = \frac{C_{P_{-\infty}}^*}{C_{P_\infty}^*}, \qquad \beta_D = \frac{D_{12_{-\infty}}^*}{D_{12_\infty}^*}, \qquad \beta_\rho = \frac{\rho_{-\infty}^*}{\rho_\infty^*} \quad \text{and} \quad \beta_\lambda = \frac{\lambda_{-\infty}^*}{\lambda_\infty^*}. \tag{4.4.19}$$

As $\eta \to -\infty$, $Q_{(\,)} \to 0$ for all three cases, and the solution of equation 4.4.17 is asymptotic to

$$Q_{(\,)} = \frac{2\alpha c_{(\,)} exp(-\alpha_{(\,)}^2(\frac{d_1}{\beta_U} + \eta)^2)}{(\frac{d_1}{\beta_U} + \eta)} \tag{4.4.20}$$

where $c_{(\,)}$ is the remaining constant of integration.

4.4.2 Shooting Scheme

With the above asymptotic equations and the boundary conditions of the original system, values for f, f', f'', f''', F, F', T and T' are known at $\eta = -\infty$ in terms of the four unknown constants (*i.e.* the shooting parameters) d_1, c_U, c_T and c_F. An iterative method involving a four step Runga-Kutta initial value problem solver is used to integrate the system from $\eta = -\infty$ to $\eta = \infty$. The shooting parameters are chosen to satisfy the appropriate conditions at the interface and at the upper freestream. The system is extremely stiff and requires a stepped convergence. The parameter d_1 is used to satisfy $f(0) = 0$, c_U and c_T are used to step U and T toward an interim boundary condition until the changes in each are less than some chosen tolerance. Holding the values of d_1, c_U and c_T constant, c_F is used to step F toward an interim boundary condition. This stepping of F may unbalance the system, causing many more cycles to be necessary to re-satisfy the conditions on f, f' and T before the next cycle on F is attempted. The iterations are continued until the total relative change in the shooting parameters with the full boundary conditions is less than a selected tolerance (10^{-4}).

4.5 Results

The system of equations (4.2.1) through (4.2.6) is solved for all 30 possible combinations of the six gases. The cases of a gas mixing with itself is not considered. The values of $M_\infty = 0$, $\beta_T = 1.5$ and $\beta_U = 0.5$ are maintained throughout. The structure of the mixing layer parameters are shown in Figures (4.1) through (4.6). These

Figures present the following nondimensional parameters as a function of η: Lewis number(Le), heat capacity (C_p), density (ρ), Prandtl number (Pr), flow velocity parallel to the x axis (u), temperature and mass fractions (F_1 and F_2) for the two gases involved. Only a few of the thirty graphs showing the mixture structure are presented in this chapter, the rest are shown in Appendices A and B.

4.5.1 Effect on Lewis Number

The Lewis number is defined as Sc/Pr. As mentioned above it is common to assume a constant value for the Lewis number. Figure (4.1) is an O_2-H_2 mixture while Figure (4.2) is an H_2-O_2 mixture. The value of W for these systems is respectively 0.063 and 15.873. In both figures the Lewis number has different values at $\pm\infty$ and varies through the mixing layer, thus indicating that it is not correct to assume a constant value of the Lewis number.

Figure (4.3) represents an He-H_2 mixture and Figure (4.4) is for the Ar-Ne mixture. These two cases have W values of 0.504 and 0.505. While the weight ratio is nearly the same, the Lewis number variation is much larger for the Ar-Ne case. This shows that the weight ratio is not the sole factor effecting Lewis number. The Lewis number is determined by other thermal properties which differ between the Ar-Ne case and the He-H_2 case. As an example, Figures (4.3) and (4.4) show the difference in the nondimensional heat capacity between the two cases.

For this study, the W values closest to 1.0 are for O_2-N_2 and N_2-O_2 with W values of 0.876 and 1.142. These mixing cases, shown in Figures (4.5) and (4.6), have a near constant value of Lewis number through the mixing layer.

4.5.2 Effect on Prandlt Number

The Prandlt number also varies through the mixing layer but in a different way than the Lewis number. In Figures (4.1) and (4.2), the Prandlt number at $\pm\infty$ are very nearly equal, while Pr varies signifigantly through the mixing layer. For the near equal W value cases, Figures (4.3) and (4.4) show a near constant value of Pr. For the W nearest to 1.0 cases of Figures (4.5) and (4.6), the value of Pr is nearly constant.

4.5.3 Effect on Density

The density ρ should be expected to vary with W since the density is given by:

$$\rho = (T[WF_1 + F_2])^{-1} \tag{4.5.21}$$

Clearly, mass fractions and temperature are dependent on the transport properties; therefore, in a secondary way, so is density. This is demonstrated most readily by Figures (4.2) through (4.6) which show cases of density being nearly constant to cases of density changing by a factor of two. In Figures (4.5) and (4.6), W is nearly one, but the density profiles of the two cases are very different.

4.5.4 Effect of Heat Capacity

The heat capacity H_2, N_2 and O_2 are temperature dependent. The heat capacity of monatomic gases in this study (He, Ne and Ar) does not depend on temperature. The mixture heat capacity is determined by

$$C_p = C_{p_1}F_1 + C_{p_2}F_2 \tag{4.5.22}$$

Figures (4.2) through (4.6) show the mixture heat capacities varying sharply through the mixing layer.

4.6 Conclusion

The characteristics of the mixing of two real gases in a laminar mixing layer were investigated using theoretical and tabulated data to calculate the values of thermal conductivity(λ), coefficient of viscosity(μ), binary diffusion coefficient(D_{12}) and thermal heat capacity(C_p). The true molecular weights were used. The gases considered in the study were hydrogen (H_2), helium (He), neon (Ne), nitrogen (N_2), oxygen (O_2) and argon (Ar). Since the freestream velocity and temperature were different at $-\infty$ and ∞, and self mixing was not considered, 30 different mixing combinations are included in the study.

In general, Le, Pr and C_p were not constants. The ratio of the gas molecular weights alone is not a gauge of the variation of these parameters. The combinations of N_2 - O_2 and O_2-N_2 with the weight ratio nearest 1.0 did show a near constant Prandtl and Lewis numbers. However, the combinations of He-H_2 and Ar-Ne with weight ratios of 0.504 and 0.505 respectively had very different profiles for the Prandtl and Lewis numbers in the mixing layer because of the different values of thermal parameters of the individual gases mixed. The Prandtl and Lewis numbers could vary across the mixing layer by factors of approximately 3 and 7, respectively.

Consequently, setting Pr and Le to constant values for the laminar problem is a poor approximation except in a few cases. Assuming equal molecular weights for the two

gases to be mixed will also provide a poor model for the mixing layer.

Table 4.1: The ratio of molecular weights W, defined as the molecular weight of the gas at $\eta = \infty$ divided by the molecular weight of the gas at $\eta = -\infty$, for the different gases considered in this study. The top row corresponds to the gases in the freestream at $\eta = \infty$, while the first column corresponds to the gases in the freestream at $\eta = -\infty$.

	H_2	He	Ne	N_2	O_2	Ar
H_2	1.000	1.986	10.011	13.897	15.873	19.813
He	0.504	1.000	5.042	6.999	7.994	9.979
Ne	0.100	0.198	1.000	1.388	1.585	1.979
N_2	0.072	0.143	0.720	1.000	1.142	1.426
O_2	0.063	0.125	0.631	0.876	1.000	1.248
Ar	0.050	0.100	0.505	0.701	0.801	1.000

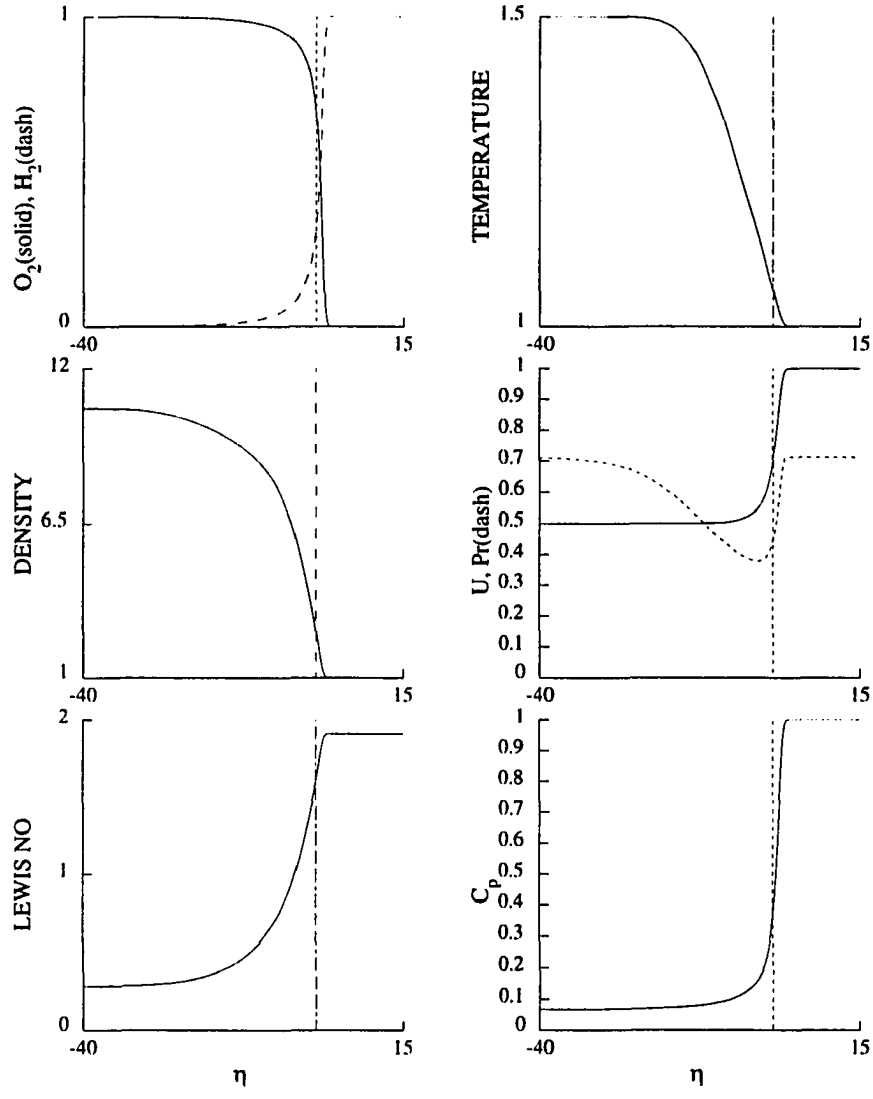

Figure 4.1: Mixing layer structure for O_2-H_2.

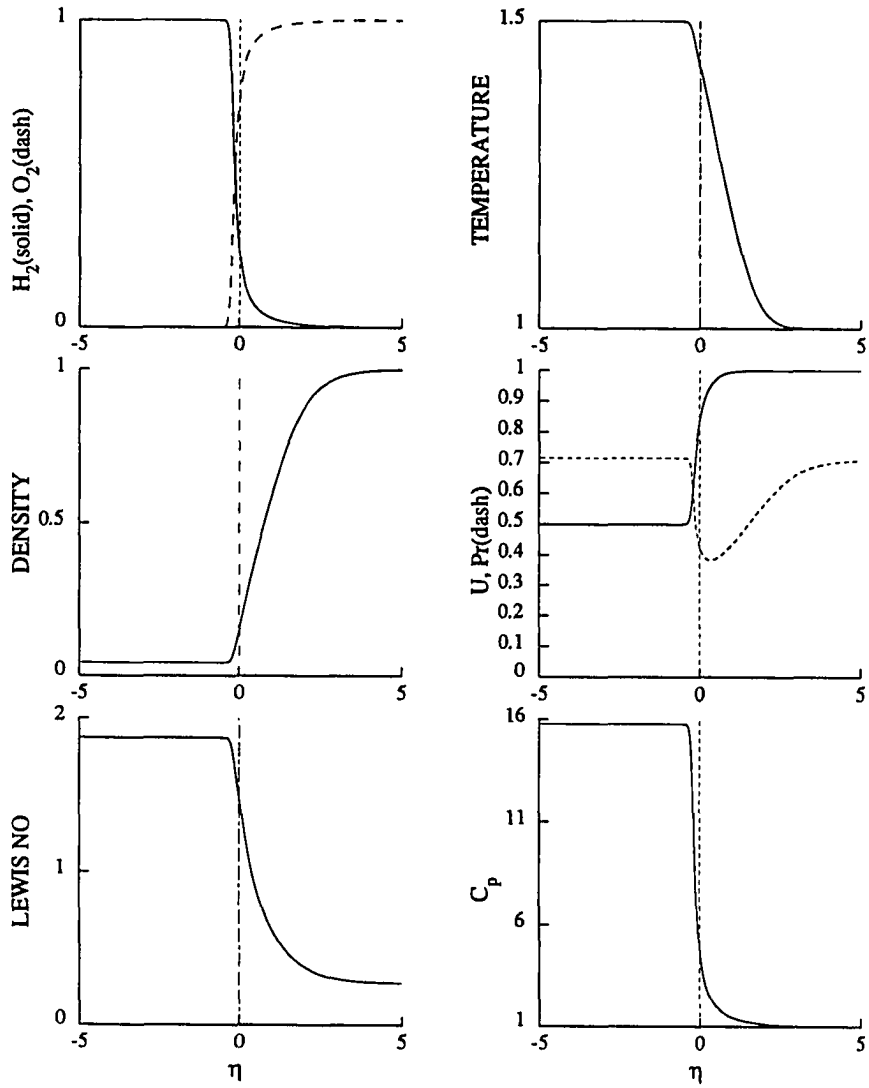

Figure 4.2: Mixing layer structure for H_2-O_2.

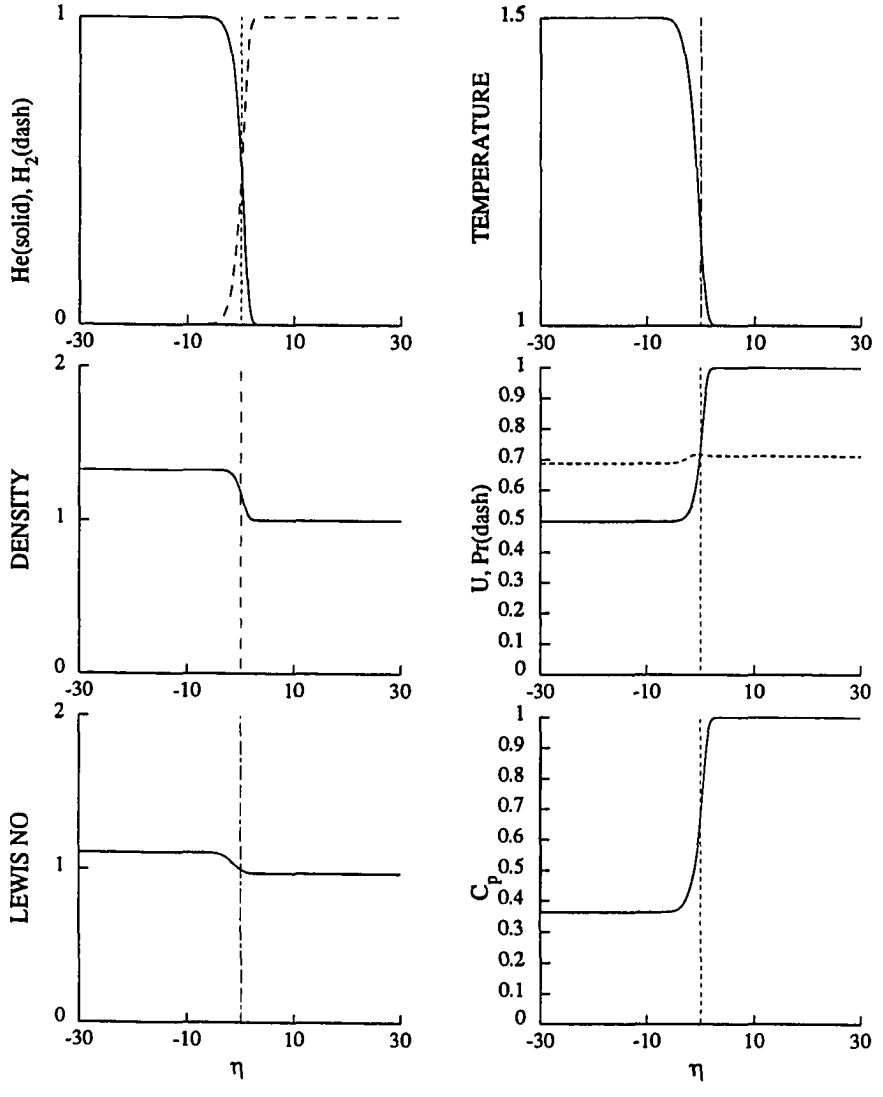

Figure 4.3: Mixing layer structure for He-H_2.

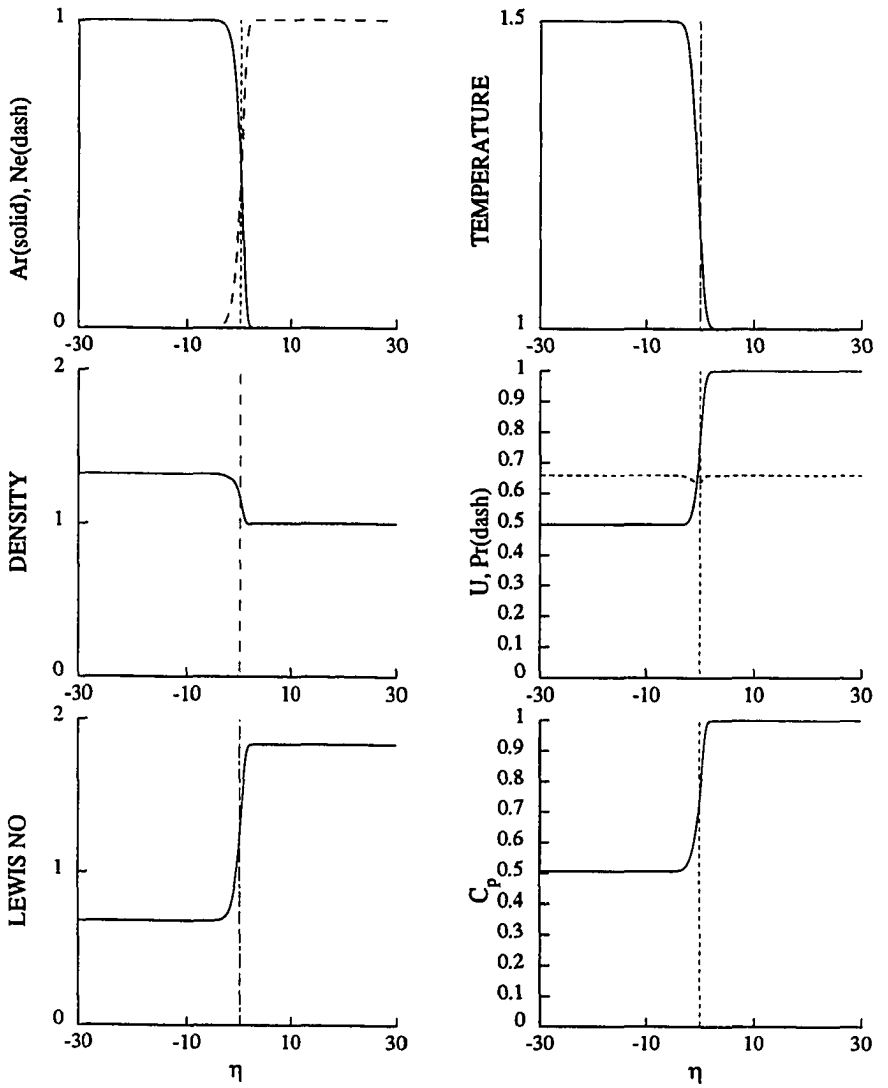

Figure 4.4: Mixing layer structure for *Ar-Ne*.

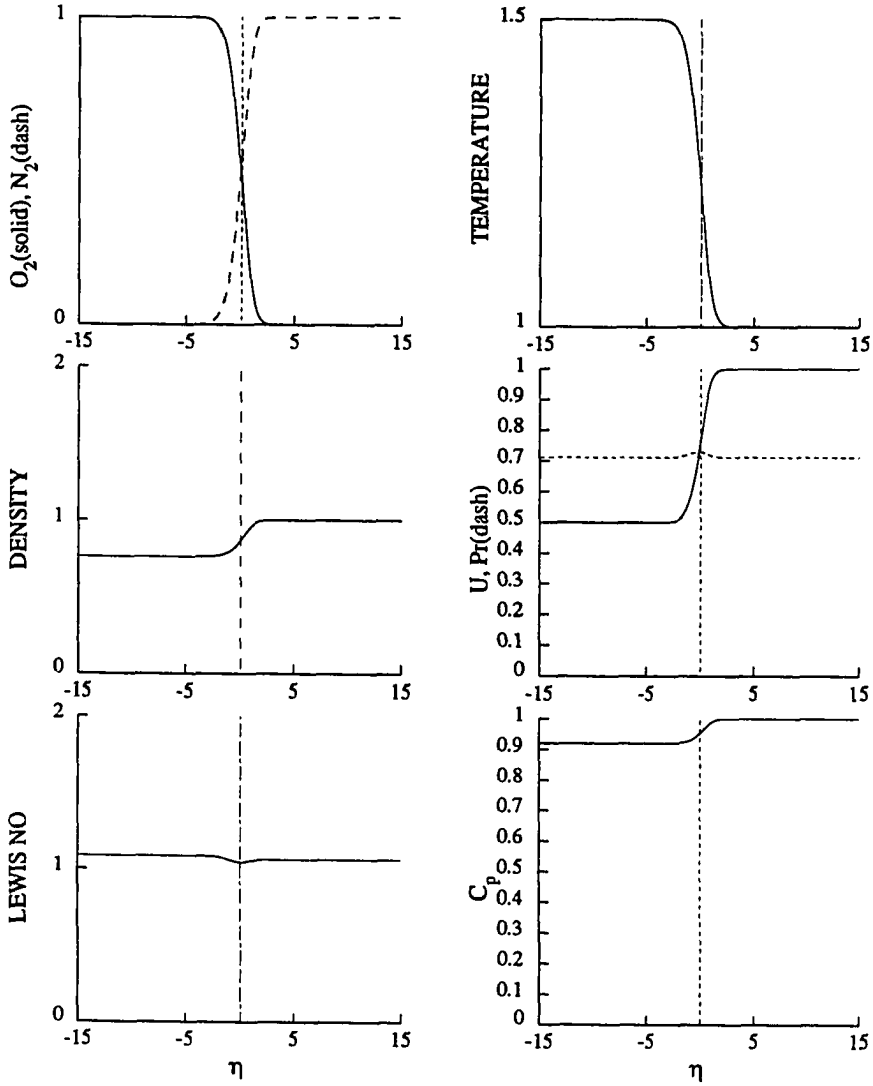

Figure 4.5: Mixing layer structure for O_2-N_2.

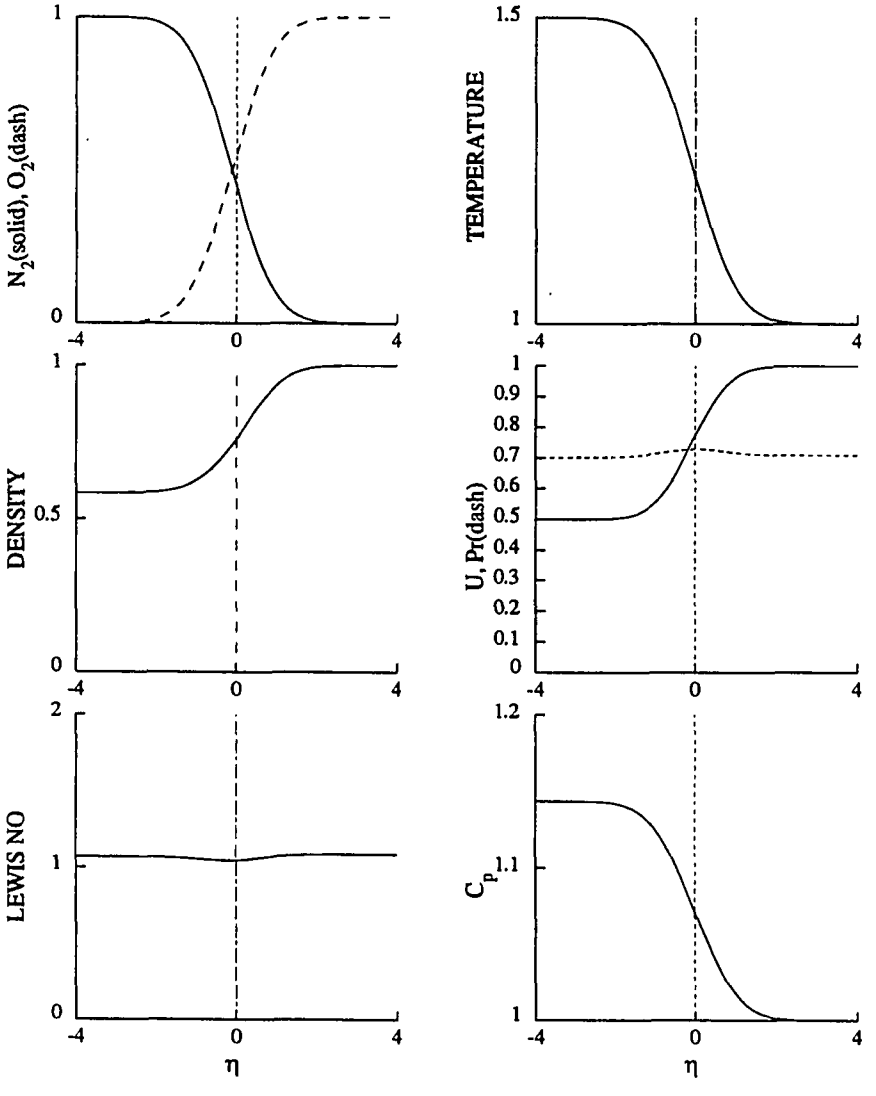

Figure 4.6: Mixing layer structure for N_2-O_2.

Chapter 5

THE STABILITY OF A COMPRESSIBLE MIXING LAYER IN A BINARY GAS

5.1 Introduction

In investigating the stability of mixing layers, it is typical to assume that there exists a local parallel flow about which the governing equations are linearized with respect to spatially and temporally varying disturbances. From this linearization, it is straightforward to calculate either temporal growth rates (assuming fixed spatial wavenumbers) or to calculate spatial growth rates (assuming a fixed temporal frequency). If an instability exists, there is usually a band or bands of wavenumbers (or frequencies) for which there are positive growth rates. These bands are bounded by the neutral modes, whose existence and phase speeds can be determined through

the Lees and Lin regularity condition assuming that the phase speeds are subsonic. Another neutral mode can be found in the limit of the wavenumber going to zero. Additionally, the growth rates of the unstable modes with wave numbers between zero and the Lees/Lin mode can be determined.

The purpose of this chapter is to analyze how the stability characteristics of the mixing layer are effected by the more detailed determination of the mean flow conditions presented in the previous chapter. The mean flow and the stability conditions for two simple models will be determined to compare the results of the stability analysis.

5.2 Mean Flow

Three laminar mixing models will be studied here to determine the mean flow structure and then the stability characteristics. The mean flow of a system of two gases initially separated by a splitter plate then allowed to mix by diffusion and convection has the same geometry, governing equations, initial and boundary conditions presented in the last chapter. The models differ in how the transport properties, thermal conductivity (λ), coefficient of viscosity (μ), binary diffusion coefficient (D_{12}) and thermal heat capacity (C_p), are determined. The models are described below:

- Model I: This model assumes Chapman's viscosity law, $\rho\mu = \rho^2 D_{12} = \rho\lambda = 1$, and allows for different but constant $C_{P,i}$. Owing to the nondimensionalization, $C_{P,2} = 1$ and $C_{P,1}$ is the ratio of the specific heat of the gas at $\eta = -\infty$ divided by the specific heat of the gas at $\eta = \infty$. The mean flow equations (4.2.1

through 4.2.6) are given by

$$f''' + 2ff'' = 0, \qquad 1 = F_1 + F_2, \qquad C_P = C_{P,1}F_1 + F_2, \tag{5.2.1}$$

$$T'' + 2Pr_\infty C_P f T' + (\gamma_\infty - 1)M_\infty^2 Pr_\infty f''^2 + Pr_\infty Sc_\infty^{-1}\left[C_{P,1}F_1' + F_2'\right]T' = 0 \tag{5.2.2}$$

and

$$F_1'' + 2Sc_\infty f F_1' = 0. \tag{5.2.3}$$

The temperature and mass fraction equations are coupled. The values of Pr_∞ and Sc_∞ are determined by considering a particular binary system. In this model, the density does not appear explicitly in the mean flow, and its influence is only felt in the stability calculations.

- Model II: The second model assumes that the viscosity is given by the Sutherland viscosity law

$$\mu = \frac{aT^{3/2}}{b+T}, \qquad a = 1 + b \quad \text{and} \quad \text{b} = 110.4\text{K/T}^*.$$

T^* is some reference temperature. The value of a is chosen to be consistent with $\mu_\infty = 1$ at $T_\infty = 1$. Additional assumptions are $\rho D_{12} = \lambda = \mu$ and $C_{P,2} = 1$. The values of Pr_∞, Sc_∞, and $C_{P,1}$ are determined by considering a particular binary system. In this model, the density is determined from the gas law.

- Model III: The last model considered has been presented in the previous chapter. This model will be called the Exact Model.

5.3 Stability Formulation

As is standard in linear stability theory, the flow field is perturbed by introducing wave disturbances of the form $e^{i(\alpha x-\omega t)}$ in the velocity, pressure, temperature, density and mass fractions with amplitudes that are functions of η. Here, ω is the frequency and α is the streamwise wavenumber of the disturbance. For spatial theory, ω is required to be real and solutions are sought for which α is complex. For temporal theory, α is assumed to be real and solutions are sought for which ω is complex. The amplification rates of the disturbances are then $-\alpha_i$ or ω_i, respectively. Substitution into the inviscid compressible equations for a binary gas and linearizing yields the compressible Rayleigh's equation for the normal velocity perturbation (ϕ)

$$\left(\frac{\phi'}{\xi}\right)' - \left[\alpha^2 + \frac{1}{U-c}\left(\frac{U'}{\xi}\right)'\right]\phi = 0, \tag{5.3.4}$$

where

$$\xi = \frac{1}{\rho^2}\left[1 - M_\infty^2(U-c)^2\rho\frac{\gamma_\infty}{\gamma}\right] \tag{5.3.5}$$

and

$$\frac{\gamma-1}{\gamma}\rho C_P T = \frac{\gamma_\infty - 1}{\gamma_\infty}. \tag{5.3.6}$$

Here, γ is the ratio of specific heats and c is the complex phase speed $c = \omega/\alpha$. Primes indicate differentiation with respect to the similarity variable η. If the molecular weights are taken to be equal and the thermodynamic quantities are assumed constant ($\gamma = \gamma_\infty$, $\rho T = 1$), then equation (5.3.4) reduces to the classical Rayleigh equation for a single component gas. The boundary conditions for ϕ are obtained by considering

the limiting form as $\eta \rightarrow \pm\infty$. The solutions are of the form

$$\phi \rightarrow \exp(\pm\Omega_{\pm}\eta), \tag{5.3.7}$$

where

$$\Omega_{+}^2 = \alpha^2\left[1 - M_{\infty}^2(1-c)^2\right] \quad \text{and} \quad \Omega_{-}^2 = \frac{\alpha^2}{\beta_\rho^2}\left[1 - \mathrm{M}_{\infty}^2(\beta_{\mathrm{U}} - \mathrm{c})^2\frac{\beta_\rho}{\beta_\gamma}\right]. \tag{5.3.8}$$

β_ρ and β_γ are defined by

$$\beta_\rho\beta_T W = 1 \quad \text{and} \quad \beta_\gamma = \frac{\gamma_{-\infty}}{\gamma_{\infty}}.$$

The values of the ratio β_γ for the different gases considered in this study are given in Table 5.1. Although, the case of a gas mixing with itself is not applicable to this study, it is interesting to observe that β_γ is not unity for those gases with a temperature dependent heat capacity (H_2, N_2 and O_2). If Ω_{+}^2 is positive, then the disturbances decay exponentially as $\eta \rightarrow \infty$. If, on the other hand, Ω_{+}^2 is negative, then the disturbance oscillates, indicating that acoustic waves are radiating away from the mixing layer. Similar statements can be made for Ω_{-}^2. c_+ and c_- are defined as the values of the phase speed for which Ω_{+}^2 and Ω_{-}^2 vanish, respectively. Thus

$$c_+ = 1 - \frac{1}{M_{\infty}} \quad \text{and} \quad \mathrm{c}_- = \beta_{\mathrm{U}} + \frac{1}{\mathrm{M}_{\infty}\sqrt{\beta_\rho/\beta_\gamma}}. \tag{5.3.9}$$

c_+ is the phase speed of a sonic disturbance in the fast stream and c_- is the phase speed of a sonic disturbance in the slow stream. At

$$M_{\infty} = M_* \equiv \frac{1 + \sqrt{\beta_\gamma/\beta_\rho}}{1 - \beta_U}, \tag{5.3.10}$$

c_+ and c_- are equal. A "convective" Mach number can now be defined for a two-dimensional binary gas as

$$M_c = \frac{M_\infty}{M_*} \equiv \frac{M_\infty(1-\beta_U)}{1+\sqrt{\beta_\gamma/\beta_\rho}}, \tag{5.3.11}$$

where M_* is the Mach number at which the sonic speeds of the two streams are equal. With this definition, all disturbances are supersonic for $M_c > 1$. This definition of the convective Mach number is based on the freestream Mach number at $\eta = \infty$ in the laboratory frame and is independent of the speed of the large-scale structures and the speed of the most unstable wave. The values of M_* for the W values considered here are shown in Figure (5.1). Figure (5.1) also shows the expanded view for $0 < W < 2$. The dashed line shows the value of M_* for a system with the $W = 1$ and $\beta_\gamma = 1$.

The nature of the disturbances can now be illustrated by Figure (5.2), which shows $c_\pm$ versus M_c for the particular case of *Ar-He*. Figure (5.3) is a similar plot for the *He-Ar* case. These curves divide the c_r - M_c plane into four regions, where c_r is the real part of c. Also shown, as dashed lines, are the bounds for c_r; namely, $c_r \in [\beta_U, 1] \equiv [0.5, 1]$. If a disturbance exists with a M_c and c_r in region 1, then Ω_+^2 and Ω_-^2 are both positive and the disturbance is subsonic at both boundaries; it is classified as a subsonic mode. In region 3, both Ω_+^2 and Ω_-^2 are negative and hence the disturbance is supersonic at both boundaries, and is classified as a supersonic-supersonic mode. In region 2, Ω_+^2 is positive and Ω_-^2 is negative, and the disturbance which is subsonic at infinity and supersonic at negative infinity is classified as a fast supersonic mode. Finally, in region 4, Ω_+^2 is negative and Ω_-^2 is positive so the disturbance is supersonic at infinity and subsonic at negative infinity, and is classified

as a slow supersonic mode.

To complete the stability problem, the appropriate boundary conditions of either spatial or temporal stability, for either damped or outgoing waves in the fast and slow freestreams are, respectively,

$$\phi \to e^{-\Omega_+ \eta} \quad \text{if } c_r > c_+, \qquad \phi \to e^{-i\eta\sqrt{-\Omega_+^2}} \quad \text{if } c_r < c_+, \tag{5.3.12}$$

$$\phi \to e^{\Omega_- \eta} \quad \text{if } c_r < c_-, \quad \text{and} \quad \phi \to e^{-i\eta\sqrt{-\Omega_-^2}} \quad \text{if } c_r > c_-. \tag{5.3.13}$$

5.4 Neutral Modes

To illustrate how a binary gas may alter the stability characteristics, the neutral phase speeds for various values of W are presented below.

5.4.1 Lees-Lin Regularity Factor

The Lees-Lin regularity factor is obtained from equation (5.3.4). Assuming a real phase speed ($c_i = 0$), the denominator $(U - c)$ will reach zero at some value of η making equation (5.3.4) singular. Since this is nonphysical, it must be that

$$\left[\left(\frac{U'}{\xi}\right)'\right]_{U=c} = 0. \tag{5.4.14}$$

Evaluating equation (5.3.5) at $U = c$ gives,

$$[\xi]_{U=c} = \frac{1}{\rho^2}. \tag{5.4.15}$$

The Lees-Lin regularity factor is reduced to

$$S(\eta) = \left(\rho^2 U'\right)'. \tag{5.4.16}$$

If a neutral mode exists in region 1 of Figures (5.2) or (5.3), then the neutral phase speed c_N is given by $c_N = U(\eta_c)$ provided $\alpha \neq 0$. Here, η_c is the zero of the Lees-Lin regularity factor

$$S(\eta) = \rho^2 \left[U'' - 2\left(\frac{T'}{T} + \frac{G'}{G}\right)\right] U', \quad \text{where} \quad G = WF_1 + F_2. \tag{5.4.17}$$

That is, $S(\eta_c) = 0$ corresponds to the neutral subsonic phase speed $c_N = U(\eta_c)$. The corresponding neutral wavenumber and frequency must be determined numerically. These modes are called regular subsonic neutral modes. If, on the other hand, a neutral mode exists in regions 2, 3 or 4, the Lees-Lin regularity condition can not be used and thus the phase speed of the neutral modes must, in general, be found numerically. These modes are called singular neutral modes.

Typical plots of $S(\eta)$ from the Exact Model are shown in Figure (5.4) for the of argon-helium system and the nitrogen-hydrogen system. In each case, there is only one zero of S, although the location differs. The difference in location implies that the neutral phase speed c_N must also be different. The locations, η_c, of the zero of S for the different binary systems are given in Table (5.2), and the corresponding neutral phase speeds given in Table (5.3). In Figures (5.5) and (5.6),the neutral phase speeds are plotted as a function of the molecular weight ratio W. Figure (5.5) shows the results for Model I and the Exact Model . Figure (5.6) shows the Exact Model and Model II. Each figure includes an expanded view of $0 < W \leq 2$ for clarity. Model I under predicts for the higher values of W when compared to the Exact Model and the difference gets larger for larger values of W. Model II is a better overall fit to the Exact Model for low values of W; at higher values it first over predicts then under

predicts.

The Exact Model indicates that the neutral phases speed c_N essentially increases with the molecular weight ratio W, or, equivalently, decreases as β_ρ increases. For Model I and Model II, the monotonic relationship holds for W less than 5. Above $W = 5$, Model I and Model II show a decrease with increasing W. The exceptions to all trends are the near equal W pairs. In Chapter 4, the different structures for the gas combinations of He-H_2 and Ar-Ne with W values of 0.504 and 0.505 were examined. The difference for this pair, as well as others can be seen in Figures (5.5) and (5.6). All three models produce different phase speeds for the pair. This is to be expected since the mean flows are different.

5.4.2 Zero Wave Number Modes

In addition to the neutral modes with $\alpha_N \neq 0$ there may exist neutral modes having zero wavenumber. The phase speed of such modes do not satisfy the Lees-Lin regularity condition but can be found by an asymptotic analysis of equation(5.3.4) in the limit $\alpha \to 0$ (Grosch [6]). In this case, an expansion of the solution in powers of α, along the lines previously used by Drazin and Howard [21] and Blumen, Drazin and Billings [22] in related studies, yields an eigenvalue relation which is analytically tractable. Described below is the extension of these results for binary gases.

The leading order term in an α-expansion is independent of the detailed form of the mean profile, and only depends on the basic flow characteristics at infinity. This is to be expected from physical arguments because the wavelength of the instability in the limit $\alpha \to 0$ is much larger than the length scale over which the undisturbed flow

is non-uniform. For the supersonic-supersonic case, setting the leading-order term in the expansion to zero yields an equation for c_N:

$$[M_\infty^2(\beta_U - c_N)^2\beta_\rho\beta_\gamma^{-1} - 1](1 - c_N)^4 = \beta_\rho^2[M_\infty^2(1 - c_N)^2 - 1](\beta_U - c_N)^4. \quad (5.4.18)$$

If the molecular weights are taken to be equal and the thermodynamic quantities are assumed constant ($\gamma = \gamma_\infty$ and $\rho T = 1$), then this equation reduces to (5.3a) of Miles [23], if his result is expressed in the notation used here. In general, this sixth-order polynomial must be solved numerically to determine c_N as a function of M. For the special case of $\beta_\gamma = 1$ (i.e., both gases are monatomic), the following can be found:

- A single real root of equation (5.4.18) exists for

$$M_\infty \geq M_* \equiv (1 + \beta_\rho^{-1/2})/(1 - \beta_U), \quad (5.4.19)$$

  with phase speed

$$c_N = (\beta_U + \beta_\rho^{-1/2})/(1 + \beta_\rho^{-1/2}). \quad (5.4.20)$$

  This is classified as a constant speed supersonic-supersonic neutral mode lying in region 3 of the c_r - M plane. It is independent of Mach number and corresponds to the phase speed at which the sonic speeds in the two streams are equal.

- A double root first appears at

$$M_{CR} = (1 + \beta_\rho^{-1/3})^{3/2}/(1 - \beta_U), \quad (5.4.21)$$

  with phase speed

$$c_N = (\beta_U + \beta_\rho^{-1/3})/(1 + \beta_\rho^{-1/3}). \quad (5.4.22)$$

There are three distinct real roots for $M_\infty > M_{CR}$. One of these is the phase speed of the constant speed supersonic-supersonic neutral mode while the other two roots must be found numerically from equation (5.4.18). For the special case of $\beta_\rho = 1$, these roots are given by

$$c_N = \frac{1+\beta_U}{2} \pm \frac{1}{2M_\infty}[M_\infty^2(1-\beta_U)^2 + 4 - 4(M_\infty^2(1-\beta_U)^2+1)^{1/2}]^{1/2}. \quad (5.4.23)$$

The root which corresponds to the $(+/-)$ sign is classified as a fast/slow supersonic-supersonic neutral mode. All three of these neutral modes lie in region 3.

5.5 Growth Rates

Equation (5.3.4) is solved numerically for the growth rates $\alpha_i < 0$ corresponding to a particular value of ω. Tables (5.4) and (5.5) present the maximum growth rates for various gas combinations for Model I, Model II and the Exact Model for $W < 1$ and $W > 1$ respectively. All growth rates are for $M_\infty = 0$ except where otherwise indicated. The gas combinations are presented in order of increasing value of W. In general, the Exact Model yields a lower maximum growth rate than that predicted for Models I and II when $W < 1$. As the value of W increases, the maximum growth rate decreases to the point where numerical error, due to the presence of the critical layer near the singular point at $U - c = 0$, is of the same order as the growth rates. Thus the numerical procedure can not be continued for the largest values of W.

Figures (5.7) and (5.8) show the growth rate curves for various combinations of gases for the Exact Model. In Figure (5.7), the two dashed lines are the near equal W

pair Ar-Ne and He-H_2. The growth rate curves are different as would be expected from previous analysis which showed different mean flow structures. Figure (5.8) shows growth rates for the higher W value combinations listed in Tables (5.4) and (5.5), the general trend of the decrease in growth rate for higher W is evident. Figure (5.9) compares the growth rate curve of Model I and the Exact Model for the O_2-H_2 case. Not only is the maximum growth rate higher for the Exact Model but the range of ω is smaller. Figures (5.10) and (5.11) are the growth rate curves for the Ar-N_2 and N_2-Ar cases for convective Mach numbers M_c=0, 0.2, 0.4, 0.6, 0.8 and 1.0. These figures show a decrease of the growth rates as the convective Mach number increases, as well as a large decrease in the range of frequencies for which the flow is unstable.

5.6 Conclusion

From the figures and tables presented it is seen that differing molecular weights have a significant effect on the phase speeds and growth rates of the disturbances. Using more precise calculations of the transport properties yields stability characteristics of a laminar mixing layer that are different than those obtained with the simplified models. Thus, weight ratios and methods of calculating the transport properties should be taken into account when computing stability characteristics of compressible mixing layers in binary gases.

Table 5.1: The ratio β_γ, defined as the ratio of specific heats at $\eta = -\infty$ divided by the ratio of specific heats at $\eta = \infty$, for the different gases considered in this study. The top row corresponds to the gases in the freestream at $\eta = \infty$, while the first column corresponds to the gases in the freestream at $\eta = -\infty$.

	H_2	He	Ne	N_2	O_2	Ar
H_2	0.995	0.839	0.839	0.999	1.002	0.839
He	1.186	1.000	1.000	1.191	1.195	1.000
Ne	1.186	1.000	1.000	1.191	1.195	1.000
N_2	0.992	0.836	0.836	0.996	1.000	0.836
O_2	0.977	0.824	0.824	0.981	0.985	0.824
Ar	1.186	1.000	1.000	1.191	1.195	1.000

Table 5.2: The location $S(\eta_c) = 0$ at $M_\infty = 0$, $\beta_U = 0.5$ and $\beta_T = 1.5$ for the different gases considered in this study. The top row corresponds to the gases in the freestream at $\eta = \infty$, while the first column corresponds to the gases in the freestream at $\eta = -\infty$. The notation NA means not applicable for a binary gas.

	H_2	He	Ne	N_2	O_2	Ar
H_2	NA	0.096	0.124	0.228	0.208	0.186
He	0.219	NA	0.246	0.373	0.346	0.317
Ne	−0.313	−0.255	NA	0.379	0.364	0.368
N_2	−0.795	−0.583	−0.057	NA	0.168	0.178
O_2	−0.814	−0.617	−0.052	0.200	NA	0.200
Ar	−1.013	−0.769	−0.110	0.153	0.145	NA

Table 5.3: The neutral phase speeds c_N at $M_\infty = 0$, $\beta_U = 0.5$ and $\beta_T = 1.5$ for the different gases considered in this study. The top row corresponds to the gases in the freestream at $\eta = \infty$, while the first column corresponds to the gases in the freestream at $\eta = -\infty$. The notation NA means not applicable for a binary gas.

	H_2	He	Ne	N_2	O_2	Ar
H_2	NA	0.829	0.896	0.922	0.924	0.926
He	0.780	NA	0.892	0.914	0.916	0.919
Ne	0.668	0.690	NA	0.851	0.856	0.868
N_2	0.628	0.649	0.757	NA	0.817	0.829
O_2	0.627	0.646	0.753	0.808	NA	0.826
Ar	0.614	0.631	0.735	0.789	0.794	NA

Table 5.4: The maximum spatial growth rates for various binary systems and for the three models used in the study. The gases are listed in order of increasing W ($W < 1$).

F_1	F_2	Model I	Model II	Model III
Ar	H2	−0.2672	−0.0558	−0.0652
O2	H2	−0.2332	−0.0562	−0.0670
N2	H2	−0.2317	−0.0587	−0.0704
Ar	He	−0.2225	−0.0697	−0.0818
Ne	H2	−0.1448	−0.0593	−0.0619
O2	He	−0.1876	−0.0687	−0.0809
N2	He	−0.1799	−0.0697	−0.0846
Ne	He	−0.1229	−0.0676	−0.0700
He	H2	−0.0744	−0.0612	−0.0550
Ar	Ne	−0.0754	−0.0599	−0.0709
O2	Ne	−0.0626	−0.0540	−0.0647
Ar	N2	−0.0626	−0.0561	−0.0557
N2	Ne	−0.0578	−0.0519	−0.0652
Ar	O2	−0.0521	−0.0538	−0.0550
O2	N2	−0.0521	−0.0498	−0.0500

Table 5.5: The maximum spatial growth rates for various binary systems and for the three models used in the study. The gases are listed in order of increasing W ($W > 1$). NA implies not avaliable.

F_1	F_2	Model I	Model II	Model III
N2	O2	−0.0437	−0.0448	−0.0486
O2	Ar	−0.0390	−0.0409	−0.0437
Ne	N2	−0.0396	−0.0430	−0.0395
N2	Ar	−0.0355	−0.0385	−0.0430
Ne	O2	−0.0357	−0.0403	−0.0381
Ne	Ar	−0.0279	−0.0337	−0.0333
H2	He	−0.0274	−0.0321	−0.0434
He	Ne	−0.0100	−0.0173	−0.0238
He	N2	NA	−0.0140	−0.0178

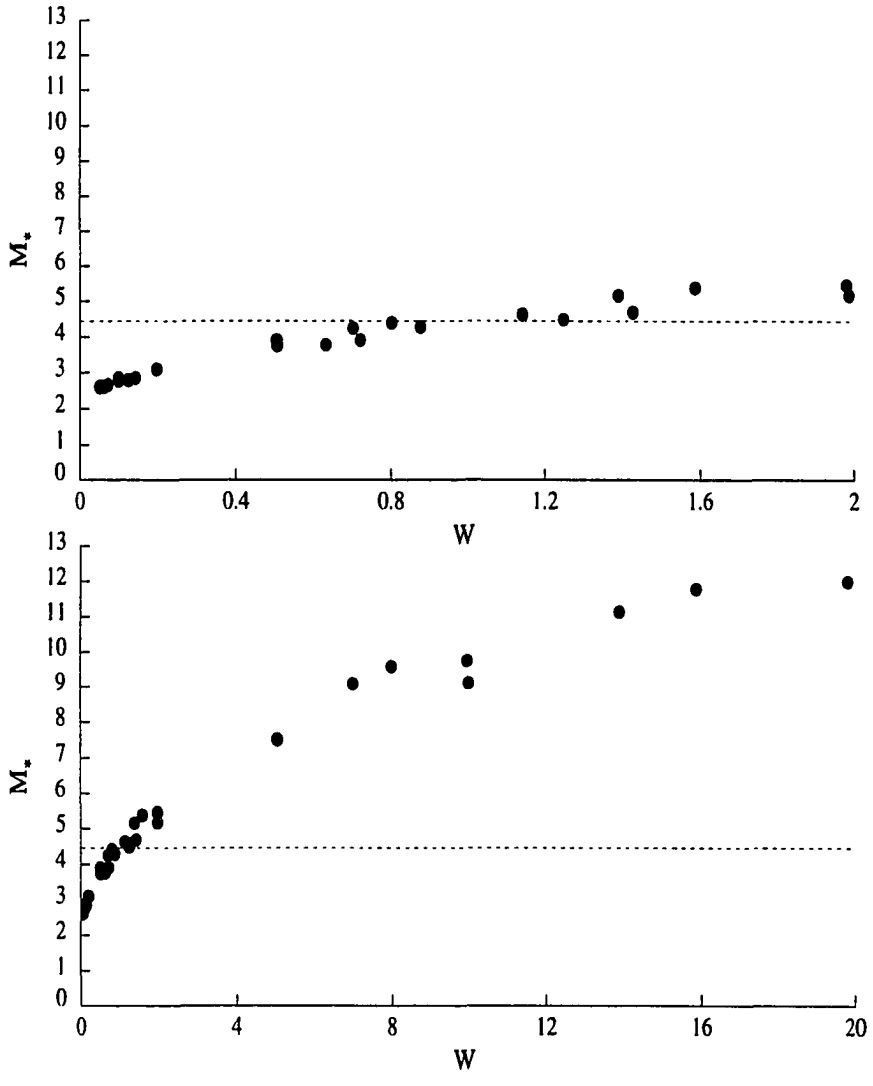

Figure 5.1: Mach number M_* vs W for $\beta_U = 0.5$ and $\beta_T = 1.5$, dashed line indicates M_* for $W = \beta_\gamma = 1$ and $\beta_\rho \beta_T = 1$.

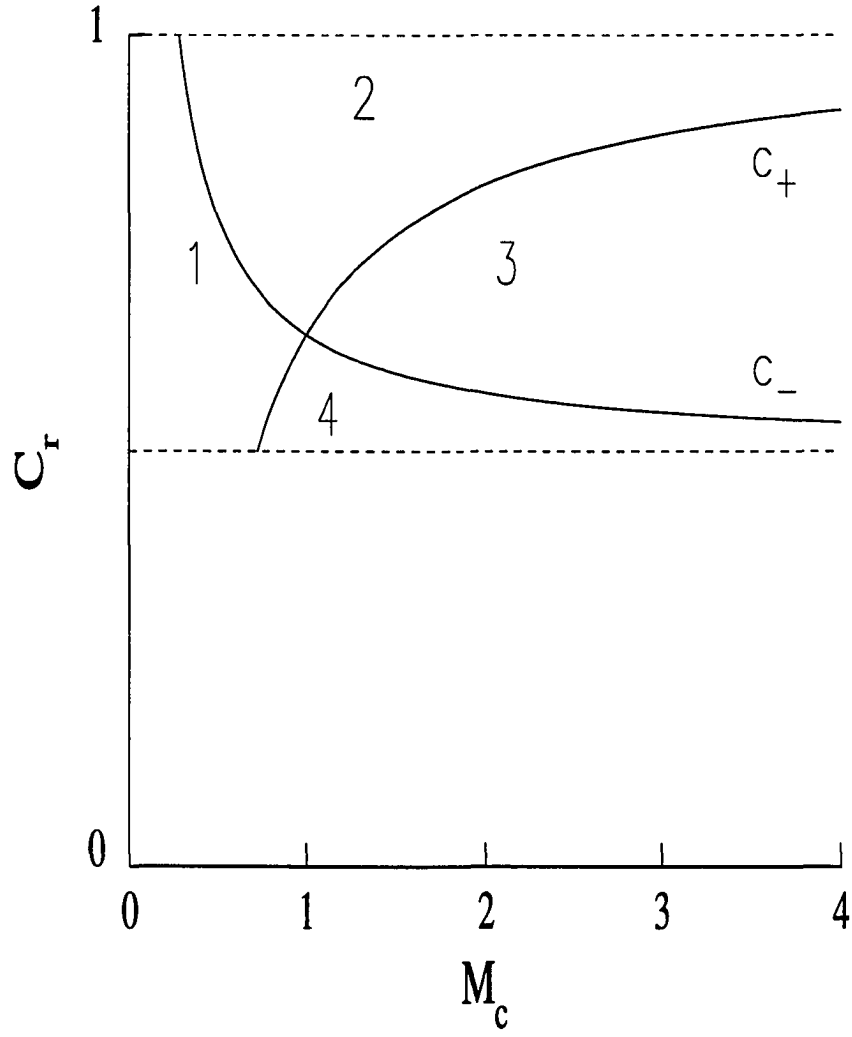

Figure 5.2: Disturbance speed phase diagram C_r vs M_c for *Ar-He*.

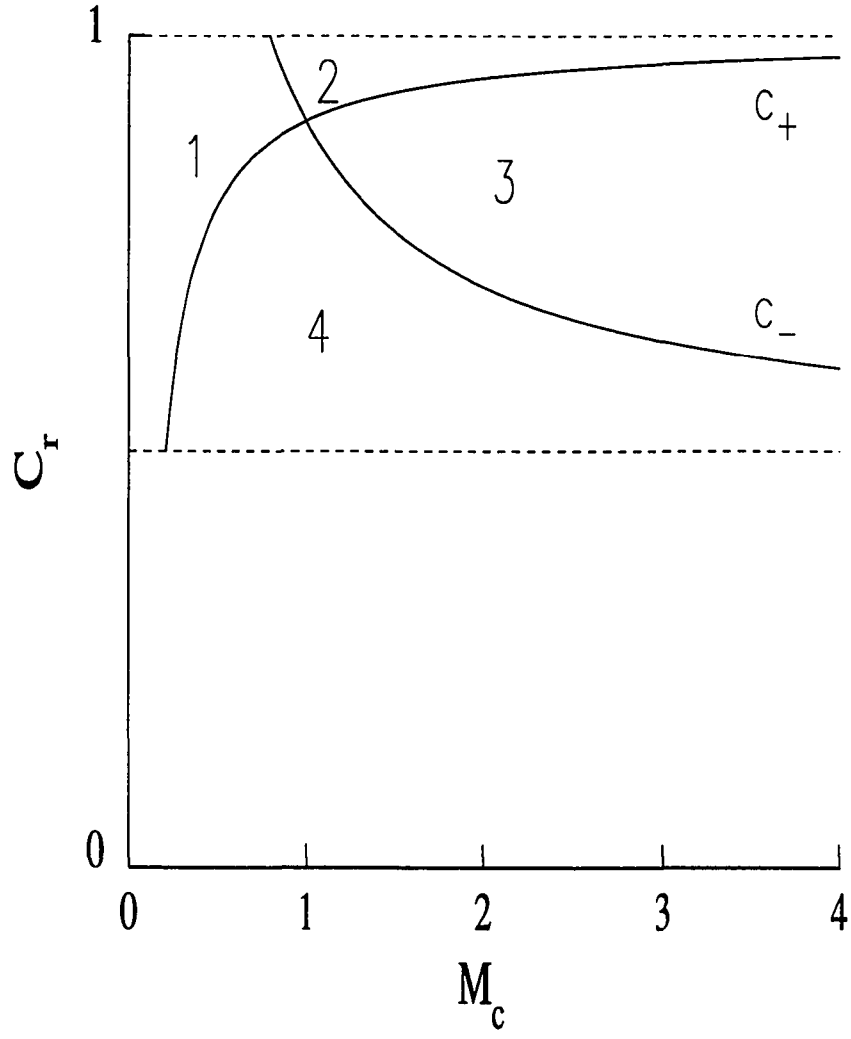

Figure 5.3: Disturbance speed phase diagram C_r vs M_c for *He-Ar*.

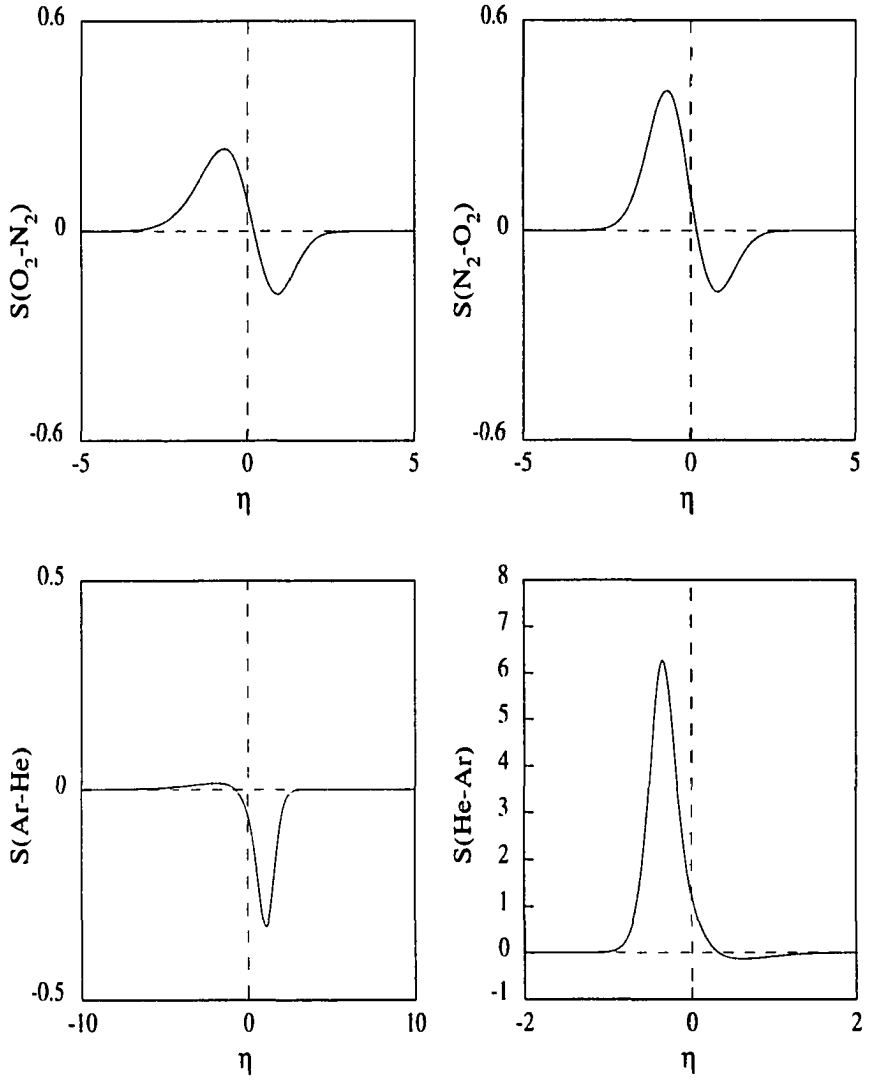

Figure 5.4: Lees-Lin regularity factor S vs η for *Ar-He*, *He-Ar*, O_2-N_2 and N_2-O_2.

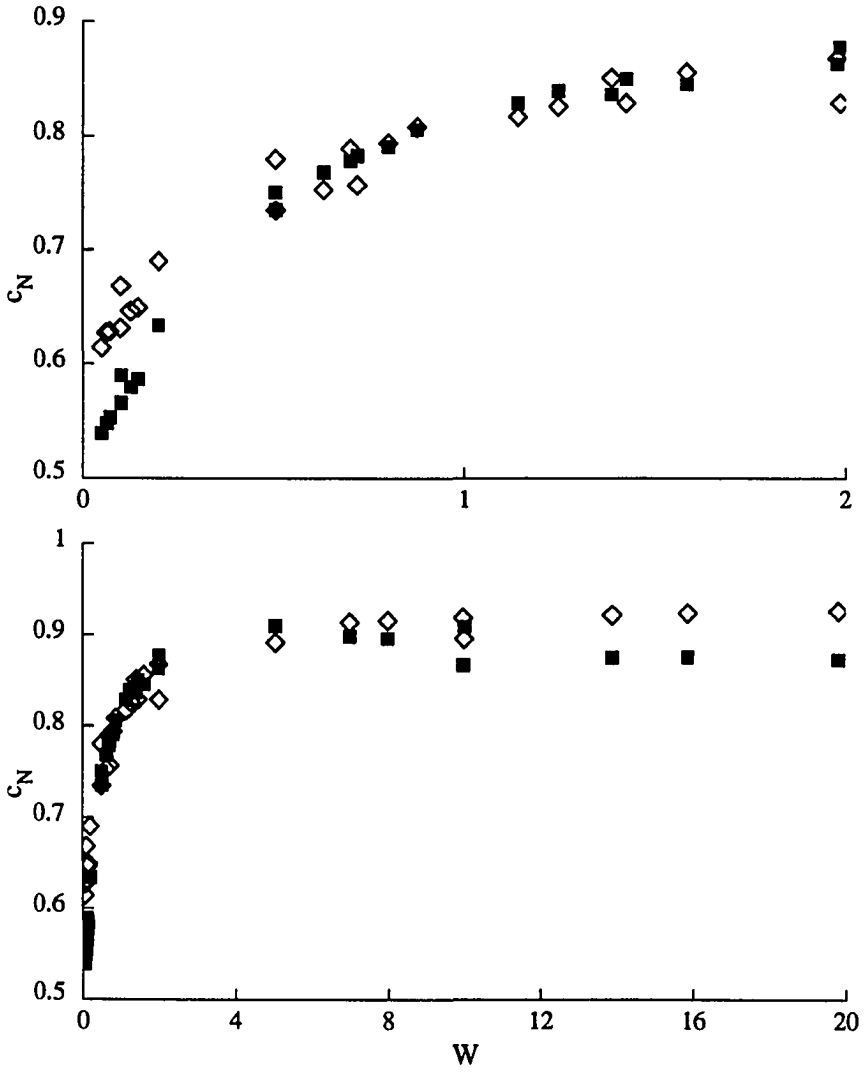

Figure 5.5: Phase speed C_N vs W for Model I (□) and the Exact Model (◇).

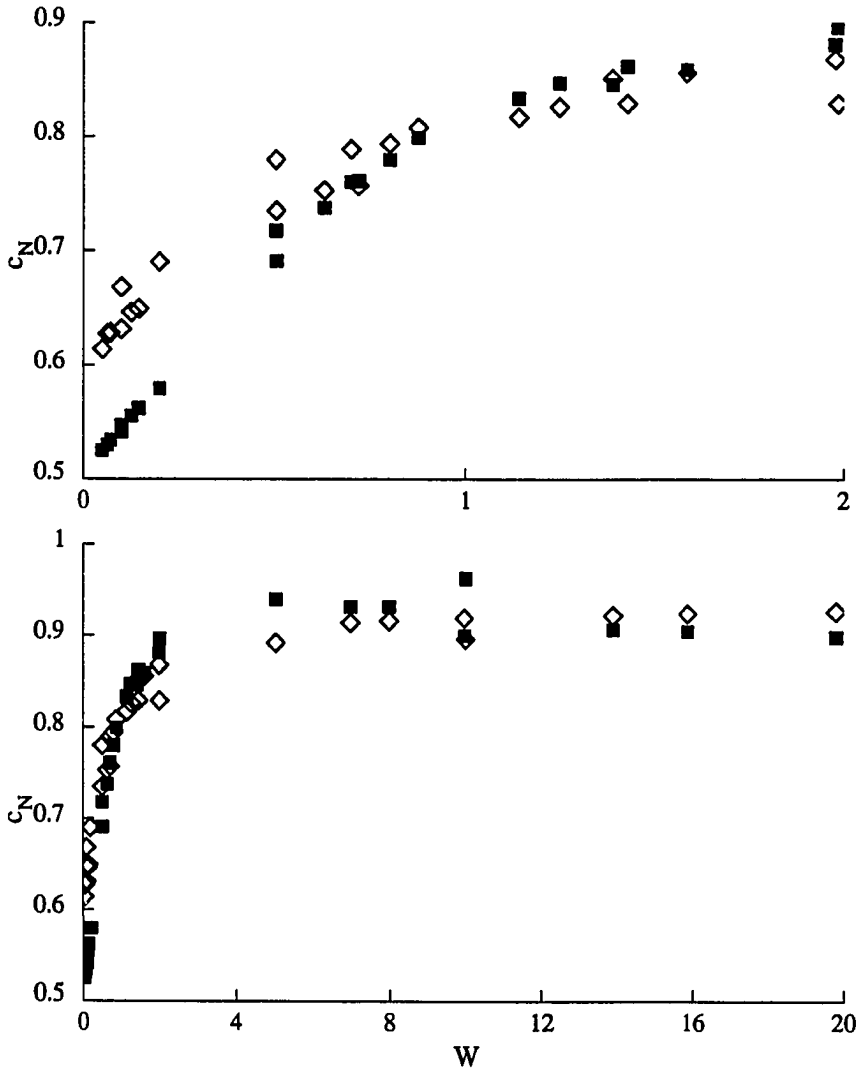

Figure 5.6: Phase speed C_N vs W for Model II (□) and the Exact Model (◇).

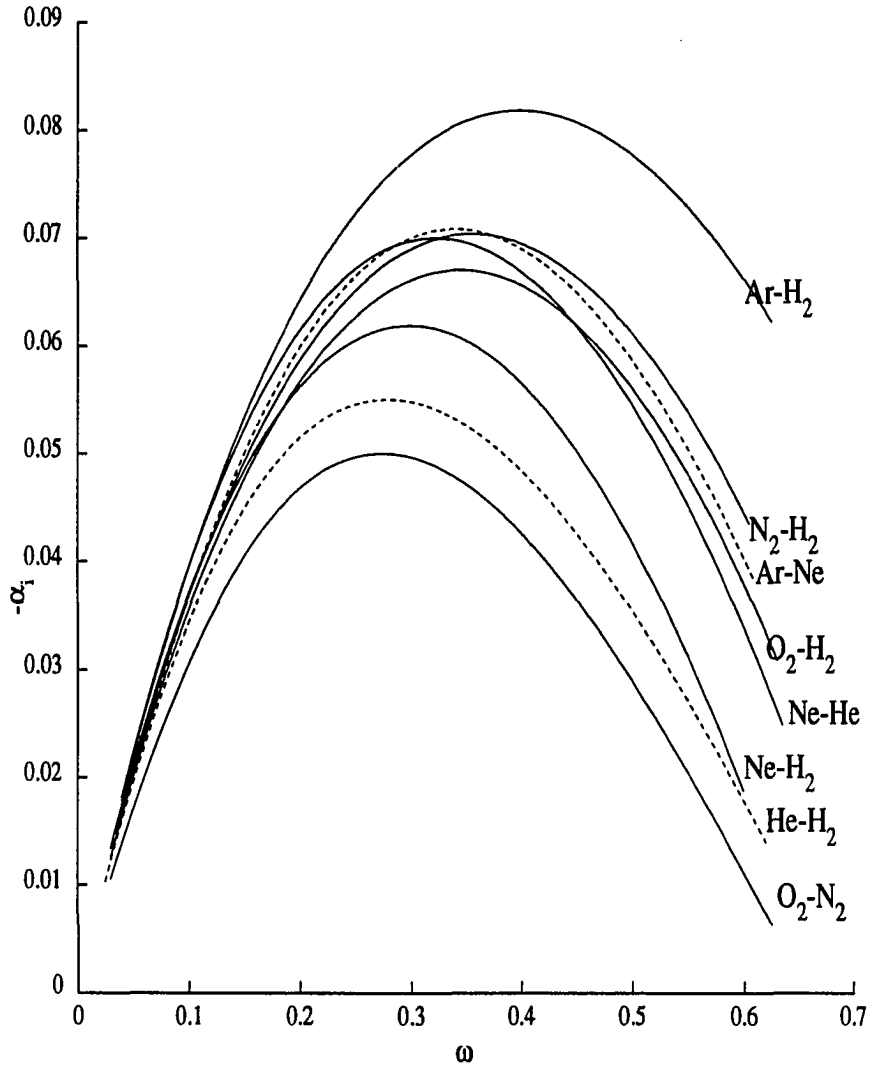

Figure 5.7: Growth rate curves, $-\alpha_i$ vs ω, for lower W values using the Exact Model.

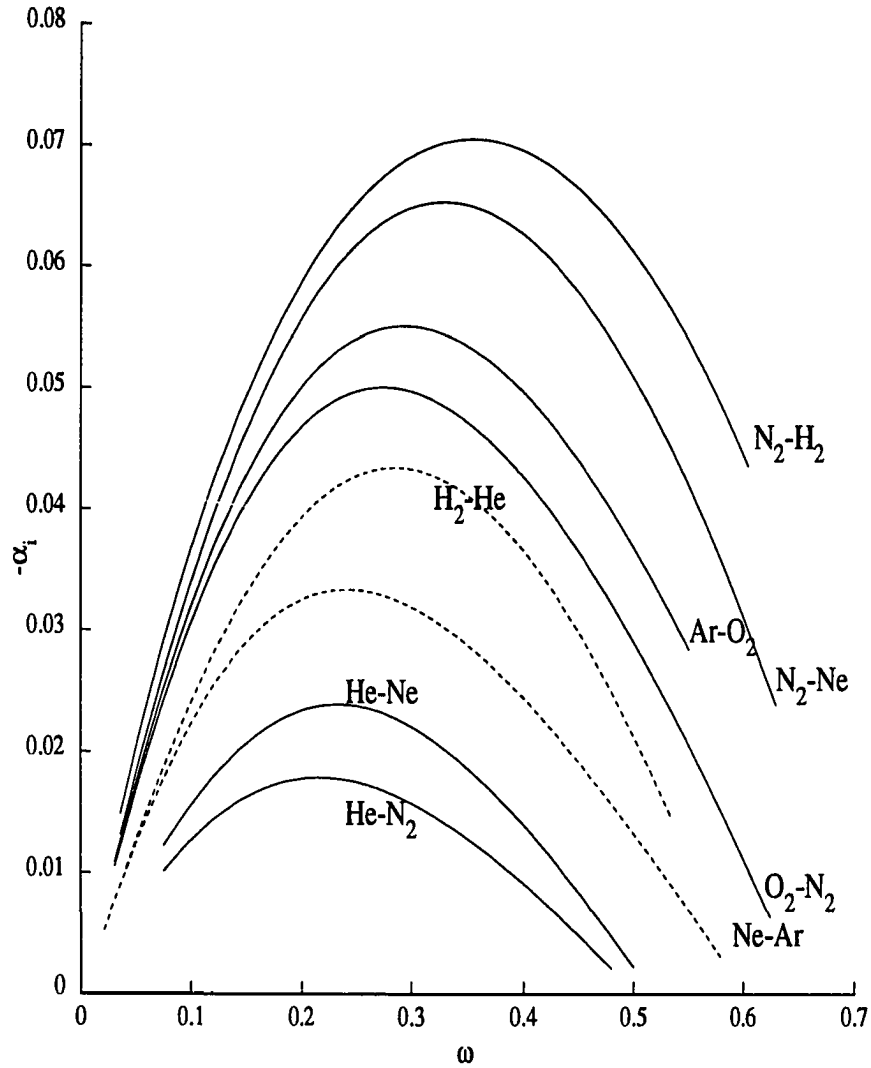

Figure 5.8: Growth rate curves, $-\alpha_i$ vs ω, for higher W values using the Exact Model.

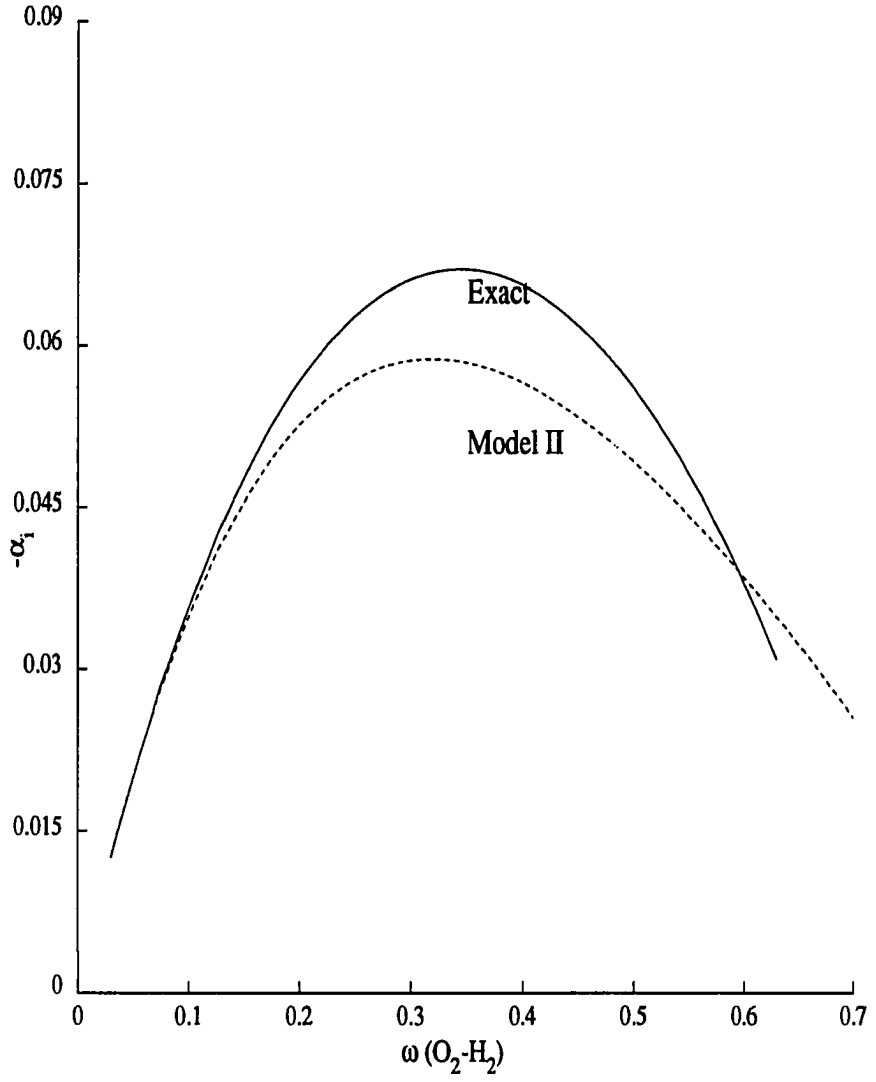

Figure 5.9: Growth rate curves, $-\alpha_i$ vs ω, of the O_2-H_2 system using the Exact Model and Model II.

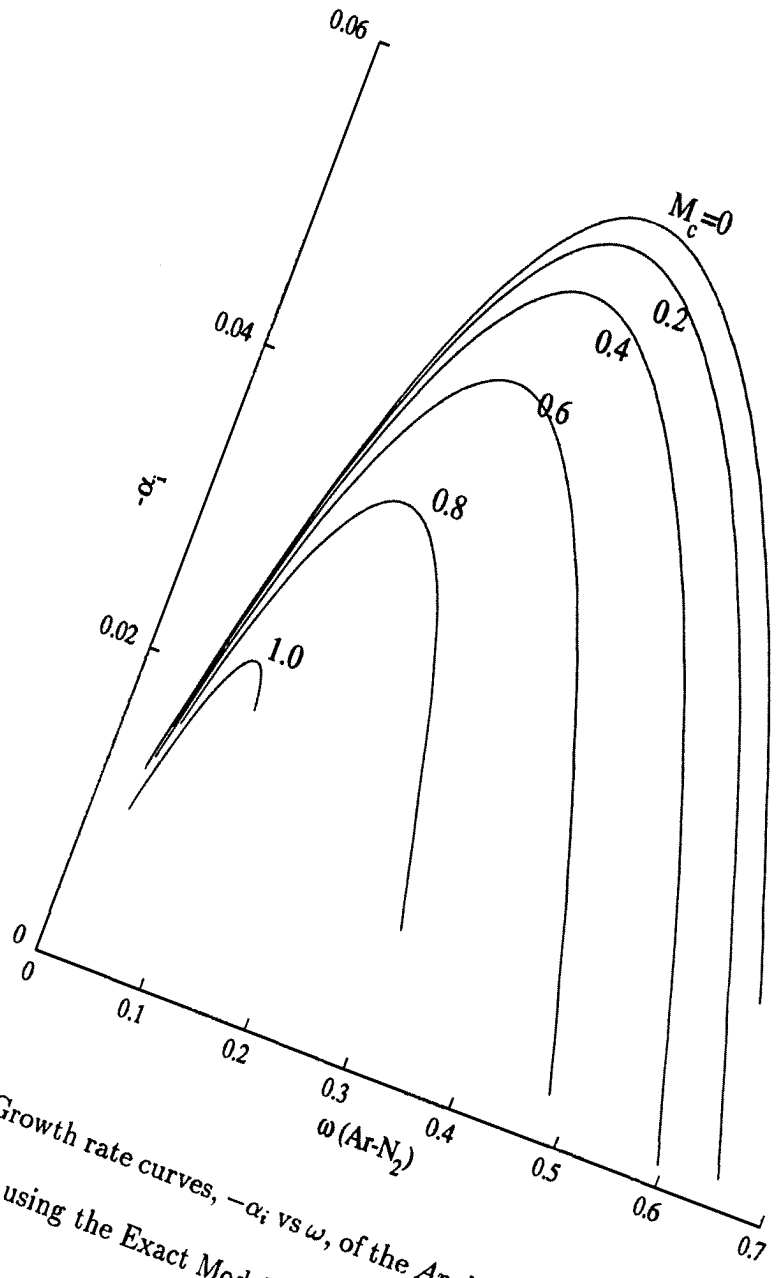

Figure 5.10: Growth rate curves, $-\alpha_i$ vs ω, of the Ar-N_2 system for various convective Mach numbers, using the Exact Model.

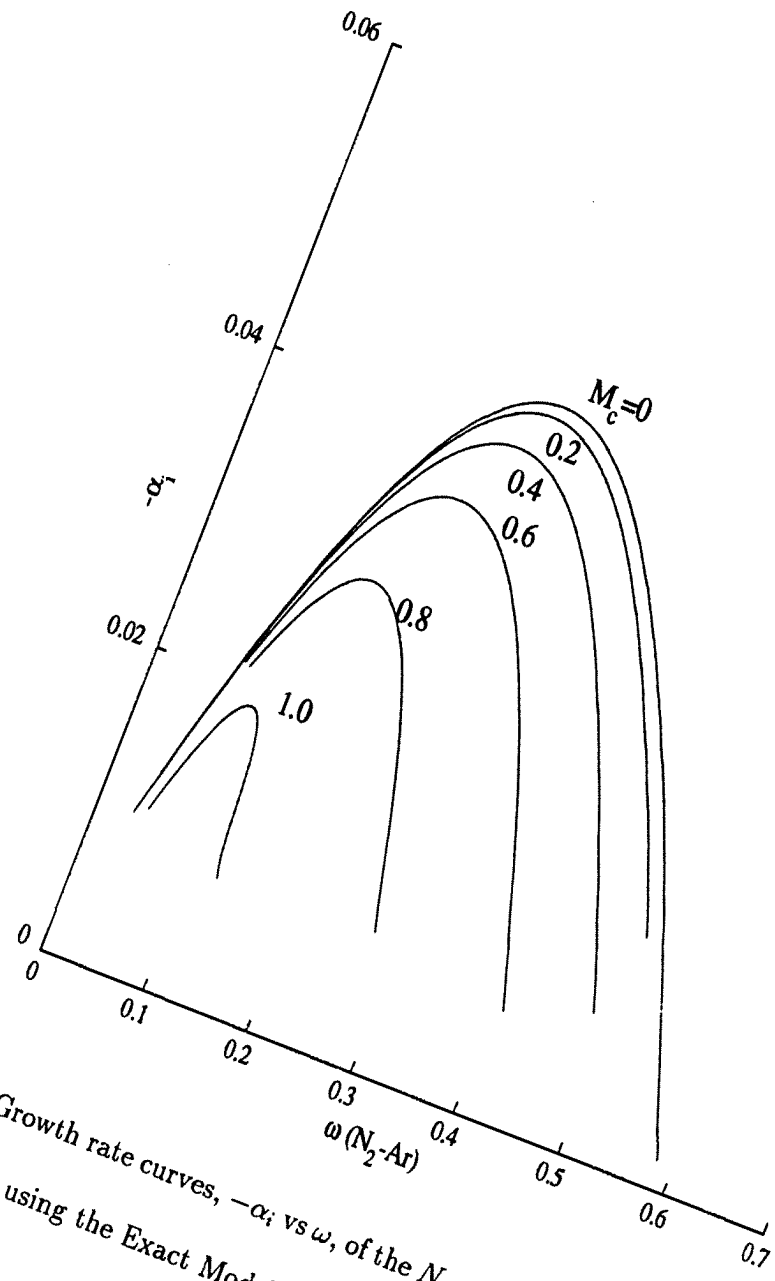

Figure 5.11: Growth rate curves, $-\alpha_i$ vs ω, of the N_2-Ar system for various convective Mach numbers, using the Exact Model.

Chapter 6

SUMMARY

Three different laminar mixing problems have been studied and the results presented. Each study represents an expansion and more detailed look into research previously conducted. Comparison of the results from the work herein with previous work presents new insight into the physical systems modeled.

6.1 Double Vortex Ignition

The double vortex ignition analysis examined the ignition of a constant density fuel-oxidizer non-premixed system with mixing provided by diffusion and two counter-rotating point-vortices. A simplified chemical model was used, as were simplifying values of the transport properties. Results were compared to the classic results of Linan and Crespo [11] which assumed diffusion only and recent work (Macaraeg et al [4] with diffusion and convection provided by a single vortex.

If the fuel-oxidizer ratio is 1.0 and there is no initial temperature difference between

fuel and oxidizer, the ignition times for the double vortex are shorter than the diffusion only case but longer than the single vortex case. The time differences vary with both the vortex strength and the distance between the vortex centers. As the distance between the two vortices gets smaller, ignition times approach the no vortex ignition time, as the distance gets larger the double vortex ignition time approaches the single vortex time. Further comparisons show the different behavior of the ignition times as the relative initial temperature, fuel/oxidizer ratio and Lewis number are varied. The analysis provides a view of the convective effects on the entire convection-diffusion process.

6.2 Reduced Chemical Combustion in a Laminar Mixing Layer

The reduced combustion chemistry of Birkan-Law [1] and a methane-air reduced system of Peters [2] was studied in a laminar mixing layer configuration proposed by Grosch [6]. It was found that the model reduction system (Birkan-Law) and the methane-air reduction system (Peters) gave quantitatively similar results. Both systems needed an initial loading of a reactant besides the fuel and oxidizer. In each case the value of the initial load of this radical affected the ignition distance inversely. However, the levels of the radicals at the point of ignition were unaffected by the initial radical concentration and neither was the post ignition steady flame temperature.

6.3 Structure of a Laminar Mixing Layer in a Binary Gas

The structure and mean flow of two gases mixing in a laminar mixing layer as proposed by [6] was studied for 30 different combinations of six different gases. The thermal transport properties were dynamically calculated using theory and experimental values. The actual molecular weights were used.

The values of Lewis number, Prandtl number and other physical system values were shown to vary greatly from gas combination to gas combination. Different values of the molecular weight ratio produced different profiles. However, cases appeared with nearly identical weight ratios but very different profiles. Numerous supporting graphs were presented.

6.4 Stability of a Laminar Mixing Layer in a Binary Gas

The mean flow of the previous gas mixing system was analyzed for various stability conditions and compared with two simplified systems, each with a much simplier method of determining the transport properties.

In general, the system with the more precisely calculated transport properties had different stability characteristics than did the two simplified models. The variations involved more than just the weight ratio of the gases considered. Tables are provided for the spatially neutral phase speeds and and the maximum growth rates for the

model derived in this study. Growth rate curves are shown for various gas combinations for all three models. The study concludes that stability calculations with the more precise models of the transport properties is recommended when posssible.

Bibliography

[1] M. A. Birkan and C. K. Law. Asymptotic structure and extinction of diffusion flames with chain mechanism. *Combustion and Flame*, 73:127–146, 1988.

[2] N. Peters. Reducing mechanisms. In Mitchell D. Smooke, editor, *Reduced Kinetic Mechanism and Asymptotic Approximations for Methane-Air Flames*, pages 68–85. Springer-Verlag, 1985.

[3] F. E. Marble. Growth of a diffusion flame in the field of vortex. In C. Cassi, editor, *Recent Advances in Aerospace Sciences*, pages 395–413. 1985.

[4] M. G. Macaraeg, T. L. Jackson, and M. Y. Hussaini. Ignition and structure of a laminar diffusion flame in the field of vortex. *Combustion Science and Technology*, 87:363–387, 1992.

[5] T. L. Jackson and C. E. Grosch. Absolute/convective instabilities and the convective mach number in a compressible mixing layer. *Physics of Fluids A*, 6(2):949–954, 1990.

[6] C. E. Grosch. Reacting compressible mixing layers:structure and stability. In J.Buckmaster, T.L.Jackson, and A.Kumar, editors, *Combustion in High-Speed Flows*, pages 131-190. Kluwer, 1994.

[7] T. L. Jackson and C. E. Grosch. Structure and stability of a laminar diffusion flame in a compressible, three-dimensional mixing layer. *Theoretical and Computational Fluid Dynamics*, 6:89-112, 1994.

[8] J. D. Anderson, Jr. *Hypersonic and High Temperature Gas Dynamics*. McGraw-Hill, 1989.

[9] L. Lees and C. C. Lin. Investigation of the stability of the laminar boundary layer. *NACA Technical Note No. 1115*, (1115):1-85, 1946.

[10] D. Thevenin and S. Candel. Effects of variable strain on the dynamics of diffusion flame ignition. *Combustion Science and Technology*, 91:73-94, 1993.

[11] A. Linan and A. Crespo. An asymptotic analysis of unsteady diffusion flames for large activation energies. *Combustion Science and Technology*, 14:95-117, 1976.

[12] B. J. McBride. *Thermodynamic Properties to* 6000° *for 210 Substances involving the First 18 Elements*. NASA, 1963.

[13] D. Papamoschou and A. Roshko. The compressible turbulent shear layer: An experimental study. *J. Fluid Mechanics*, 197:453-477, 1988.

[14] J. L. Hall, P. E. Dimotakis, and H. Rosemann. Experiments in non-reacting compressible shear layers study. *AIAA Paper*, (91-0629), 1991.

[15] Geoffrey C. Maitland. *Intermolecular Forces (Their Origin and Determination.* Claredon, 1981.

[16] Y. S. Touloudian, P.E. Liley, and S.C. Saxena. *Thermal Properties of Matter Volume 11: Viscosity.* Plenum, 1970.

[17] Y. S. Touloudian, P.E. Liley, and S.C. Saxena. *Thermal Properties of Matter Volume 3: Thermal Conductivity.* Plenum, 1970.

[18] J. Bzowski, J. Krestin, E. A. Mason, and F. J. Uribe. Equilibrium and transport properties of gas mixtures at low density. *J. Phys. Chem. Ref. Data*, 19(5):1179–1197, 1990.

[19] J. O. Hirschfelder, C. F. Curtiss, and R. B. Bird. *Molecular Theory of Gases and Liquids.* John Wiley and Sons, 1954.

[20] C. A. Kennedy and T. B. Gatski. Self-similar supersonic variable density shear layers in binary systems. *Physics of Fluids*, 6(2):662–673, 1994.

[21] P. G. Drazin and L. N. Howard. The instability to long waves of unbounded parallel flow. *J.Fluid Mechanics*, 14:257–253, 1962.

[22] W. Blumen, P. G. Drazin, and D. F. Billings. Shear layer instability of an inviscid compressible fluid part 2. *J. Fluid Mechanics*, 71:305–316, 1975.

[23] J. W. Miles. On the disturbed motion of a plane vortex sheet. *J.Fluid Mechanics*, 4:538–552, 1958.

Appendix A

ADDITIONAL FIGURES FOR BINARY GAS MIXTURES ($W < 1$)

Thirty different combinations of gas mixtures were studied. The structure of the mixing layer is presented here for those combinations not covered in Chapter 4 and with $W < 1$.

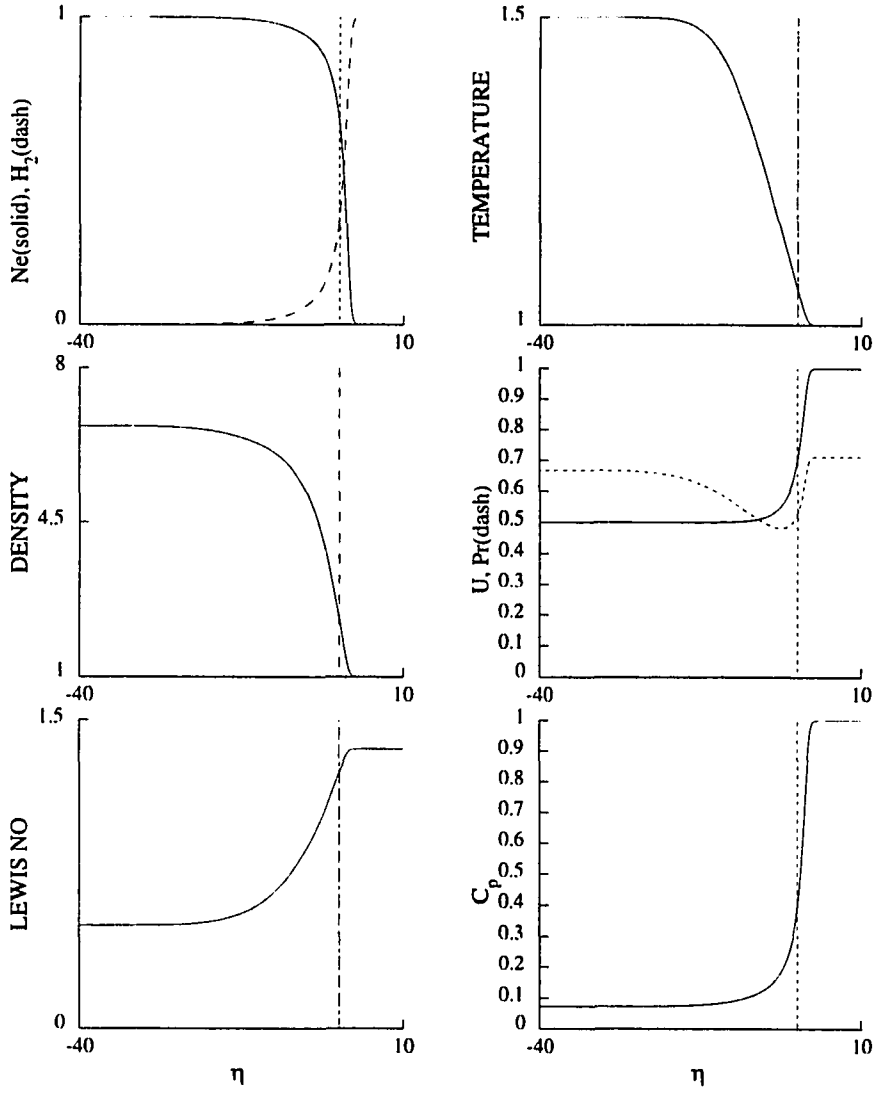

Figure A.1: Mixing layer structure for Ne-H_2.

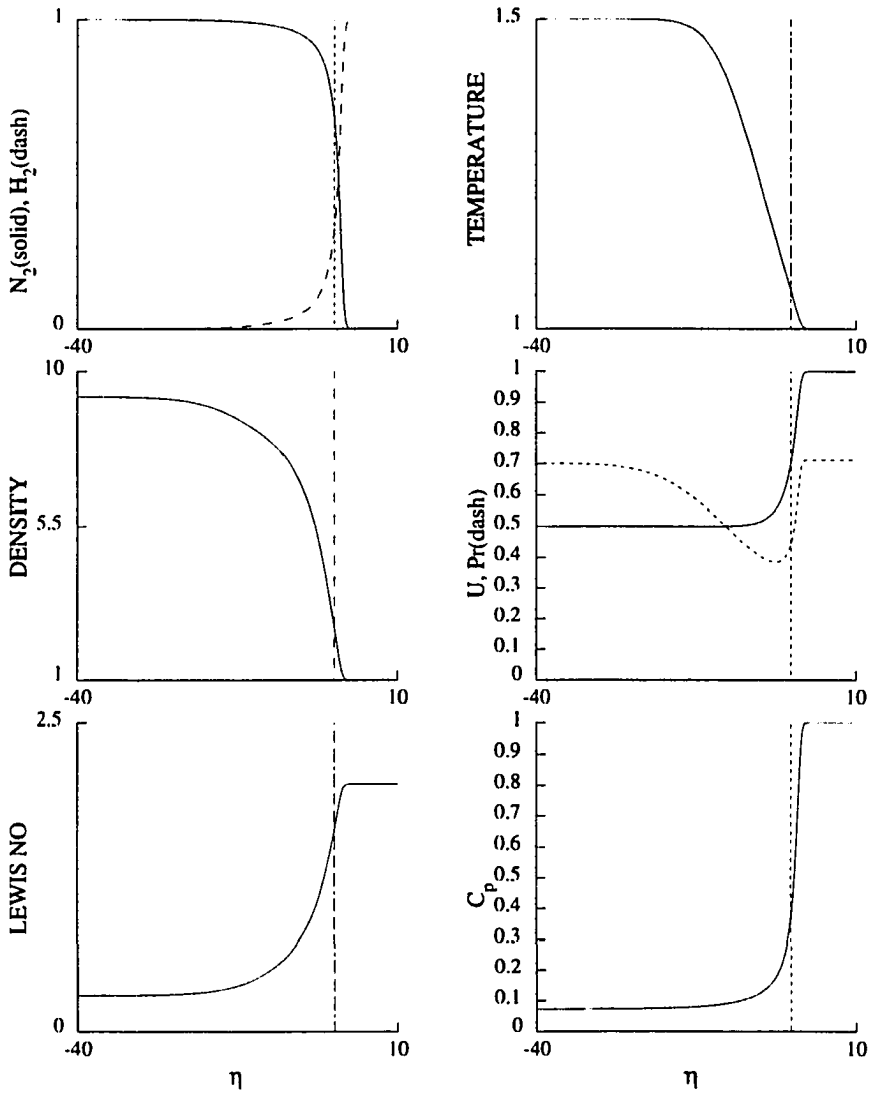

Figure A.2: Mixing layer structure for N_2-H_2.

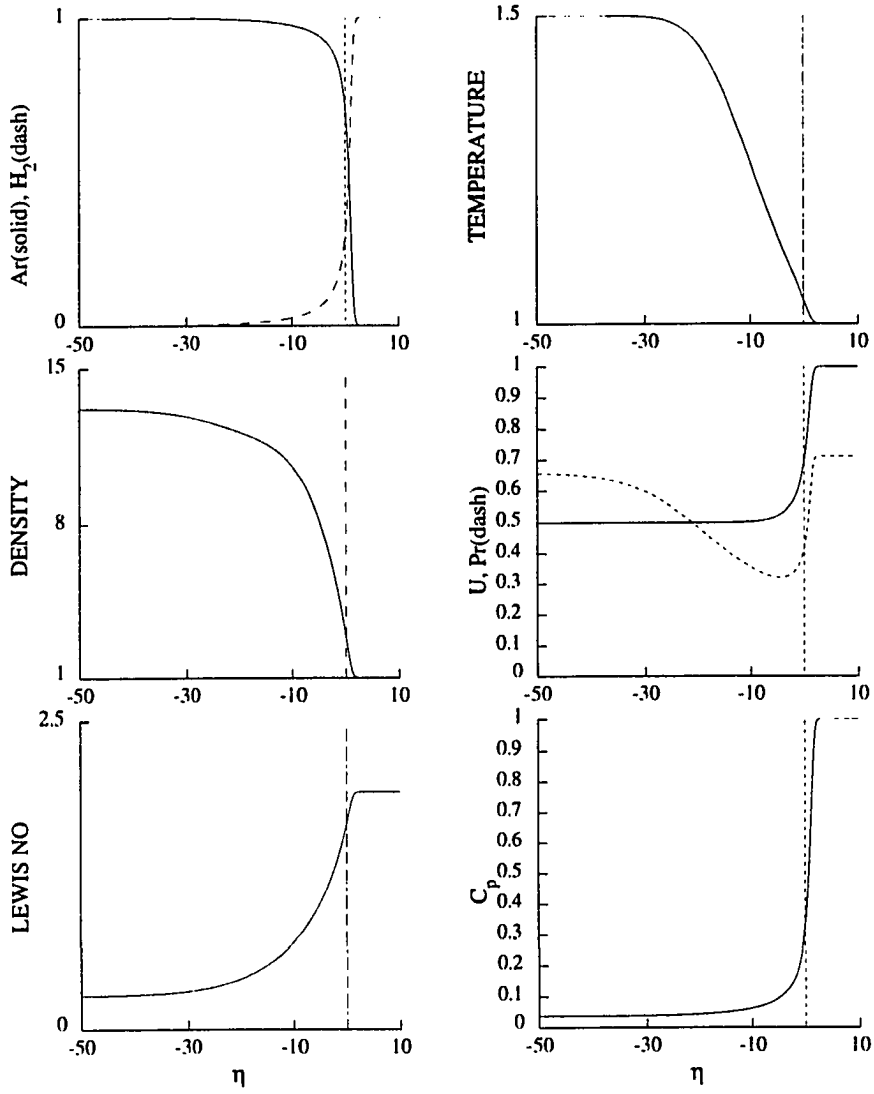

Figure A.3: Mixing layer structure for Ar-H_2.

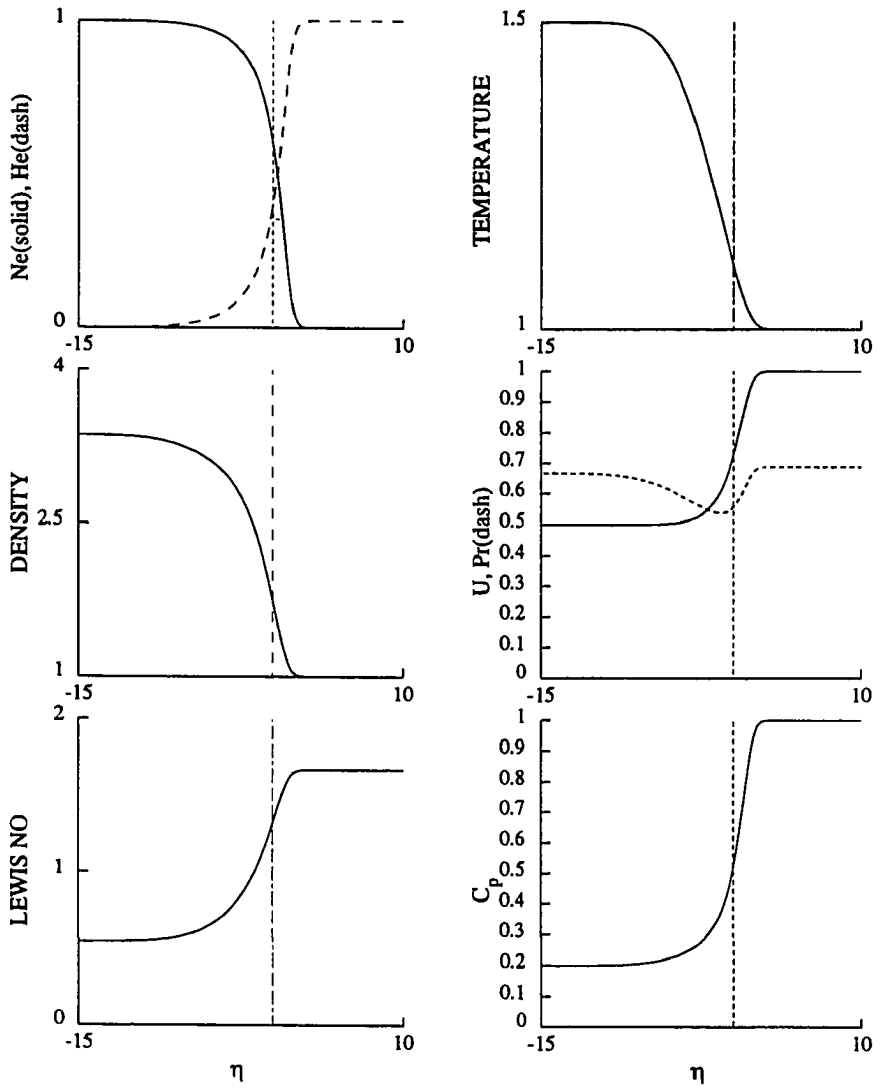

Figure A.4: Mixing layer structure for *Ne-He*.

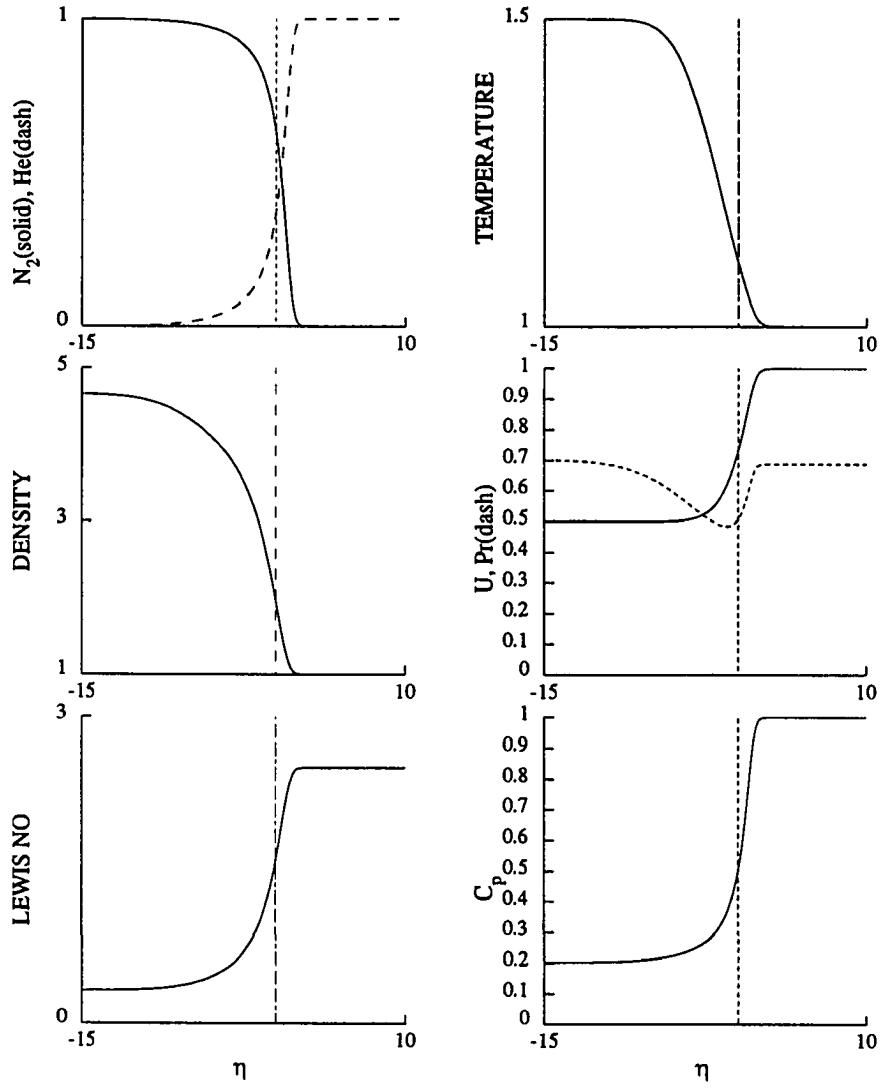

Figure A.5: Mixing layer structure for N_2-He.

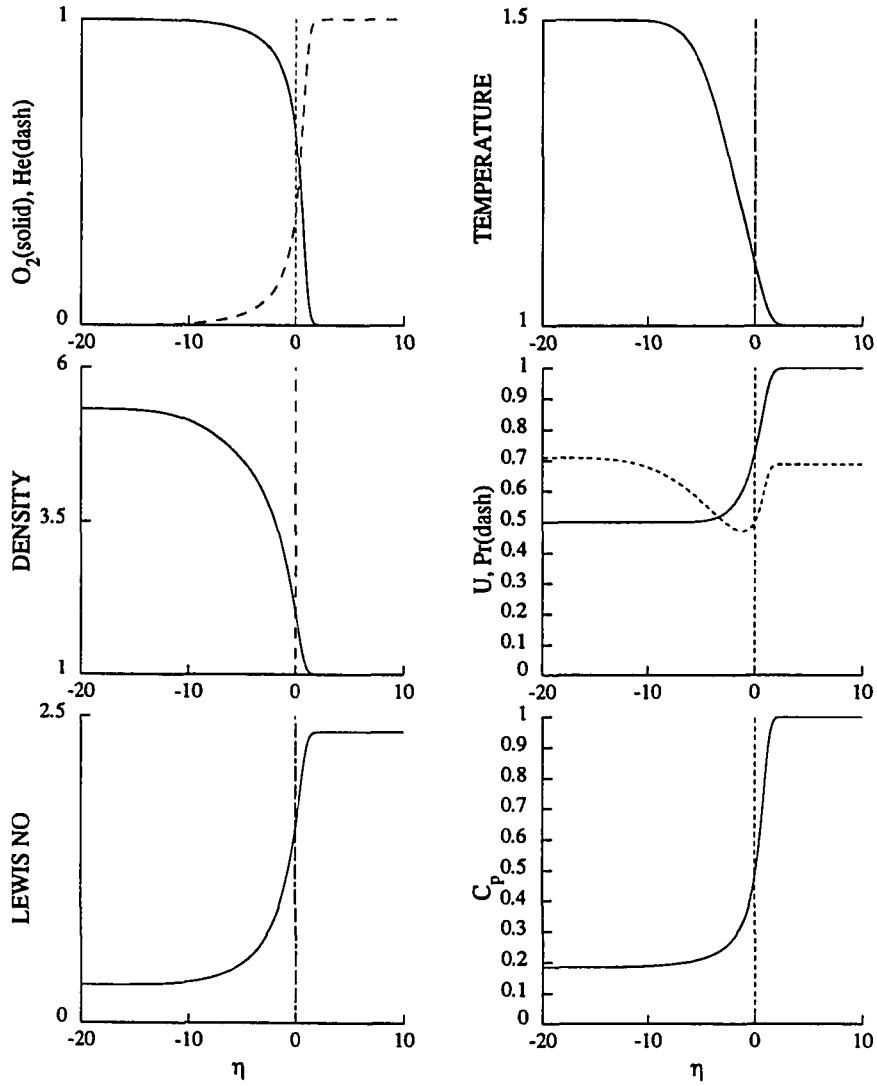

Figure A.6: Mixing layer structure for O_2-He.

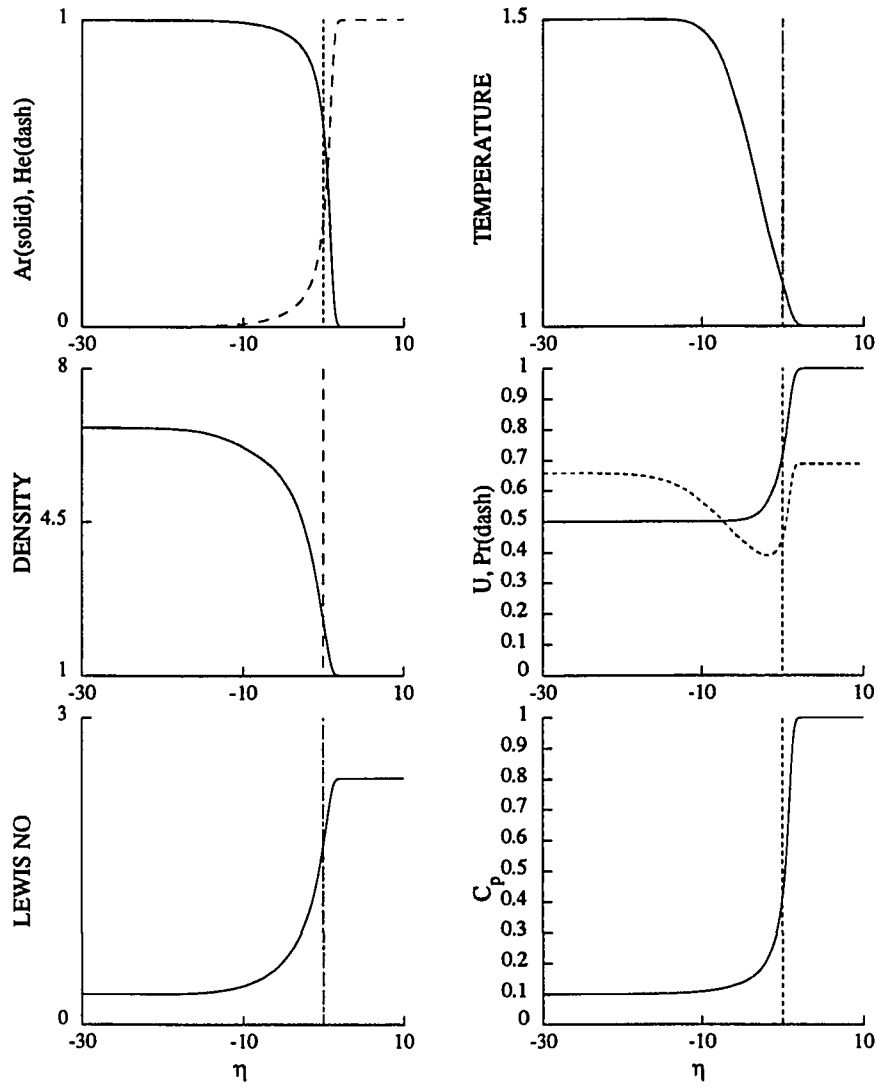

Figure A.7: Mixing layer structure for *Ar-He*.

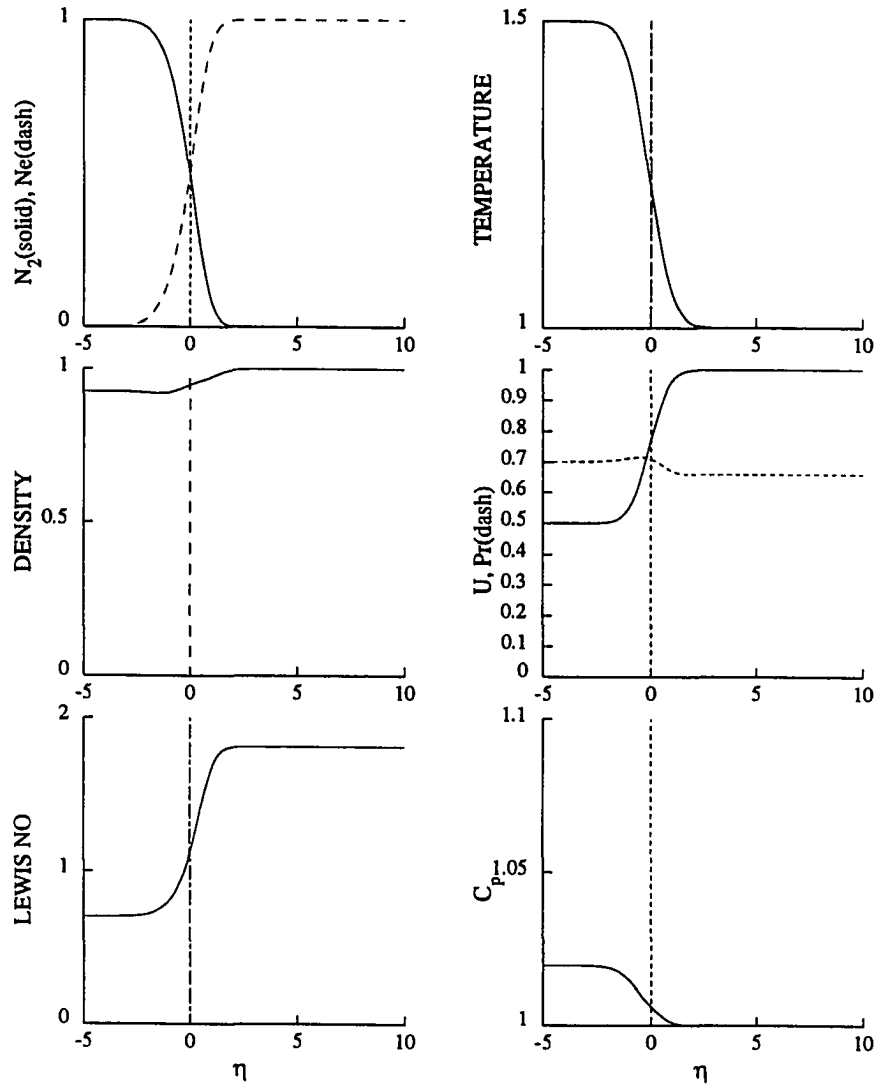

Figure A.8: Mixing layer structure for N_2-Ne.

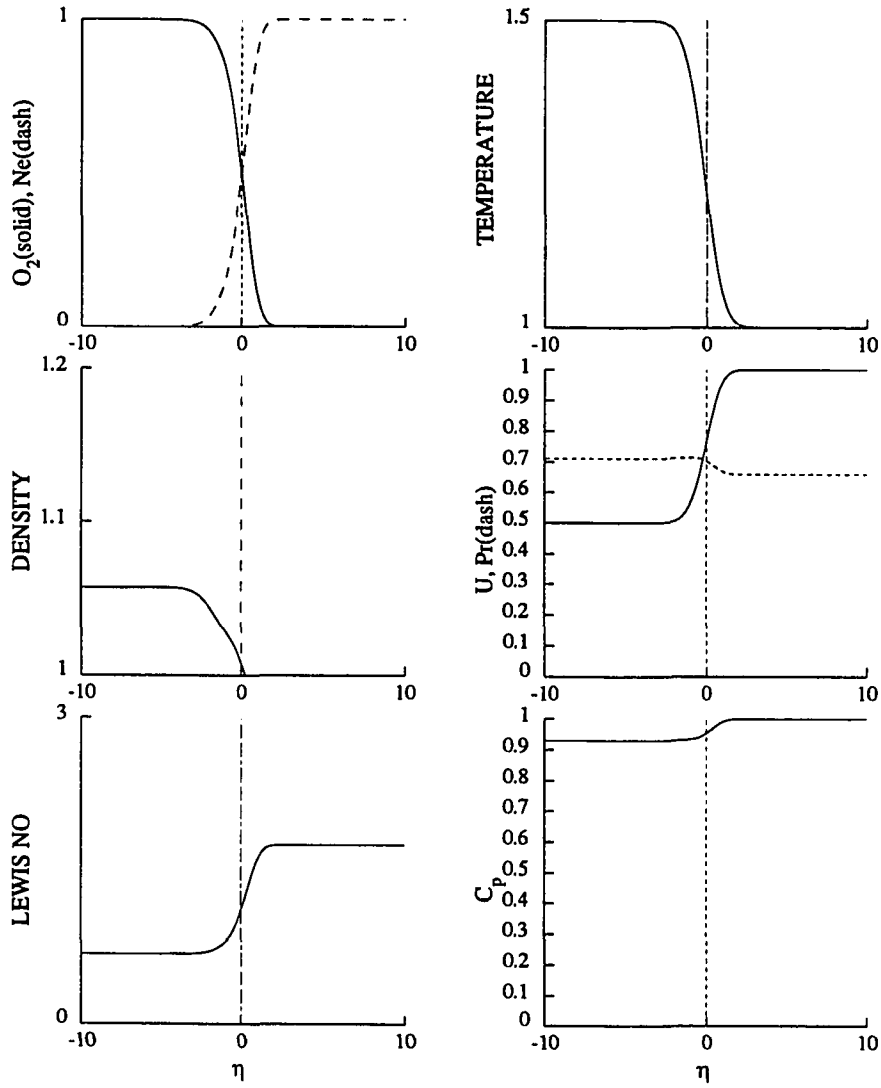

Figure A.9: Mixing layer structure for O_2-Ne.

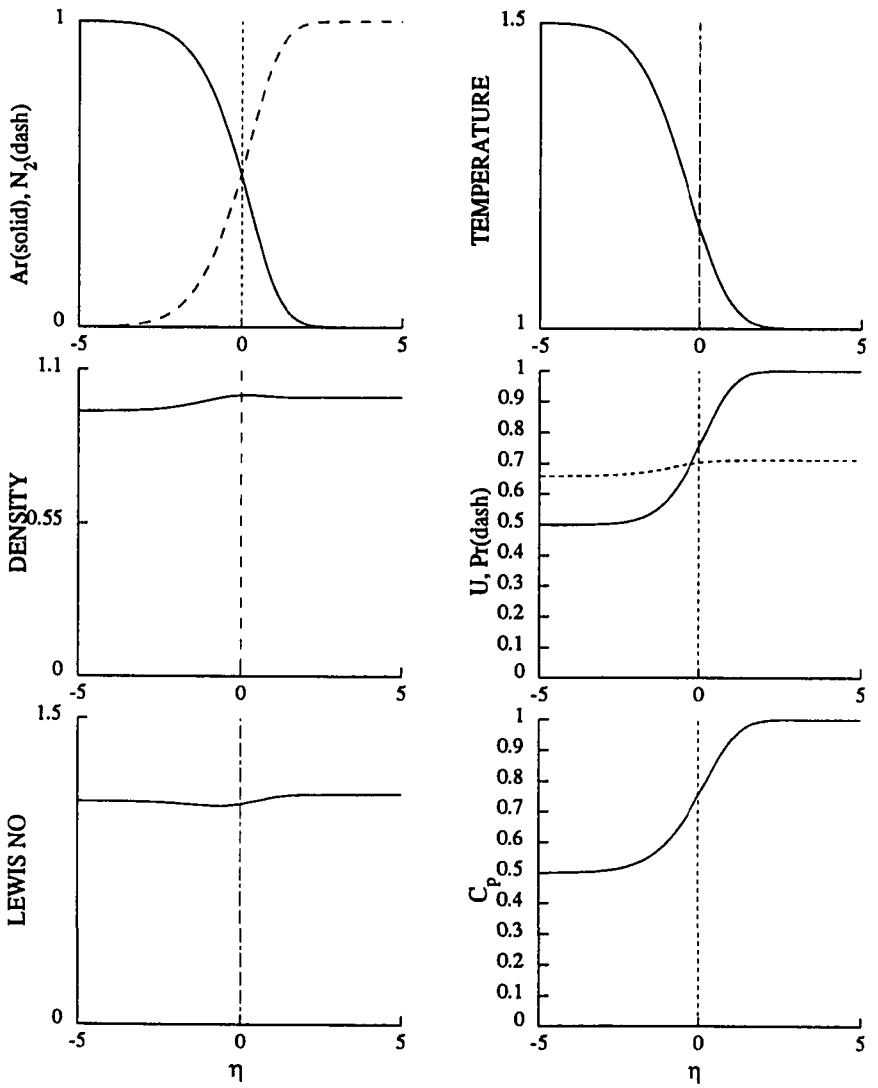

Figure A.10: Mixing layer structure for Ar-N_2.

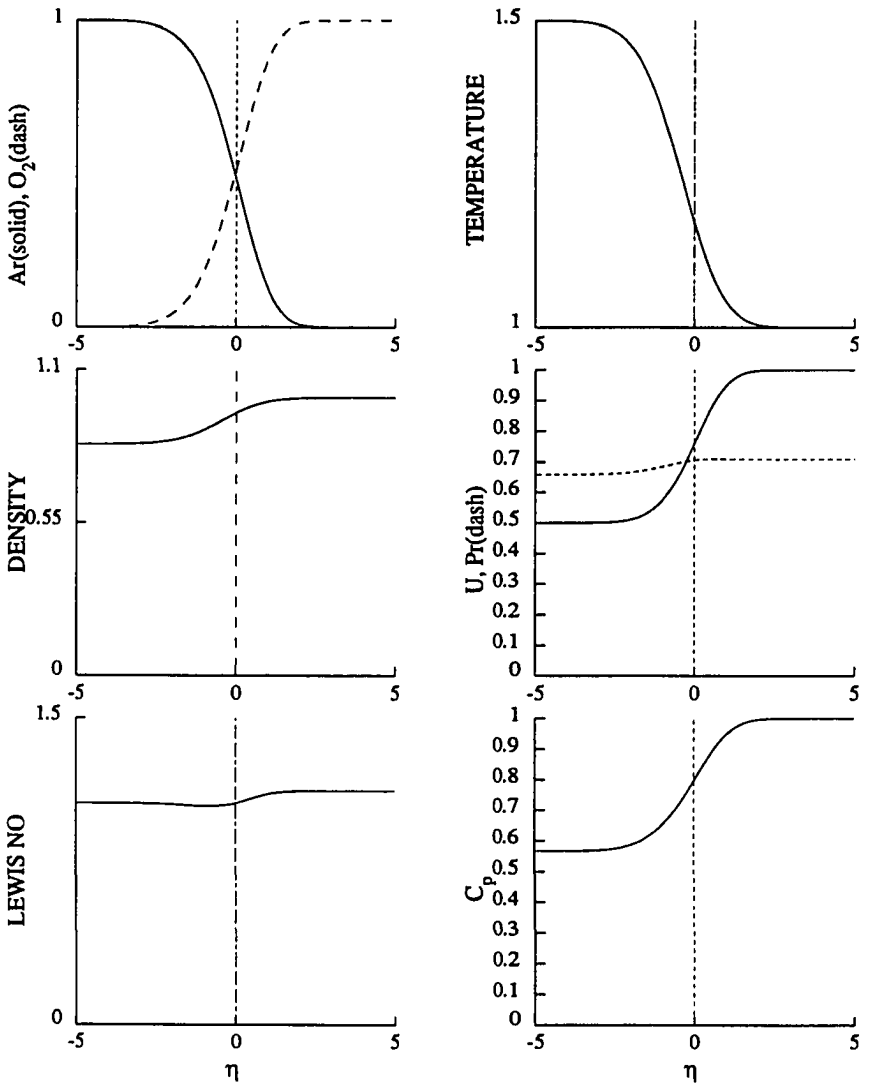

Figure A.11: Mixing layer structure for Ar-O_2.

Appendix B

ADDITIONAL FIGURES FOR BINARY GAS MIXTURES ($W > 1$)

Thirty different combinations of gas mixtures were studied. The structure of the mixing layer is presented here for those combinations not covered in Chapter Four and with $W > 1$.

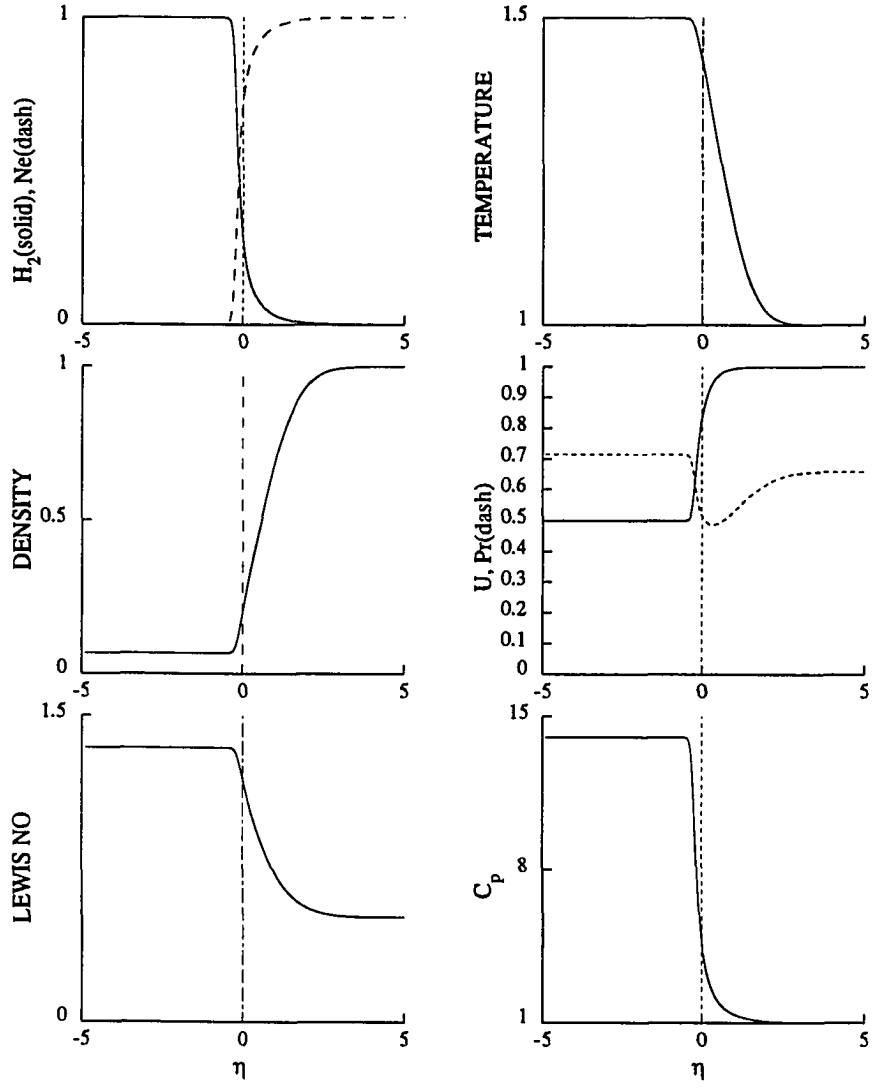

Figure B.1: Mixing layer structure for H_2-He.

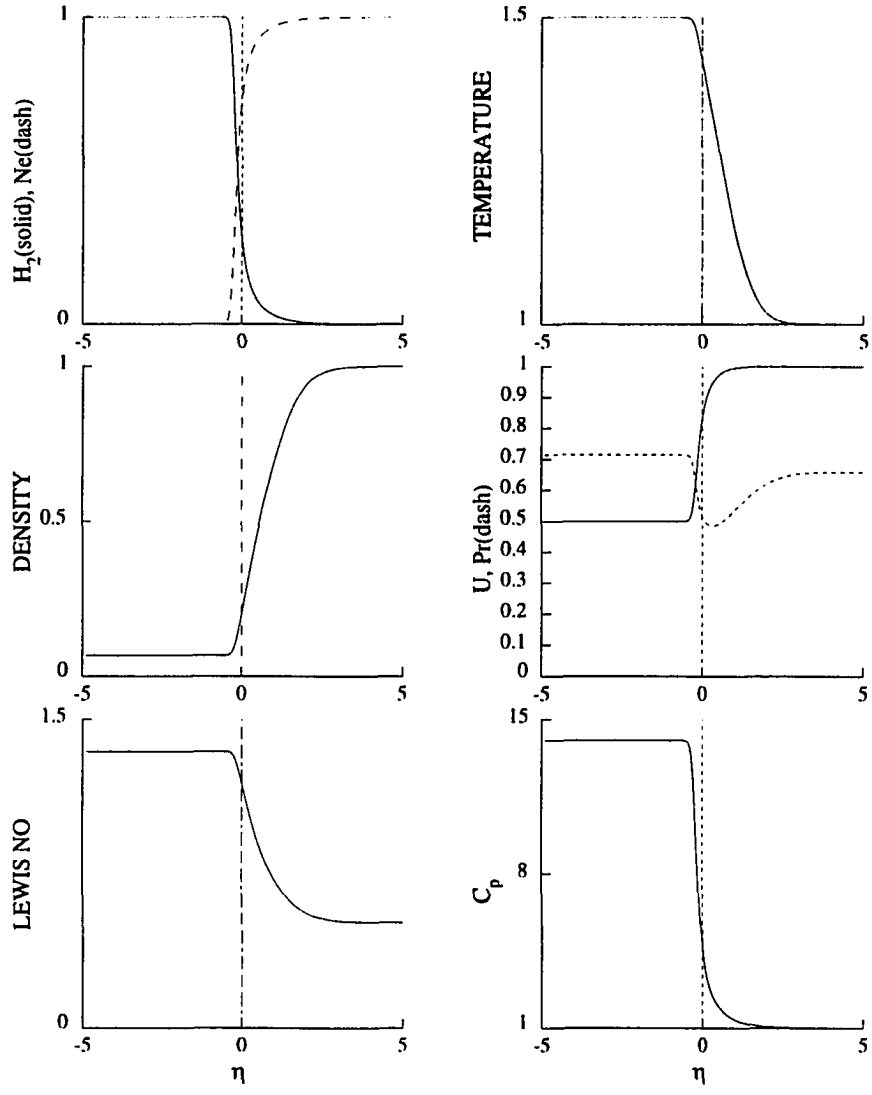

Figure B.2: Mixing layer structure for H_2-Ne.

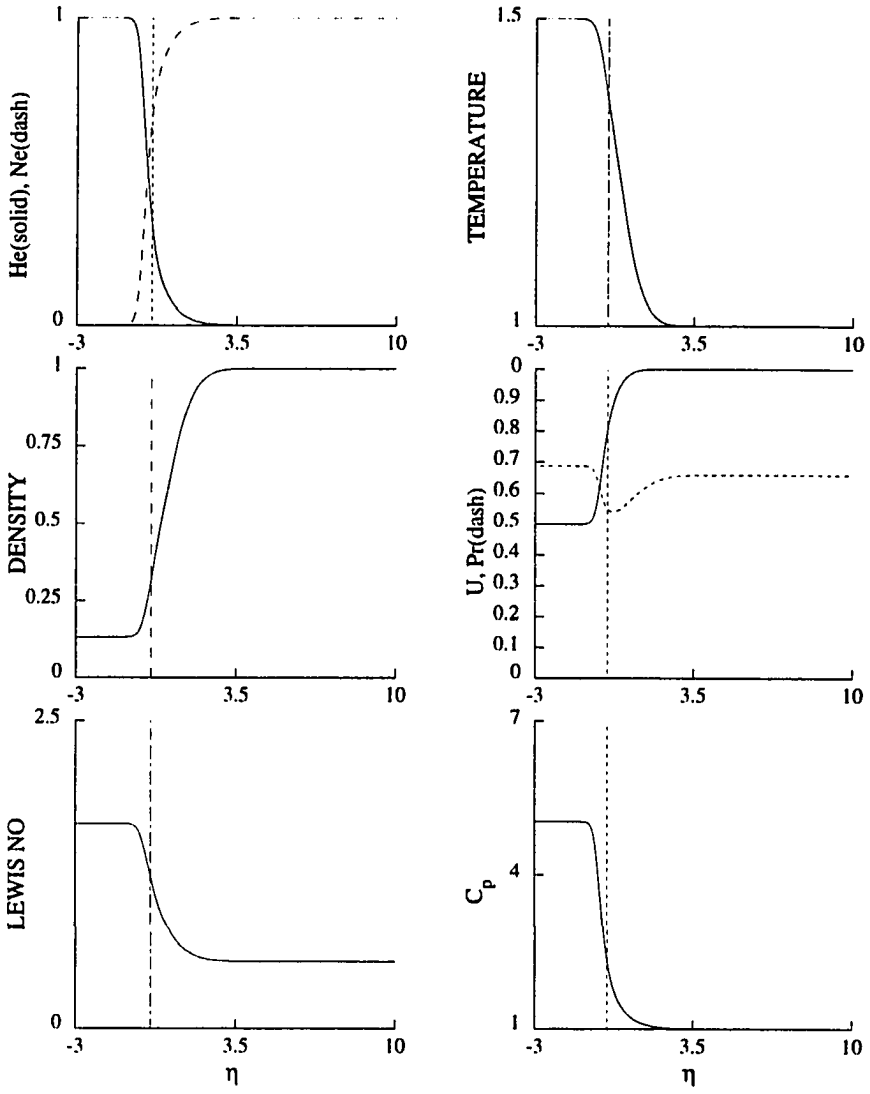

Figure B.3: Mixing layer structure for *He-Ne*.

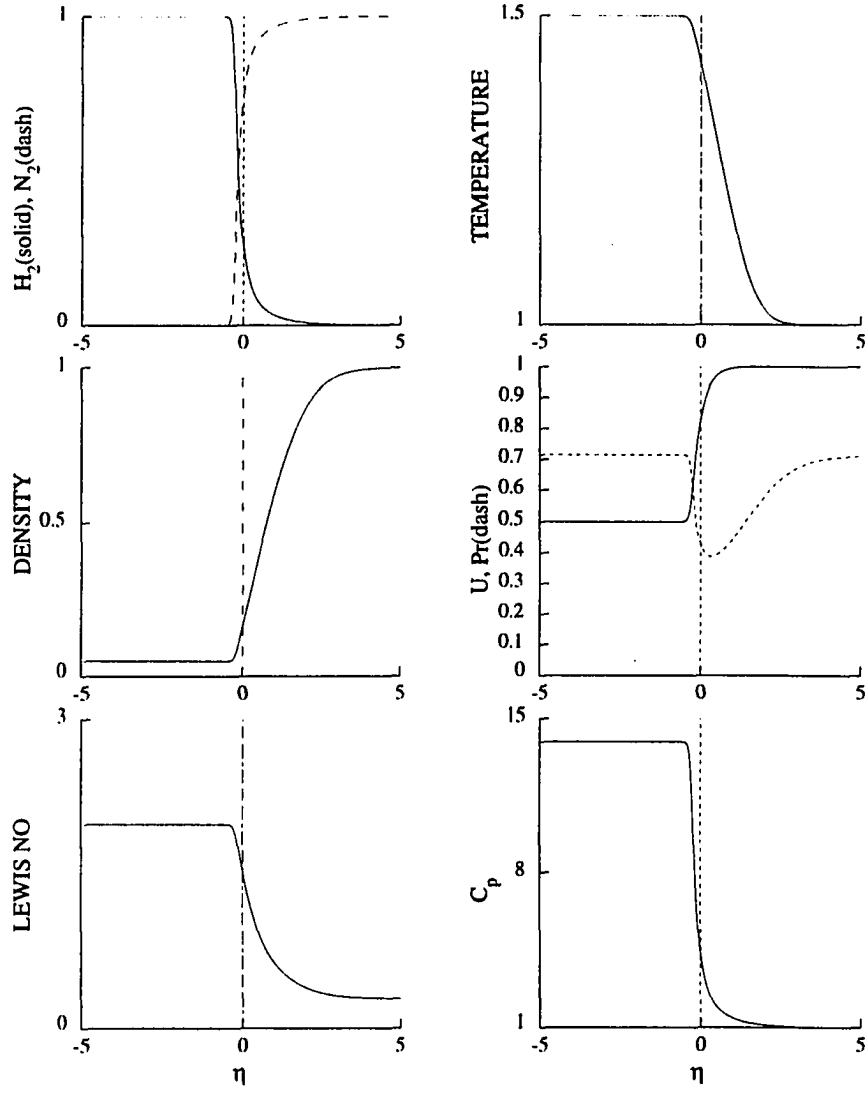

Figure B.4: Mixing layer structure for H_2-N_2.

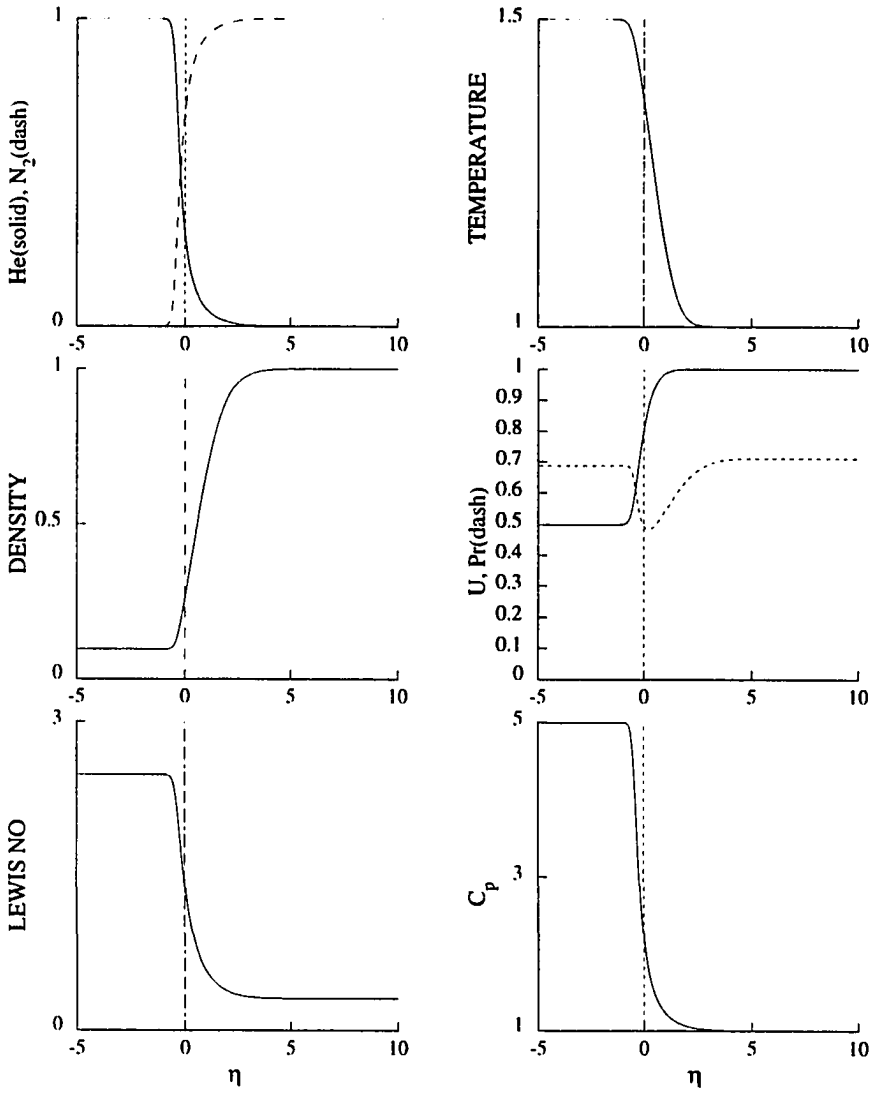

Figure B.5: Mixing layer structure for He-N_2.

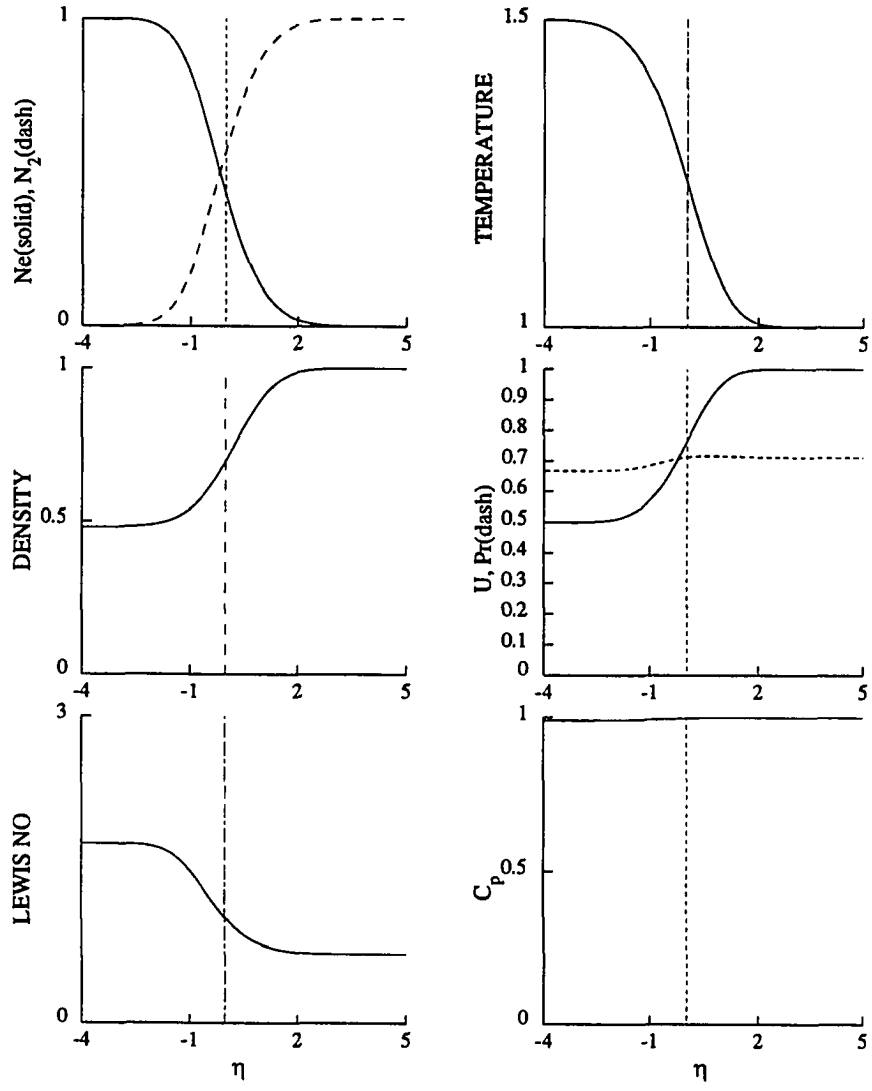

Figure B.6: Mixing layer structure for Ne-N_2.

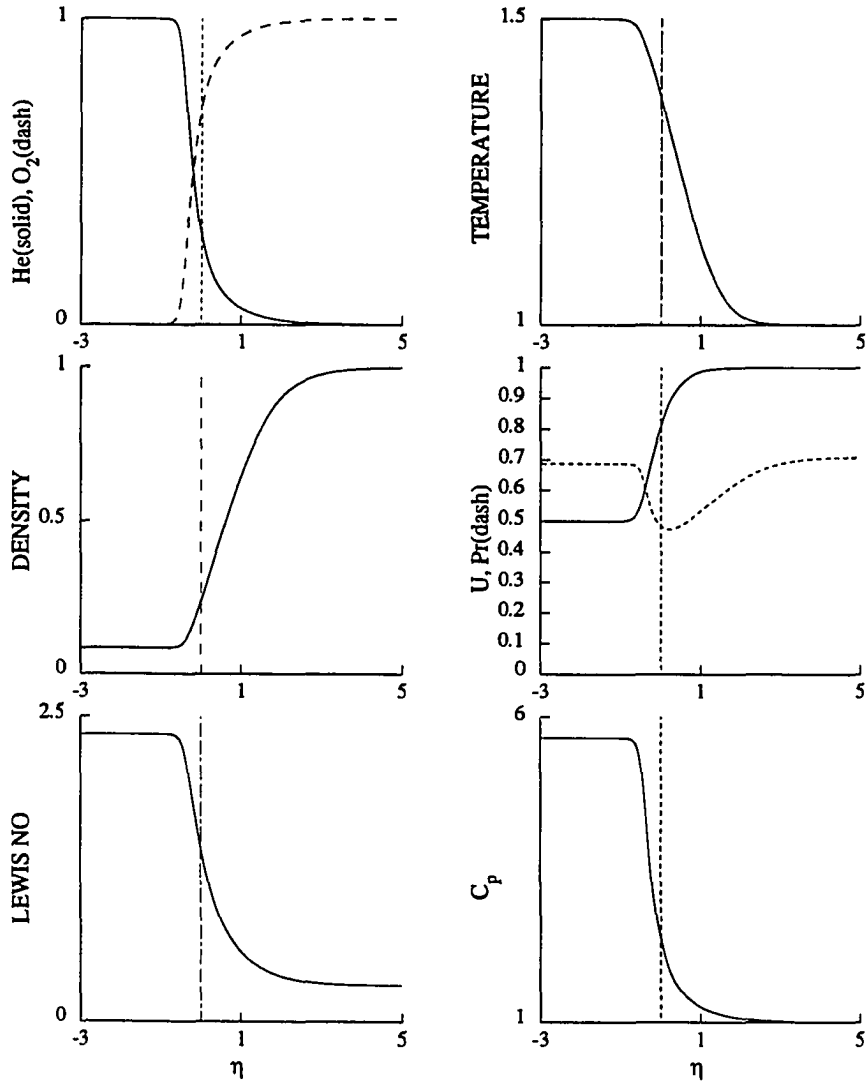

Figure B.7: Mixing layer structure for He-O_2.

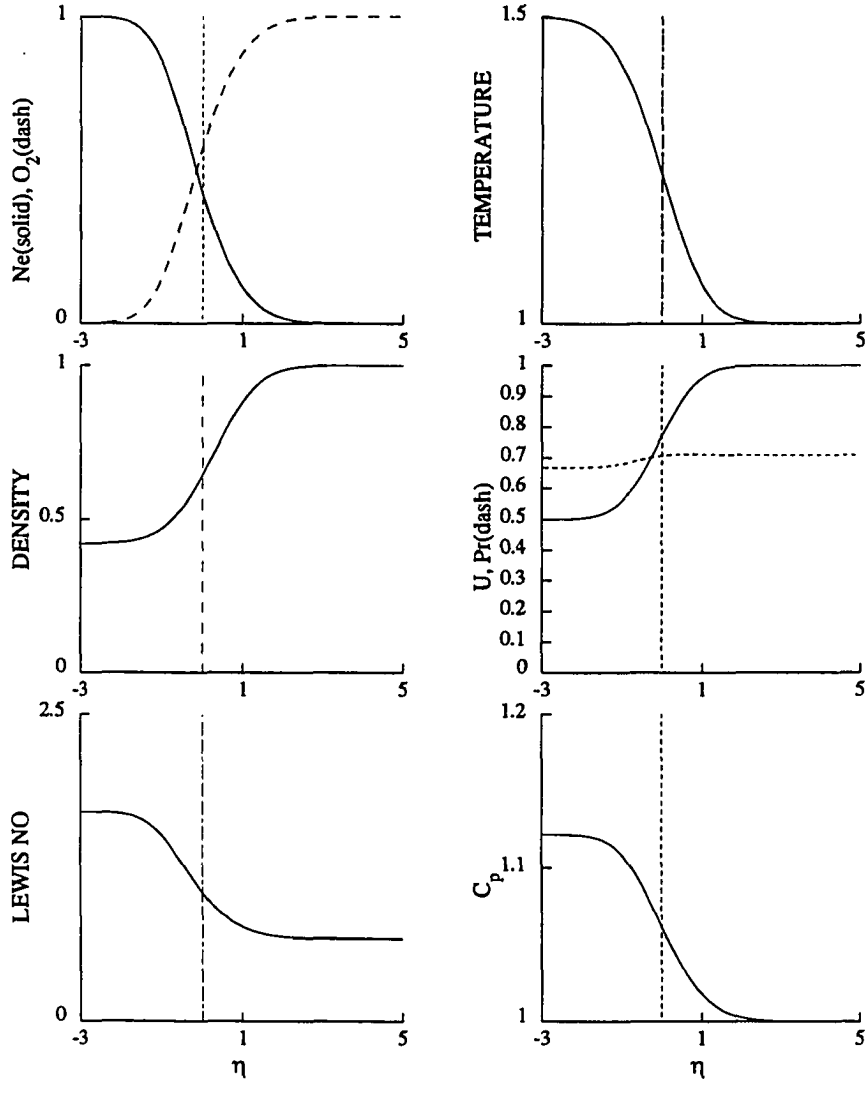

Figure B.8: Mixing layer structure for Ne-O_2.

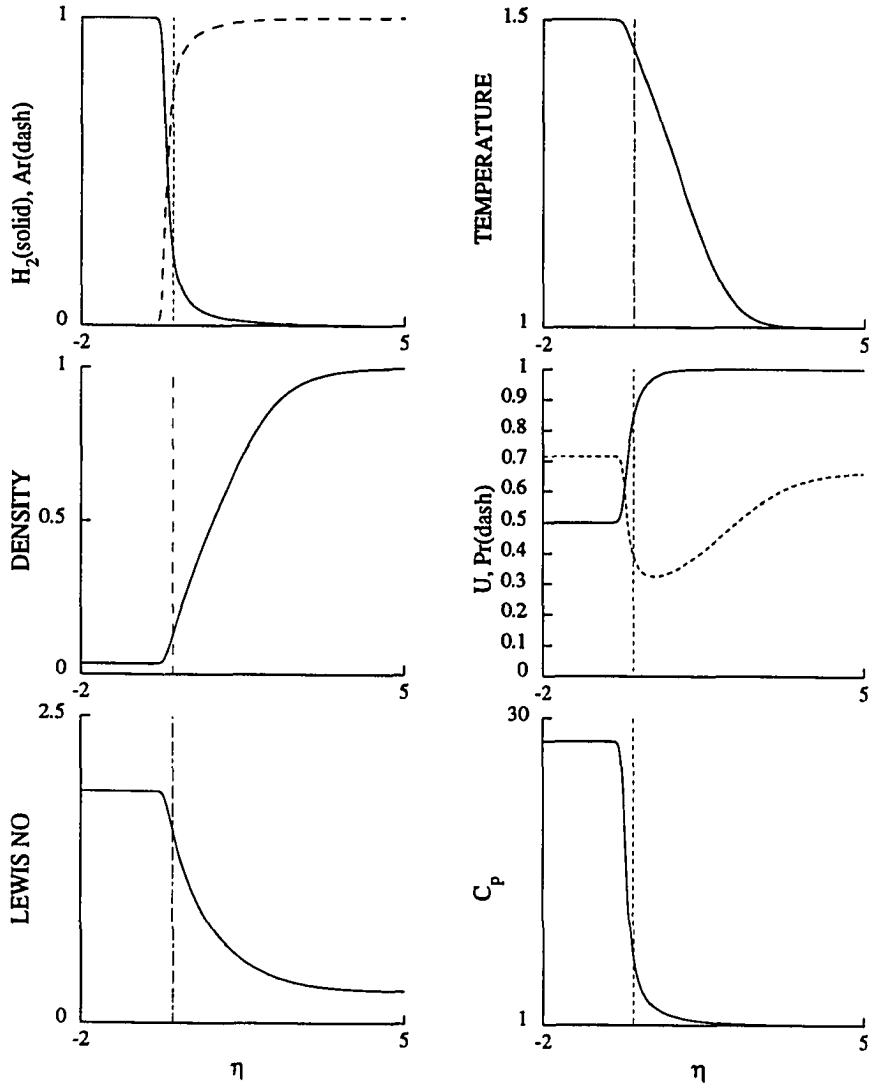

Figure B.9: Mixing layer structure for H_2-Ar.

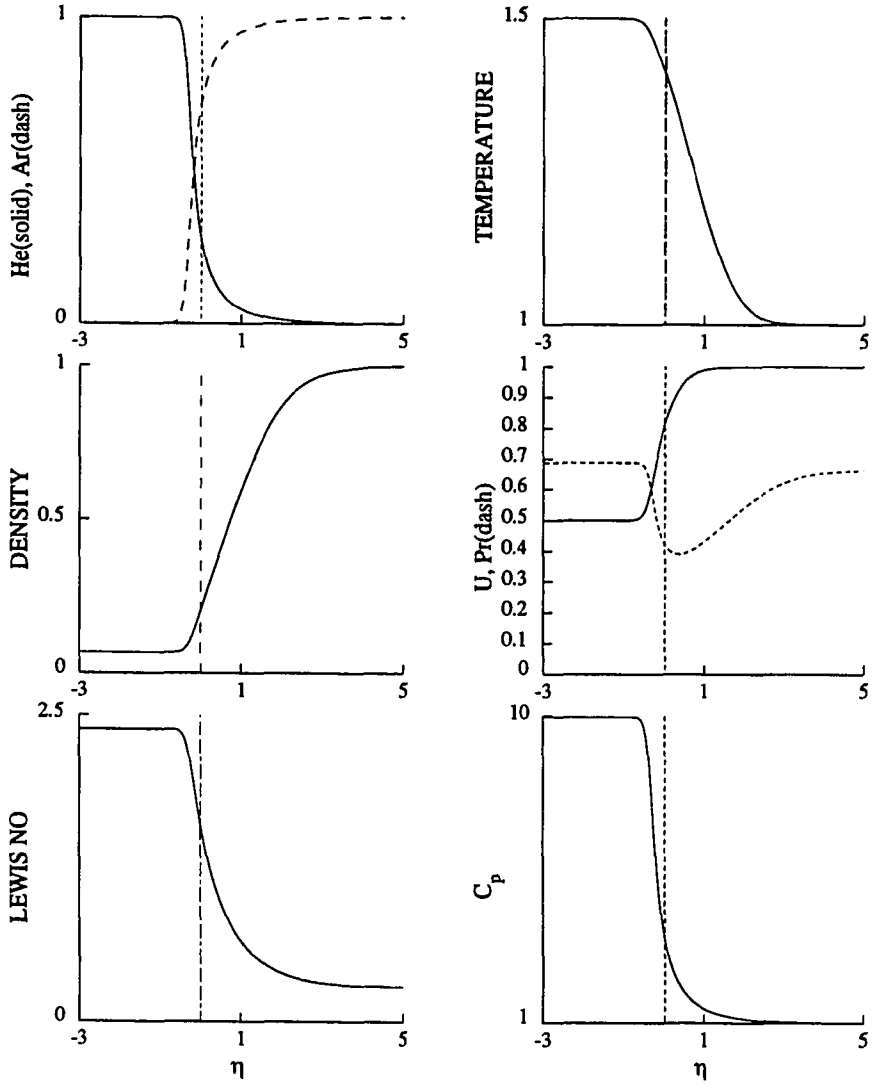

Figure B.10: Mixing layer structure for *He-Ar*.

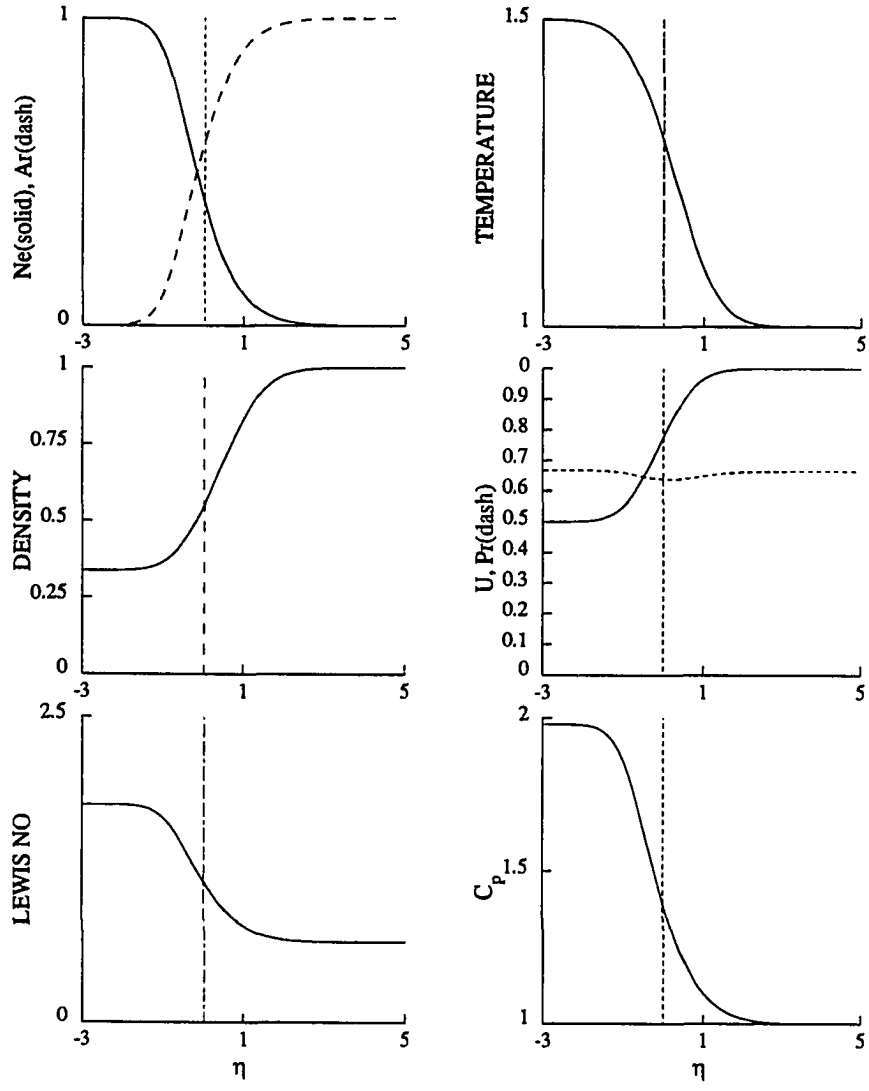

Figure B.11: Mixing layer structure for *Ne-Ar*.

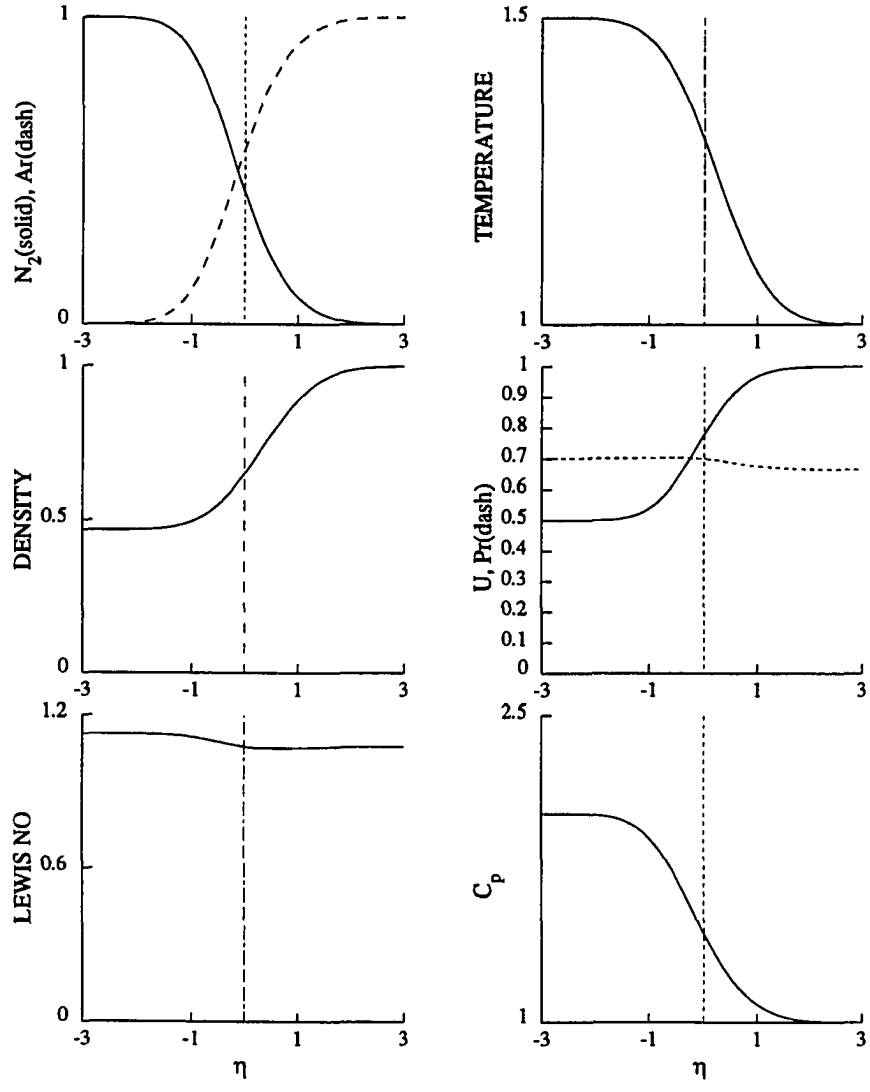

Figure B.12: Mixing layer structure for N_2-Ar.

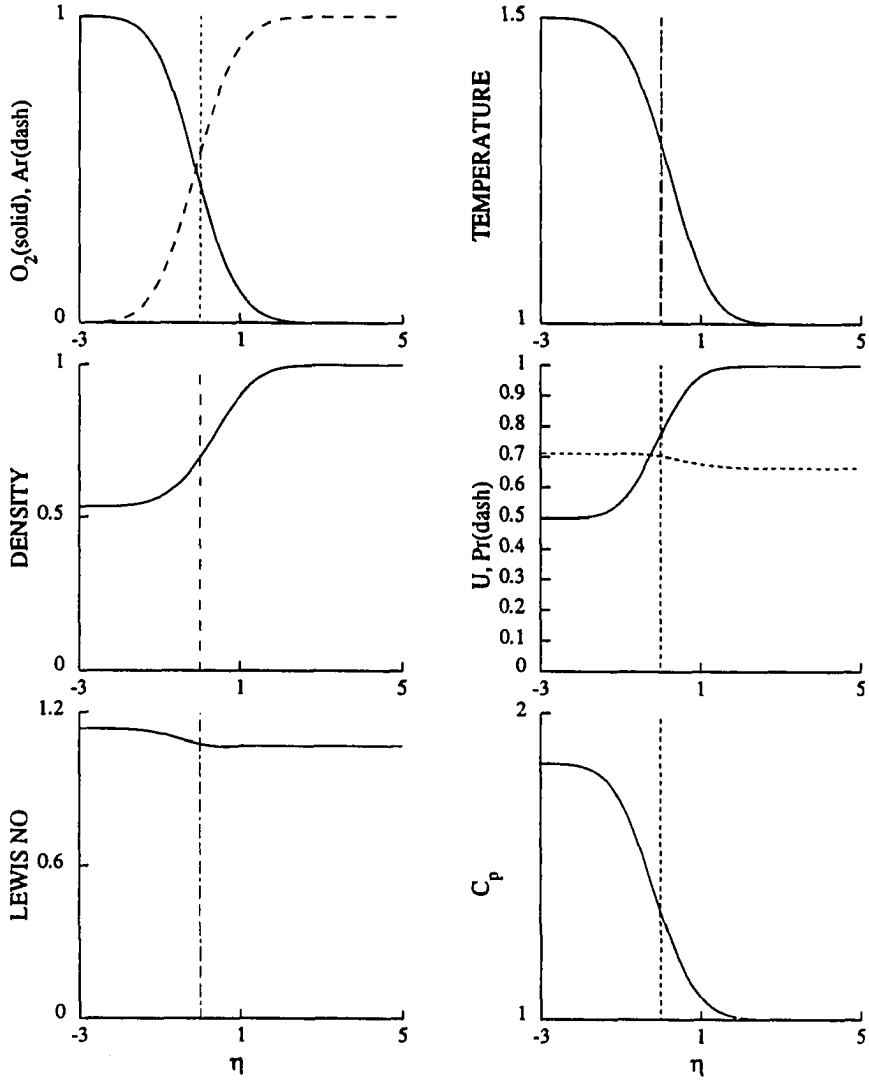

Figure B.13: Mixing layer structure for O_2-Ar.

Autobiographical Statement

Frank Kozusko was born in San Francisco, California on December 18, 1946 and spent most of his boyhood years in Utica, New York. Mr. Kozusko received a Bachelor of Science degree (with honors) from Utica College of Syracuse University in June, 1969. In September, 1969 he began graduate studies in the Department of Physics at University of California at Davis. He received a Master of Arts degree and was advanced to Ph.D. candidacy before his studies were interrupted by military service.

While still a civilian he applied for nuclear submarine duty in the United States Navy. After his interview with Admiral Rickover and acceptance in the Navy Nuclear Propulsion Program, he began what turned into a twenty-one year career in the U. S. Navy, in June 1971.

During his Naval career, Mr. Kozusko served as ship's company on three submarines, two cruisers and one aircraft carrier. He also served as a nuclear propulsion training officer for Commander U.S. Naval Air Forces, Atlantic Fleet and Commander U.S. Naval Surface Forces, Atlantic Fleet for three years. His final tour of duty in the Navy was three years as Assistant Professor of Naval Science at Hampton University. His numerous military awards and citations include three Navy Commendation Medals with one for heroism. He has been submerged in submarines in excess of a

total of two years.

In preparation for a second career after the inevitable end of military service, Lieutenant Commander Kozusko began part-time study in the graduate Mathematics program at Old Dominion University in August, 1987, and continue part-time for five years until retirement from the Navy in June, 1992. He received a Masters degree in Computational and Applied Mathematics from Old Dominion University in May, 1991. He started full time studies in July, 1992 and has since been a graduate teaching assistant in the Mathematics Department.

Mr. Kozusko has been pleased to conducted his research at the Institute for Computer Applications in Science and Engineering(ICASE) at NASA Langley Research in Hampton, Virginia and gratefully acknowledges their support. He anticipates completing all requirements for the Ph.D in Computational and Applied Mathematics in August,1995. He has published a paper, titled: Study of Ignition of a Diffusion Flame in the Field of a Vortex Pair, F. Kozusko, Michele G. Macaraeg and T. L. Jackson in Transition, Turbulence and Combustion 1994.

Mr. Kozusko is married to the former Christine Szczerba of Utica, New York. She is a first grade teaching assistant for the Hampton city schools system. They have three children Michelle and Edward, who are both graduates of Virginia Tech, and Teresa a student at Hampton High School.